EZH2-mediated primary cilium deconstruction drives metastatic melanoma formation

Zingg, Daniel ; Debbache, Julien ; Peña-Hernández, Rodrigo ; Antunes, Ana T ; Schaefer, Simon M ; Cheng, Phil F ; Zimmerli, Dario ; Haeusel, Jessica ; Calçada, Raquel R ; Tuncer, Eylul ; Zhang, Yudong ; Bossart, Raphaël ; Wong, Kwok-Kin ; Basler, Konrad ; Dummer, Reinhard ; Santoro, Raffaella ; Levesque, Mitchell P ; Sommer, Lukas

Abstract: Human melanomas frequently harbor amplifications of EZH2. However, the contribution of EZH2 to melanoma formation has remained elusive. Taking advantage of murine melanoma models, we show that EZH2 drives tumorigenesis from benign BrafV600E- or NrasQ61K-expressing melanocytes by silencing of genes relevant for the integrity of the primary cilium, a signaling organelle projecting from the surface of vertebrate cells. Consequently, gain of EZH2 promotes loss of primary cilia in benign melanocytic lesions. In contrast, blockade of EZH2 activity evokes ciliogenesis and cilia-dependent growth inhibition in malignant melanoma. Finally, we demonstrate that loss of cilia enhances pro-tumorigenic WNT/ -catenin signaling, and is itself sufficient to drive metastatic melanoma in benign cells. Thus, primary cilia deconstruction is a key process in EZH2-driven melanomagenesis.

DOI: https://doi.org/10.1016/j.ccell.2018.06.001

Originally published at:
Zingg, Daniel; Debbache, Julien; Peña-Hernández, Rodrigo; Antunes, Ana T; Schaefer, Simon M; Cheng, Phil F; Zimmerli, Dario; Haeusel, Jessica; Calçada, Raquel R; Tuncer, Eylul; Zhang, Yudong; Bossart, Raphaël; Wong, Kwok-Kin; Basler, Konrad; Dummer, Reinhard; Santoro, Raffaella; Levesque, Mitchell P; Sommer, Lukas (2018). EZH2-mediated primary cilium deconstruction drives metastatic melanoma formation. Cancer Cell, 34(1):69-84.
DOI: https://doi.org/10.1016/j.ccell.2018.06.001

Graphical Abstract

Click here to download Graphical Abstract No frame G abstract.pdf

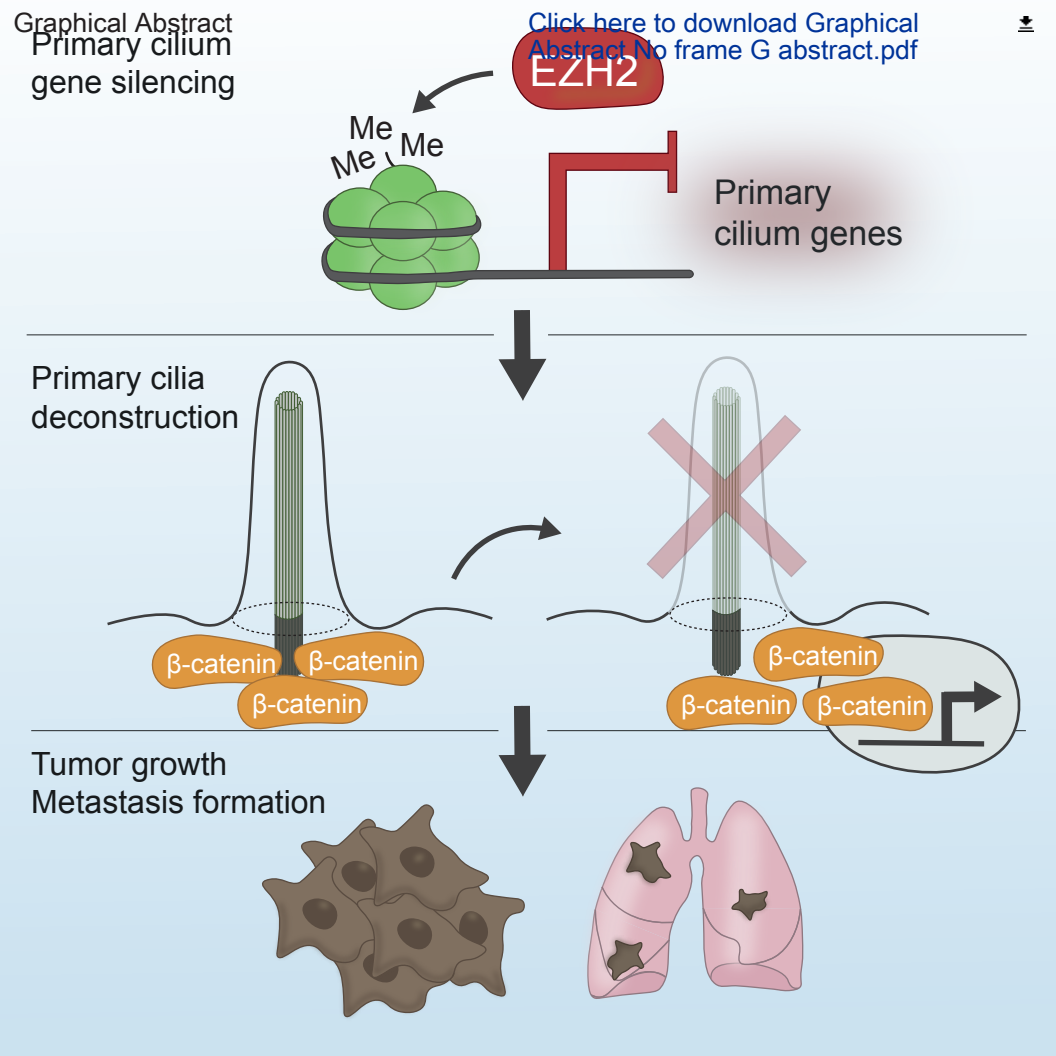

EZH2-mediated primary cilium deconstruction drives metastatic melanoma formation

Daniel Zingg,[1,6] Julien Debbache,[1] Rodrigo Peña-Hernández,[2] Ana T. Antunes,[1] Simon. M. Schaefer,[1] Phil F. Cheng,[3] Dario Zimmerli,[4] Jessica Haeusel,[1] Raquel R. Calçada,[1] Eylul Tuncer,[1] Yudong Zhang,[1] Raphaël Bossart,[1] Kwok-Kin Wong,[5] Konrad Basler,[4] Reinhard Dummer,[3] Raffaella Santoro,[2] Mitchell P. Levesque,[3] and Lukas Sommer[1,7,*]

[1] Stem Cell Biology, Institute of Anatomy, University of Zurich, Winterthurerstrasse 190, CH-8057 Zurich, Switzerland

[2] Department of Molecular Mechanisms of Disease, University of Zurich, Winterthurerstrasse 190, CH-8057 Zurich, Switzerland

[3] Department of Dermatology, University Hospital Zurich, University of Zurich, Gloriastrasse 31, CH-8091 Zurich, Switzerland

[4] Institute of Molecular Life Sciences, University of Zurich, Winterthurerstrasse 190, CH-8057 Zurich, Switzerland

[5] Division of Hematology & Medical Oncology, Laura and Isaac Perlmutter Cancer Center, New York University Langone Medical Center, 522 First Avenue, New York, NY 10016, USA

[6] Present Address: Division of Molecular Pathology, The Netherlands Cancer Institute, Plesmanlaan 121, 1066 CX Amsterdam, the Netherlands

[7] Lead Contact

* Correspondence: lukas.sommer@anatomy.uzh.ch

SUMMARY

Human melanomas frequently harbor amplifications of *EZH2*. However, the contribution of this methyltransferase to melanoma formation has remained elusive. Taking advantage of murine melanoma models, we show that EZH2 drives tumorigenesis from benign $Braf^{V600E}$ or $Nras^{Q61K}$-expressing melanocytes by silencing of genes relevant for the integrity of the primary cilium, a signaling organelle projecting from the surface of vertebrate cells. Consequently, gain of EZH2 promotes loss of primary cilia in benign melanocytic lesions. In contrast, blockade of EZH2 activity evokes ciliogenesis and cilia-dependent growth inhibition in malignant melanoma. Finally, we demonstrate that loss of cilia enhances pro-tumorigenic WNT/β-catenin signaling and is itself sufficient to drive metastatic melanoma in benign cells. Thus, primary cilia deconstruction is a key process in EZH2-driven melanomagenesis.

KEY WORDS

Melanoma, Tumor Initiation, Metastasis, Epigenetics, PRC2, EZH2, Primary Cilium, WNT/β-catenin Signaling

SIGNIFICANCE

Aberrant activity of epigenetic modifiers, such as the histone methyltransferase EZH2, is thought to contribute to the formation of various cancer entities. Here we show that EZH2, in conjunction with oncogenic *BRAF* or *NRAS*, drives formation of metastatic melanoma. EZH2 exerts tumorigenicity through epigenetic silencing of genes relevant for the primary cilium, resulting in deconstruction of this signaling organelle and potentiation of WNT/β-catenin signaling. Importantly, primary cilium disassembly itself suffices to initiate WNT signaling-dependent melanoma. Loss of primary cilia and gain of β-catenin activity are hallmarks of many cancers. Thus, EZH2-mediated cilia deconstruction associated with WNT signal stimulation could, in principle, be relevant for tumor development in a variety of tissues.

INTRODUCTION

In recent years, many studies have revealed dysregulation of Polycomb repressive complex 2 (PRC2) in cancer. PRC2 epigenetically suppresses gene transcription through tri-methylation of lysine 27 in histone 3 (H3K27me3). Among others, the catalytic capacity of PRC2 can be potentiated by either overexpression or gain-of-function (GoF) mutations (e.g. Y646F, Y646N) of Enhancer of zeste homolog 2 (*EZH2*), the gene encoding the methyltransferase unit of PRC2 (Kim and Roberts, 2016).

Recent attempts to decipher the significance of elevated PRC2 activity for tumorigenesis have revealed tissue-specific expression of wild-type (WT) *Ezh2* to foster breast, prostate, and lung epithelial neoplasia in mice (Koppens et al., 2017; Li et al., 2009; Zhang et al., 2016). Expression of *Ezh2*^{Y646F} or *Ezh2*^{Y646N} in murine B-cells likewise drove hyperplastic transformation ultimately progressing into lymphoma (Béguelin et al., 2013; Berg et al., 2014; Souroullas et al., 2016). Moreover, in conjunction with *Braf*^{V600E}, substitution of endogenous *Ezh2* with *Ezh2*^{Y646F} led to emergence of non-metastatic melanocytic tumors (Souroullas et al., 2016). In an autochthonous mouse model of malignant melanomagenesis, homozygous deletion of *Ezh2* abolished cutaneous melanoma initiation and metastatic spread (Zingg et al., 2015). However, it remains unresolved whether a gain in EZH2 activity is sufficient to drive malignant metastatic melanoma.

In solid cancers, together with cutaneous melanoma, PRC2 activity has been connected to regulation of cell proliferation and tumor growth through repression of tumor suppressors, such as *CDKN1A* and *CDKN2A* (Kim and Roberts, 2016). In the context of oncogenic NRAS^{Q61K} signaling and *Cdkn2a* gene knockout, mice spontaneously develop melanoma (Ackermann et al., 2005). Yet, in these animals, *Ezh2* ablation is sufficient to prevent tumor growth (Zingg et al., 2015). Hence, EZH2 might contribute to melanomagenesis by controlling genes beyond traditional tumor suppressors.

RESULTS

Recurrent gains of *EZH2* in human melanomas confer tumorigenesis

Analysis of The Cancer Genome Atlas' (TCGA) datasets on skin cutaneous melanoma (TCGA Network, 2015) revealed the *EZH2* locus to be amplified in 58.3% of melanoma samples. *EZH2* copy number gains were associated with enhanced *EZH2* transcription compared to samples with normal or loss of *EZH2* copy numbers (Figures 1A and S1A). This appeared to be independent of genetic subtypes, i.e. *BRAF* versus *NRAS* somatic GoF mutations, *NF1* loss-of-function (LoF), and triple WT (Figures S1A and S1B). Furthermore, across several published gene expression datasets (Kabbarah et al., 2010; Scatolini et al., 2010; Smith et al., 2005; Talantov et al., 2005), *EZH2* levels were significantly increased in malignant melanomas in comparison to benign nevus samples (Figure 1B).

These findings prompted us to investigate the functional relevance of EZH2 upregulation for melanomagenesis. We first expressed $EZH2^{WT}$ and $EZH2^{Y646N}$ in the melanoma cell line A375, which led to global gains in H3K27me3 (Figures S1C and S1D). $EZH2^{WT}$ and $EZH2^{Y646N}$ comparably triggered colony formation in A375 (Figure 1C). Importantly, the clonogenic potential depended on canonical EZH2 function, as inhibition of the catalytic activity of EZH2 using the chemical compound GSK503 (Béguelin et al., 2013) largely abrogated A375 clonogenicity (Figures 1C and S1D). Next, we turned to a mouse model of melanoma, in which dermal hyperplasia formation reminiscent of human benign nevi is driven through a $Nras^{Q61K}$ transgene. In combination with a *Cdkn2a* knockout, few of these pre-malignant lesions progress into melanoma over time (Ackermann et al., 2005). We isolated RIH hyperplasia cells from $Nras^{Q61K}$;$Cdkn2a^{-/-}$ mice using Cre-mediated *R26R–lox-stop-lox-*(*LSL*)*–tdTomato* cell labeling and fluorescence-activated cell sorting (FACS) (Figures 1D and S1E). When transplanted subcutaneously (SC) into immunocompromised Nude-$Foxn1^{nu/nu}$ mice, control RIH cells rarely gave rise to tumors. In contrast, despite low infection efficiency (Figure S1F), RIH cells expressing $EZH2^{WT/Y646N}$ formed malignant melanomas, which were fully tdTomato and ZsGreen1 positive (Figures 1E and S1G-S1I). Importantly,

through FACS analysis of lung tissue from tumor-bearing mice, we could identify tdTomato-ZsGreen1-traced cells in this distant organ (Figure S1J). To verify whether EZH2$^{WT/Y646N}$ mediated melanoma formation in conjunction with endogenous murine EZH2, we used primary RIM-1 melanoma cells derived from a *Nras*^{Q61K};*Cdkn2a*$^{-/-}$ animal harboring floxed *Ezh2* alleles (Zingg et al., 2015). ZsGreen1-EZH2$^{WT/Y646N}$-expressing RIM-1 cells were inoculated into immunosuppressed mice (Figures 1F and S1K). Efficient *Ezh2* deletion *in vivo* via tamoxifen (TM) administration compromised RIM-1 tumor growth (Figures 1G and S1L-S1N). However, lack of endogenous *Ezh2* was fully rescued through EZH2^{WT} or EZH2^{Y646N} expression, resulting in growing tumors predominantly comprised of ZsGreen1-traced cells (Figures 1G and S1L-S1O).

Ezh2^{Y646N} induction enhances tumorigenesis in murine models of malignant melanoma

To address whether EZH2 can initiate tumorigenesis in genetically engineered mouse models of melanoma, we used *Nras*^{Q61K};*Cdkn2a*$^{-/-}$ and *Braf*^{V600E};*Pten*$^{-/-}$ mice. In the latter, tumorigenesis is driven by synchronous conditional activation of *Braf*^{V600E} and deletion of *Pten* (Dankort et al., 2009). We bred these animals with *ColA1-LSL-Ezh2*^{Y646N} mice (Béguelin et al., 2013), allowing conditional *Ezh2*^{Y646N} activation (Figure 2A). Topical 4-hydroxytamoxifen administration or intraperitoneal (IP) TM injection (Figure 2B) led to considerable EZH2^{Y646N} expression in *Braf*^{V600E};*Pten*$^{-/-}$ and *Nras*^{Q61K};*Cdkn2a*$^{-/-}$ tumors. This resulted in increased H3K27me3 levels specifically in melanoma cells (Figures S2A-S2C). Proliferation rates were increased in *Braf*^{V600E};*Pten*$^{-/-}$;*Ezh2*^{Y646N} and *Nras*^{Q61K};*Cdkn2a*$^{-/-}$;*Ezh2*^{Y646N} tumor cells as compared to the respective controls (Figures 2C, 2D, and S2D). Consequently, tumors grew faster in *Braf*^{V600E};*Pten*$^{-/-}$;*Ezh2*^{Y646N} mice compared to *Braf*^{V600E};*Pten*$^{-/-}$ controls, resulting in a significantly shortened melanoma-specific survival (Figures 2E and S2E). Activation of *Ezh2*^{Y646N} in *Nras*^{Q61K};*Cdkn2a*$^{-/-}$ mice prior to tumor development (Figure 2B) resulted in both increased and quicker initiation of primary melanomas in comparison to controls (Figures 2F-2H). Inclusion of a *R26R-LSL-tdTomato* allele allowed fate-mapping of dermal hyperplasia cells (Figure 2A). Recombination efficiencies in control and

Ezh2^{Y646N} GoF hyperplasia were about 50%. Accordingly, roughly half of all tumors emerging in *Nras*^{Q61K};*Cdkn2a*$^{-/-}$ animals were tdTomato-positive. However, *Ezh2*^{Y646N} activation strongly increased the emergence of fully recombined melanomas at the expense of tdTomato-negative, non-recombined tumors, reflecting the tumor-promoting activity of EZH2^{Y646N} (Figures 2I–2K).

Ezh2^{Y646N} drives metastatic melanoma from *Braf*^{V600E} and *Nras*^{Q61K} hyperplasia

We next activated *Ezh2*^{Y646N} in *Braf*^{V600E} or *Nras*^{Q61K} animals harboring proficient *Pten* and *Cdkn2a* (Figures 3A and 3B). *Braf*^{V600E} and *Nras*^{Q61K} mice form dermal hyperplasia, but malignant melanoma occurrence is sparse and observed only in mice older than 1 year (Ackermann et al., 2005; Dankort et al., 2009). In absence of *Braf*^{V600E} or *Nras*^{Q61K}, expression of *Ezh2*^{Y646N} affected neither the capacity of melanocytes to populate hair follicle bulbs nor hair pigmentation (Figures S3A-S3D). *Ezh2*^{Y646N} alone was also insufficient to promote melanocytic hyperplasia (Figure 3C). However, in combination with *Nras*^{Q61K}, *Ezh2*^{Y646N} accelerated proliferation of dermal hyperplasia cells (Figure S3E), comparable to the increased proliferation of *Nras*^{Q61K};*Cdkn2a*$^{-/-}$;*Ezh2*^{Y646N} hyperplasia (Figure 2D). This led to enlarged dermal hyperplasia consisting of tdTomato-traced cells in *Nras*^{Q61K};*Ezh2*^{Y646N} skin (Figures 3C and S3F).

Strikingly, with a high incidence, *Ezh2*^{Y646N} drove emergence of malignant melanomas from both benign *Nras*^{Q61K} and *Braf*^{V600E} hyperplasia (Figures 3D, 3E, and S3G). At the day of sacrifice, these mice displayed many more skin melanomas than *Nras*^{Q61K} and *Braf*^{V600E} controls (Figures 3F, 3G, and S3H). In contrast, animals bearing solely *Ezh2*^{Y646N} never developed melanoma, independently of *Pten* or *Cdkn2a* deficiency (Figures 2E, 2H, 3D, and 3G). Of note, *Nras*^{Q61K};*Ezh2*^{Y646N} and *Braf*^{V600E};*Ezh2*^{Y646N} primary melanomas frequently metastasized to lymph nodes (Figures 3H and 3I). Cutaneous tumors and metastases were tdTomato-traced and, across the mouse cohorts, occurrence of metastases strongly correlated with prevalence of primary skin melanomas (Figures 3J-3L and S3I). Taken together, these data

show that, in conjunction with oncogenic *BRAF* or *NRAS* alleles, EZH2 functions as a *bona fide* driver of metastasizing cutaneous melanoma.

EZH2 silences a gene network functionally connected to the primary cilium

To decipher the molecular consequences of a gain of EZH2 in melanomagenesis, we FACS-isolated tdTomato-labeled dermal hyperplasia cells from *Nras*^{Q61K} and *Nras*^{Q61K};*Ezh2*^{Y646N} animals and performed RNA-sequencing (Figures S4A and S4B). Interestingly, among differentially expressed genes, we neither found tumor suppressors, such as *Cdkn1a* or *Cdkn2a* (Table S1), nor did gene ontology (GO) classification of biological processes reveal any terms related to cell cycle (Figure S4C). However, GO biological process and cellular component localization analyses revealed that a significant number of differentially expressed genes encoded proteins locating to the primary cilium (Figures 4A and S4C). The primary cilium is an organelle that projects from the surface of vertebrate cells and is a nexus for several signaling pathways (Goetz and Anderson, 2010). To substantiate a possible connection between PRC2 epigenetics and primary cilium biology, we exploited published genome-wide gene expression profiles that were acquired from two human melanoma cell cultures following RNA interference (RNAi)-mediated *EZH2* silencing (Zingg et al., 2015). In both cell lines, GO cellular component analyses revealed differentially expressed genes to be connected to the primary cilium (Figure S4D). Next, we established a group of genes changed in at least two of the three murine and human data sets (Figure 4B). Cellular component analysis on this subset of genes showed that most of the significantly enriched GO terms were related to primary cilium assembly or function (Figure 4C). According to the SYSCILIA gold standard list of known ciliary components (van Dam et al., 2013), the analyzed gene subset was comprised of about 20% ciliary genes. These were predominantly downregulated upon gain of EZH2^{Y646N} and upregulated after *EZH2* silencing (Figure 4D). Finally, we analyzed global H3K27me3 landscapes of melanoma cells (Verfaillie et al., 2015). In comparison to a set of randomly selected genes, SYSCILIA genes harbored strong H3K27me3 enrichment flanking transcriptional start sites (TSS) (Figures 4E-4G, S4E, and S4F).

To pursue a possible connection between EZH2 activity and ciliary genes, we inhibited EZH2 with GSK503 in a panel of melanoma cell lines. This resulted in loss of H3K27me3 and upregulation of primary cilium genes (Figure S4G-S4J). Chromatin immunoprecipitation (ChIP) for H3K27me3 followed by qPCR revealed that the TSS of many ciliary genes had lost trimethylation of H3K27 upon GSK503 (Figures S4K and S4L). In contrast, expression of both $EZH2^{WT}$ and $EZH2^{Y646N}$ in A375, a melanoma cell line with low H3K27me3 and high expression of ciliary genes (Figures S4H and S4M), resulted in downregulation of primary cilium genes, which was completely reversed when applying GSK503. Consequently, gain in EZH2 provoked reversible H3K27me3 enrichment in ciliary gene TSS (Figure S4N).

To clarify whether increased EZH2 activity *in vivo* would also result in H3K27me3 deposition at cilia loci, we first used RIH tumors induced by $EZH2^{WT/Y646N}$ expression (Figure 1E). ChIP-qPCR revealed TSS of ciliary genes to be enriched in H3K27me3 as compared to negative control sequences (Figure S4O). Next, we FACS-isolated dermal hyperplasia cells from $Nras^{Q61K}$ or $Braf^{V600E}$ mice after $Ezh2^{Y646N}$ activation (Figure S4A). Importantly, ChIP-qPCR showed that, in these benign cells, $Ezh2^{Y646N}$ elicited strong H3K27me3 enrichment in cilia gene TSS. This appeared to be maintained in $Nras^{Q61K}$;$Ezh2^{Y646N}$ tumors (Figure 4H). Accordingly, $Ezh2^{Y646N}$ induced ciliary gene silencing in $Nras^{Q61K}$ and $Braf^{V600E}$ hyperplasia, which was sustained throughout melanomagenesis (Figure 4I). Expression of $Ezh2^{Y646N}$ also led to downregulation of cilia genes in $Nras^{Q61K}$;$Cdkn2a^{-/-}$ and $Braf^{V600E}$;$Pten^{-/-}$ tumors. In contrast, conditional *Ezh2* deletion in established $Nras^{Q61K}$;$Cdkn2a^{-/-}$ melanomas resulted in re-expression of primary cilium genes (Figures S2A, S4P, and S4Q). Finally, within genome expression datasets on human melanocytic lesions, cilia genes were significantly downregulated in primary melanomas and metastases in comparison to benign nevi, a pattern that appeared to anti-correlate with *EZH2* expression (Figure 4J). Thus, during human and murine melanoma formation, EZH2 suppresses genes functionally connected to the primary cilium.

Suppression of ciliary genes by EZH2 mediates primary cilium deconstruction

We analyzed whether, across melanocytic lesions, the identified ciliary gene expression patterns coincided with the extent of ciliation. Indeed, benign nevi were ciliated, while malignant melanomas were mostly devoid of primary cilia (Figures 5A and S5A). In contrast, EZH2 levels were strongly increased in melanomas as compared to nevi, which negatively correlated with the presence of cilia (Figures 5A, 5B, and S5B). To verify whether EZH2-dependent repression of ciliary genes impaired primary cilium integrity, we reverted to melanoma cell cultures. Similar to melanocytes, which form primary cilia in starvation conditions (Le Coz et al., 2014), few of the melanoma cell lines tested were ciliated during starvation. The remaining lines only marginally displayed cilia (Figures 5C and S5C). Across the melanoma cell lines, percentages of ciliated cells correlated positively with the expression levels of primary cilia genes (Figure S4M). Moreover, relative H3K27me3 levels inversely correlated with cellular ciliation (Figure S5D), suggesting an EZH2 activity-dependent regulation of ciliogenesis.

Indeed, EZH2 blockade with GSK503 induced primary cilium formation in most melanoma cell lines (Figure 5C), a process that significantly correlated with increased ciliary gene expression (Figure S4J). In A375, a melanoma cell line with considerable ciliation (Figure 5C), $EZH2^{WT}$ and $EZH2^{Y646N}$ expression comparably provoked cilia deconstruction specifically in transfected ZsGreen1-positive cells. However, EZH2 inhibition restored ciliogenesis despite EZH2 overexpression (Figure 5D). *In vivo*, $Ezh2^{Y646N}$ expression promoted loss of primary cilia in $Braf^{V600E}$;$Pten^{-/-}$ melanomas (Figure 5E). $Nras^{Q61K}$;$Cdkn2a^{-/-}$ tumors already displayed low percentages of ciliation, thus $Ezh2^{Y646N}$ gain did not further suppress cilia formation. In contrast, $Nras^{Q61K}$;$Cdkn2a^{-/-}$ dermal hyperplasia cells were frequently ciliated, comparable to human benign nevi. However, $Ezh2^{Y646N}$ activation strongly reduced primary cilia numbers in $Nras^{Q61K}$;$Cdkn2a^{-/-}$ dermal hyperplasia, while *Ezh2* depletion resulted in ciliogenesis in established tumors (Figures 5F and S5E). Of note, $Ezh2^{Y646N}$ also led to loss of cilia in $Nras^{Q61K}$ dermal hyperplasia long before cutaneous melanoma formation (Figures 5G and S5E). Thus, EZH2-mediated deconstruction of primary cilia might represent an early event in malignant melanoma initiation.

EZH2-mediated primary cilium disassembly augments WNT/β-catenin signaling

A central function of the primary cilium lays in controlling key signaling pathways, especially sonic hedgehog (SHH) and wingless (WNT) signaling (Goetz and Anderson, 2010; Oh and Katsanis, 2013). To examine whether these pathways are controlled by ciliation in melanoma cells, we depleted EZH2-regulated primary cilium genes in ciliated A375 melanoma cells and benign murine RIH cells. Manipulation of *WDR19*, *FUZ*, and *IFT81* elicits cilia deconstruction (Ashe et al., 2012; Bhogaraju et al., 2013; Gray et al., 2009). Accordingly, RNAi-mediated silencing of these genes resulted in loss of primary cilia in A375 cells (Figures S6A and S6B). Likewise, silencing of *Wdr19* and *Kif3a*, a gene encoding a key ciliary component (Marszalek et al., 1999) that was, however, not regulated by EZH2, depleted cilia from RIH cells (Figures S6A and S6C). Treatment of A375 with WNT3A or SHH followed by luciferase reporter assays using constructs containing *TCF/LEF* or *GLI1* promoter sequences showed that loss of primary cilia compromised SHH/GLI signaling, while it strongly enhanced canonical WNT/β-catenin signaling (Figure 6A). Upon cilia depletion, WNT3A also promoted *TCF/LEF* luciferase reporter activity in RIH cells (Figure S6D). In both A375 and RIH cells, elevated WNT signaling was associated with nuclear accumulation of total and especially non-phosphorylated, active β-catenin in deciliated cells (Figures 6B, S6E, and S6F). However, blockade of canonical WNT signaling with the chemical compounds JW55 or PRI-724 (Emami et al., 2004; Waaler et al., 2012) erased deciliation-induced β-catenin activity, as revealed by β-catenin exclusion from the nucleus and reversal of *TCF/LEF* reporter responses (Figures 6B and S6F-S6H).

WNT/β-catenin is an established oncogenic signaling pathway in human melanoma (Xue et al., 2016). Accordingly, nuclei of benign nevus cells were devoid of β-catenin, while malignant melanomas displayed accumulation of nuclear β-catenin (Figures 6C and S6I). Across melanocytic lesions, nuclear β-catenin localization anti-correlated with presence of primary cilia, but significantly correlated with EZH2 expression (Figures 6C, 6D, and S6J). To further dissect the association between WNT/β-catenin signaling

and EZH2-mediated loss of cilia, we expressed EZH2$^{WT/Y646N}$ in A375 and RIH cells. This provoked cilia deconstruction (Figure 5D) and consistently stimulated *TCF/LEF* reporter activity, expression of the WNT signaling reporter gene *AXIN2* (Jho et al., 2002), and nuclear β-catenin accumulation. These responses were suppressed when either EZH2 was inhibited with GSK503 or WNT signaling was blocked using JW55 or PRI-724 (Figures 6E, 6F, and S6K-S6M). *In vivo*, induction of *Ezh2*^{Y646N} resulted in *Axin2* upregulation in *Braf*^{V600E} and *Nras*^{Q61K} hyperplasia, which was maintained in *Nras*^{Q61K};*Ezh2*^{Y646N} tumors (Figure 6G). Likewise, *Ezh2*^{Y646N} activation boosted *Axin2* expression in *Braf*^{V600E};*Pten*$^{-/-}$ and *Nras*^{Q61K};*Cdkn2a*$^{-/-}$ melanomas, whereas *Ezh2* ablation reduced *Axin2* expression in *Nras*^{Q61K};*Cdkn2a*$^{-/-}$ tumors (Figures 6H and S6N). Thus, enhanced EZH2 activity potentiates WNT/β-catenin signaling in benign melanocytic hyperplasia and melanoma.

To functionally link EZH2-mediated deciliation to elevated WNT/β-catenin signaling, we relied on a melanoma cell culture (M130604) with low baseline ciliation but strong cilia induction upon EZH2 blockade (Figure 5C). EZH2 inhibition considerably compromised WNT signal activation in response to WNT3A, as revealed by reduced *TCF/LEF* reporter activity, *AXIN2* expression, and nuclear β-catenin accumulation. Strikingly, silencing of *WDR19* or *FUZ* mediated deciliation and consequently resulted in reactivation of WNT signaling even in the presence of the EZH2 inhibitor GSK503 (Figures 6I and S6O-S6S). However, the canonical WNT inhibitors JW55 and PRI-724 abrogated WNT/β-catenin signaling induction (Figure S6T).

Primary cilium disassembly provokes melanoma cell growth

To investigate the role of the primary cilium in melanomagenesis, we assessed whether cilia deconstruction mediated by ciliary gene depletion affects melanoma cell behavior. We found silencing of *WDR19* and *FUZ* to enhance clonogenicity of human A375 and depletion of *Wdr19* and *Kif3a* to substantially promote colony formation of murine RIH cells (Figures 7A-7C and S7A). Next, we silenced

cilia genes in human melanoma cell cultures, in which EZH2 inhibition strongly induced primary cilium assembly (Figure 5C). Ciliogenesis was reversed through RNAi against ciliary genes (Figures S6O-S6Q). Accordingly, depletion of ciliary genes partially restored cell proliferation despite EZH2 inactivation (Figure S7B), and loss of clonogenicity upon EZH2 blockade was overcome by *WDR19* and *FUZ* silencing (Figures 7D and 7E). Hence, *in vitro*, deciliation counteracts growth suppression induced by EZH2 inhibition.

To elucidate whether this phenotype emerged from enhanced WNT signaling, we suppressed β-catenin activity with JW55 or PRI-724. These inhibitors annihilated clonogenicity of A375 and RIH cells evoked by cilia deconstruction (Figures 7A-7C and S7A). Similarly, in EZH2-inhibited M130604 cells, clonogenicity re-acquired after deciliation was suppressed through WNT signaling inhibition (Figures 7D and 7E). JW55 and PRI-724 also prevented A375 and RIH colony formation induced by $EZH2^{WT/Y646N}$ expression (Figures S7C and S7D). Next, we tested 501Mel melanoma cells, which harbor an endogenous $CTNNB1^{S37F}$ mutation preventing β-catenin phosphorylation and degradation (Rubinfeld et al., 1997). Despite considerable de-repression of ciliary genes and formation of primary cilia upon EZH2 blockade (Figures 5C and S4J), 501Mel cells were resistant to EZH2 inhibition, as revealed by sustained β-catenin activity and colony formation (Figures S7E-S7G). Thus, we stimulated WNT signaling in M130604 cells, either by inducing β-catenin stabilization with the GSK-3 inhibitor Chiron or by expressing non-degradable $CTNNB1^{S33Y}$ (Figures S7H and S7I). M130604 was sensitive to EZH2 blockade by displaying ciliogenesis-dependent loss of β-catenin signaling (Figures 6I and S6O-S6S). Notably, β-catenin stabilization with Chiron as well as $CTNNB1^{S33Y}$ expression significantly reversed the effect of EZH2 inhibition on cell clonogenicity (Figure 7F). Taken together, in benign hyperplasia and malignant melanoma cells, EZH2-mediated primary cilium disassembly appears to promote clonogenicity via β-catenin activation.

Primary cilium deconstruction is a driver of malignant metastatic melanoma

Finally, we aimed to explore whether EZH2-dependent loss of primary cilia and gain in β-catenin is relevant for melanomagenesis *in vivo*. To this end, we suppressed primary cilia via *Wdr19* silencing in primary murine RIM-3 cells (Figures 8A, S8A, and S8B). When inoculated SC into immunocompromised mice, RIM-3 cells maintained *Wdr19* loss *in vivo* (Figure S8C). Daily IP administration of GSK503 counteracted RIM-3 tumor growth. However, *Wdr19* silencing strongly enhanced RIM-3 growth, which was sufficient to completely abrogate tumor growth control mediated by GSK503 (Figures 8B, 8C, and S8D). Interestingly, EZH2 inhibition reduced *Axin2* expression in RIM-3 tumors. In contrast, despite EZH2 blockade, *Wdr19* RNAi-dependent deciliation boosted WNT/β-catenin signaling *in vivo*, as revealed by *Axin2* upregulation (Figure 8D).

Next, we transplanted *Wdr19* and *Kif3a*-depleted RIH cells SC into immunosuppressed mice (Figure 8E). Control RIH cells rarely gave rise to tumors. In contrast, *Wdr19* as well as *Kif3a*-depleted RIH cells readily advanced into tdTomato-GFP double-positive melanomas upon transplantation (Figures 8F-8H and S8E-S8G). These tumors evidently metastasized to the lung, as we FACS-identified tdTomato-GFP-traced cells in this organ (Figures 8I and S8H). We then expressed $CTNNB1^{S33Y}$ in RIH cells (Figures 8E and S8I). SC transplantation of these cells into immunocompromised mice similarly led to emergence of fully tdTomato-GFP traceable metastasizing melanomas (Figures 8J, 8K, and S8J-S8M). Thus, activation of β-catenin signaling *in vivo* was sufficient to initiate melanomagenesis. To verify whether melanoma initiation driven by EZH2 and primary cilium deconstruction was dependent on WNT signaling, we serially passaged tumors that had emerged from RIH cells through $EZH2^{Y646N}$ expression, *Wdr19* silencing, or *Kif3a* silencing (Figures 1E, 8G, and 8H). Daily oral administration of JW55 significantly reduced β-catenin in second-generation RIH tumors (Figures 8L and S8N). Strikingly, canonical WNT signaling inhibition strongly compromised growth of RIH-$EZH2^{Y646N}$, RIH-shWdr19, and RIH-shKif3a melanomas (Figures 8M and S8O). Thus, EZH2 gain and primary cilium deconstruction are key drivers for the initiation of WNT/β-catenin signaling-addicted malignant melanoma *in vivo*.

DISCUSSION

Recent publications have revealed that a large set of solid cancers exhibit loss of primary cilia (Cao and Zhong, 2016), in line with reduced ciliary gene expression (Shpak et al., 2014). However, the mechanisms by which cancer cells lose their cilia and the significance of cilia loss for tumorigenesis have remained elusive. Our study reveals how assembly and disassembly of the primary cilium are epigenetically regulated by PRC2. In particular, we identify the PRC2 component EZH2 to promote tumorigenesis by suppressing primary cilium genes, which results in deciliation. Ciliary deconstruction in turn initiates the formation of metastasizing melanoma by promoting WNT/β-catenin signaling. Thus, the primary cilium functions as a tumor suppressor organelle of malignant metastatic melanoma.

About 67% of human primary melanomas and 56% of melanoma metastases display cytoplasmic or nuclear β-catenin accumulation (Xue et al., 2016). Of note, active β-catenin stimulates emergence of metastasizing melanoma in mice harboring *Braf*^{V600E} or *Nras*^{Q61K} hyperplasia (Damsky et al., 2011; Delmas et al., 2007; Gallagher et al., 2013). In several cancers, β-catenin activity is maintained mostly through genetic aberrations affecting either *CTNNB1* itself or the β-catenin destruction complex member *APC* (Zhan et al., 2017). Although few melanomas harbor somatic *CTNNB1* mutations (Xue et al., 2016), in most melanomas the sources of elevated β-catenin activity are unknown. In this study, we uncovered a mechanism of β-catenin induction that is independent of genetic alterations but relies on PRC2 activity and suppression of the primary cilium. Interestingly, enhanced PRC2 activity also propagates glioblastoma stem cells and initiates dysplasia formation from breast epithelium (Kim et al., 2013; Li et al., 2009). Moreover, in cells of the central nervous system and the mammary gland, depletion of cilia genes stimulates canonical WNT signaling (Oh and Katsanis, 2013), which is crucial for the formation of glioblastoma and breast cancer, respectively (Lee et al., 2016; Yu et al., 2016). Thus, the mechanism of primary cilium disruption discovered here could maintain oncogenic WNT/β-catenin signaling not only in a large portion of human melanomas but also in tumors of brain and breast.

Contrary to cutaneous melanoma, malignant peripheral nerve sheath tumors (MPNSTs) harbor LoF mutations abolishing PRC2 activity (De Raedt et al., 2014). Whether these tumors are ciliated is unknown. However, MPNSTs show a signature of elevated SHH signaling (Lévy et al., 2004), a pathway that strongly relies on the primary cilium (Goetz and Anderson, 2010). Likewise, emergence of basal cell carcinoma and medulloblastoma is dependent on both oncogenic SHH signaling and functional cilia (Han et al., 2009; Wong et al., 2009). Of note, *Ezh2* deletion in a mouse model of medulloblastoma accelerates tumorigenesis (Vo et al., 2017). Upon disassembly of primary cilia via EZH2, we observed abrogated SHH signaling, whereas WNT signaling was enhanced. Interestingly, SHH-WNT antagonisms are required for neural tube morphogenesis as much as epidermal stem cell expansion (Ouspenskaia et al., 2016; Ulloa and Briscoe, 2007), while the primary cilium counteractively controls these two signaling pathways (Goetz and Anderson, 2010; Oh and Katsanis, 2013). Taken together, acquiring either gain or loss of PRC2 might allow cancers to manipulate the primary cilium, thus ultimately skewing the SHH-WNT interplay towards the preferential oncogenic signaling pathway.

Recent immunotherapeutic advancements have resulted in remarkable clinical responses in some melanoma patients. However, the remaining patients frequently acquire resistance to immunotherapies (Sharma et al., 2017). Distinctive mechanisms in suppressing anti-tumor immunity involve tumor-intrinsic PRC2 activity as well as WNT/β-catenin signaling (Spranger et al., 2015; Zingg et al., 2017). Moreover, physical contact between cytotoxic T-cells and tumor cells depends on the formation of the cytolytic synapse. Assembly of that structure involves many of the proteins required for primary ciliogenesis (de la Roche et al., 2016). In principle, EZH2 could therefore foster immune escape by suppressing cytolytic synapses or primary cilium formation, the latter potentially increasing immunosuppressive WNT signaling. Several EZH2 inhibitors have entered clinical trials (Kim and Roberts, 2016). Thus, EZH2-targeting might conceivably be considered as a strategy for treating melanoma, possibly in combination with immunotherapies.

SUPPLEMENTAL INFORMATION

Supplemental Information includes eight figures and two tables and can be found with this article online at …

ACKNOWLEDGMENTS

We thank M. van den Broek, the Flow Cytometry Facility, and the Functional Genomics Center Zurich (University of Zurich) for experimental support. We thank F. Beermann (EPFL, Switzerland), H. Koseki (RIKEN Center for Integrative Medical Sciences, Japan), and M. Serrano (Centro Nacional de Investigaciones Oncologicas, Spain) for providing *Tyr::Nras*^{Q61K}, *Ezh2*^{lox}, and *Cdkn2a*$^{-/-}$ mice. We thank A. Melnick (Weill Cornell Medical College, USA) and M. T. McCabe (GlaxoSmithKline, USA) for providing EZH2 plasmids and GSK503. This work was funded by the Swiss National Science Foundation (R.S. and L.S.), including a Sinergia grant (K.B. and L.S.), the Swiss Cancer League (L.S.), the Zurich Cancer League (R.S.), and the Zurich University Research Priority Program "Translational Cancer Research" (K.B., R.D., M.P.L., and L.S.).

AUTHOR CONTRIBUTIONS

Conceptualization, D.Z. and L.S.; Methodology, D.Z. and R.P.-H.; Formal Analysis; D.Z., R.P.-H., and P.F.C., and R.R.C.; Investigation, D.Z., J.D., R.P.-H., A.T.A., S.M.S., D.Zim., J.H., E.T., Y.Z., and R.B.; Resources, K.-K.W., K.B., R.D., and M.P.L.; Writing, D.Z. and L.S.; Visualization, A.T.A.; Supervision, R.S. and L.S.; Funding Acquisition, K.B., R.D., R.S., M.P.L., and L.S.

DECLARATION OF INTERESTS

The authors declare no competing interests.

REFERENCES

Ackermann, J., Frutschi, M., Kaloulis, K., McKee, T., Trumpp, A., and Beermann, F. (2005). Metastasizing melanoma formation caused by expression of activated N-RasQ61K on an INK4a-deficient background. Cancer Res. *65*, 4005–4011.

Albers, J., Danzer, C., Rechsteiner, M., Lehmann, H., Brandt, L.P., Hejhal, T., Catalano, A., Busenhart, P., Gonçalves, A.F., Brandt, S., et al. (2015). A versatile modular vector system for rapid combinatorial mammalian genetics. J. Clin. Invest. *125*, 1603–1619.

Ashe, A., Butterfield, N.C., Town, L., Courtney, A.D., Cooper, A.N., Ferguson, C., Barry, R., Olsson, F., Liem, K.F., Parton, R.G., et al. (2012). Mutations in mouse Ift144 model the craniofacial, limb and rib defects in skeletal ciliopathies. Hum. Mol. Genet. *21*, 1808–1823.

Béguelin, W., Popovic, R., Teater, M., Jiang, Y., Bunting, K.L., Rosen, M., Shen, H., Yang, S.N., Wang, L., Ezponda, T., et al. (2013). EZH2 Is Required for Germinal Center Formation and Somatic EZH2 Mutations Promote Lymphoid Transformation. Cancer Cell *23*, 677–692.

Berg, T., Thoene, S., Yap, D., Wee, T., Schoeler, N., Rosten, P., Lim, E., Bilenky, M., Mungall, A.J., Oellerich, T., et al. (2014). A transgenic mouse model demonstrating the oncogenic role of mutations in the polycomb-group gene EZH2 in lymphomagenesis. Blood *123*, 3914–3924.

Bhogaraju, S., Cajanek, L., Fort, C., Blisnick, T., Weber, K., Taschner, M., Mizuno, N., Lamla, S., Bastin, P., Nigg, E.A., et al. (2013). Molecular basis of tubulin transport within the cilium by IFT74 and IFT81. Science *341*, 1009–1012.

Bolger, A.M., Lohse, M., and Usadel, B. (2014). Trimmomatic: a flexible trimmer for Illumina sequence data. Bioinformatics *30*, 2114–2120.

Cao, M., and Zhong, Q. (2016). Cilia in autophagy and cancer. Cilia *5*, 4.

Carpenter, A.E., Jones, T.R., Lamprecht, M.R., Clarke, C., Kang, I.H., Friman, O., Guertin, D. a, Chang, J.H., Lindquist, R. a, Moffat, J., et al. (2006). CellProfiler: image analysis software for identifying and quantifying cell phenotypes. Genome Biol. *7*, R100.

Le Coz, M., Benmerah, A., and Larue, L. (2014). Quiescent melanocytes form primary cilia. Exp. Dermatol. *23*, 426–427.

van Dam, T.J., Wheway, G., Slaats, G.G., Huynen, M.A., and Giles, R.H. (2013). The SYSCILIA gold standard (SCGSv1) of known ciliary components and its applications within a systems biology consortium. Cilia *2*, 7.

Damsky, W.E., Curley, D.P., Santhanakrishnan, M., Rosenbaum, L.E., Platt, J.T., Gould Rothberg, B.E., Taketo, M.M., Dankort, D., Rimm, D.L., McMahon, M., et al. (2011). β-Catenin Signaling Controls Metastasis in Braf-Activated Pten-Deficient Melanomas. Cancer Cell *20*, 741–754.

Dankort, D., Curley, D.P., Cartlidge, R.A., Nelson, B., Karnezis, A.N., Damsky Jr., W.E., You, M.J., DePinho, R.A., McMahon, M., and Bosenberg, M. (2009). Braf(V600E) cooperates with Pten loss to induce metastatic melanoma. Nat. Genet. *41*, 544–552.

Delmas, V., Beermann, F., Martinozzi, S., Carreira, S., Ackermann, J., Kumasaka, M., Denat, L., Goodall, J., Luciani, F., Viros, A., et al. (2007). beta-Catenin induces immortalization of melanocytes by suppressing p16INK4a expression and cooperates with N-Ras in melanoma development. Genes Dev. *21*, 2923–2935.

Dobin, A., Davis, C.A., Schlesinger, F., Drenkow, J., Zaleski, C., Jha, S., Batut, P., Chaisson, M., and Gingeras, T.R. (2013). STAR: ultrafast universal RNA-seq aligner. Bioinformatics *29*, 15–21.

Emami, K.H., Nguyen, C., Ma, H., Kim, D.H., Jeong, K.W., Eguchi, M., Moon, R.T., Teo, J.-L., Oh, S.W., Kim, H.Y., et al. (2004). A small molecule inhibitor of β-catenin/CREB-binding protein transcription. Proc. Natl. Acad. Sci. *101*, 12682–12687.

Gallagher, S.J., Rambow, F., Kumasaka, M., Champeval, D., Bellacosa, A., Delmas, V., and Larue, L. (2013). Beta-catenin inhibits melanocyte migration but induces melanoma metastasis. Oncogene *32*, 2230–2238.

Gilfillan, G.D., Hughes, T., Sheng, Y., Hjorthaug, H.S., Straub, T., Gervin, K., Harris, J.R., Undlien, D.E., and Lyle, R. (2012). Limitations and possibilities of low cell number ChIP-seq. BMC Genomics *13*, 645.

Goetz, S.C., and Anderson, K. V (2010). The Primary Cilium: A Signaling Center During Vertebrate Development. Nat. Rev. Genet. *11*, 331–344.

Gray, R.S., Abitua, P.B., Wlodarczyk, B.J., Szabo-Rogers, H.L., Blanchard, O., Lee, I., Weiss, G.S., Liu, K.J., Marcotte, E.M., Wallingford, J.B., et al. (2009). The planar cell polarity effector Fuz is essential for targeted membrane trafficking, ciliogenesis and mouse embryonic development. Nat. Cell Biol. *11*, 1225–1232.

Han, Y.-G., Kim, H.J., Dlugosz, A.A., Ellison, D.W., Gilbertson, R.J., and Alvarez-Buylla, A. (2009). Dual and opposing roles of primary cilia in medulloblastoma development. Nat. Med. *15*, 1062–1065.

Hirabayashi, Y., Suzki, N., Tsuboi, M., Endo, T.A., Toyoda, T., Shinga, J., Koseki, H., Vidal, M., and Gotoh, Y. (2009). Polycomb Limits the Neurogenic Competence of Neural Precursor Cells to Promote Astrogenic Fate Transition. Neuron *63*, 600–613.

Jho, E., Zhang, T., Domon, C., Joo, C.-K., Freund, J.-N., and Costantini, F. (2002). Wnt/beta-catenin/Tcf signaling induces the transcription of Axin2, a negative regulator of the signaling pathway. Mol. Cell. Biol. *22*, 1172–1183.

Kabbarah, O., Nogueira, C., Feng, B., Nazarian, R.M., Bosenberg, M., Wu, M., Scott, K.L., Kwong, L.N., Xiao, Y., Cordon-Cardo, C., et al. (2010). Integrative Genome Comparison of Primary and Metastatic Melanomas. PLoS One *5*, e10770.

Kent, W.J., Sugnet, C.W., Furey, T.S., Roskin, K.M., Pringle, T.H., Zahler, A.M., and Haussler, a. D. (2002). The Human Genome Browser at UCSC. Genome Res. *12*, 996–1006.

Kim, K.H., and Roberts, C.W.M. (2016). Targeting EZH2 in cancer. Nat. Med. *22*, 128–134.

Kim, E., Kim, M., Woo, D.-H., Shin, Y., Shin, J., Chang, N., Oh, Y.T., Kim, H., Rheey, J., Nakano, I., et al. (2013). Phosphorylation of EZH2 Activates STAT3 Signaling via STAT3 Methylation and Promotes Tumorigenicity of Glioblastoma Stem-like Cells. Cancer Cell *23*, 839–852.

Koppens, M.A.J., Tanger, E., Nacerddine, K., Westerman, B., Song, J.-Y., and van Lohuizen, M. (2017). A new transgenic mouse model for conditional overexpression of the Polycomb Group protein EZH2. Transgenic Res. *26*, 187–196.

de la Roche, M., Asano, Y., and Griffiths, G.M. (2016). Origins of the cytolytic synapse. Nat. Rev. Immunol. *16*, 421–432.

Lawrence, M., Huber, W., Pagès, H., Aboyoun, P., Carlson, M., Gentleman, R., Morgan, M.T., and Carey, V.J. (2013). Software for Computing and Annotating Genomic Ranges. PLoS Comput. Biol. *9*, e1003118.

Lee, Y., Lee, J.-K., Ahn, S.H., Lee, J., and Nam, D.-H. (2016). WNT signaling in glioblastoma and therapeutic opportunities. Lab. Investig. *96*, 137–150.

Lévy, P., Vidaud, D., Leroy, K., Laurendeau, I., Wechsler, J., Bolasco, G., Parfait, B., Wolkenstein, P., Vidaud, M., and Bièche, I. (2004). Molecular profiling of malignant peripheral nerve sheath tumors associated with neurofibromatosis type 1, based on large-scale real-time RT-PCR. Mol. Cancer *3*, 20.

Li, L.-C., and Dahiya, R. (2002). MethPrimer: designing primers for methylation PCRs. Bioinformatics *18*, 1427–1431.

Li, X., Gonzalez, M.E., Toy, K., Filzen, T., Merajver, S.D., and Kleer, C.G. (2009). Targeted Overexpression of EZH2 in the Mammary Gland Disrupts Ductal Morphogenesis and Causes Epithelial Hyperplasia. Am. J. Pathol. *175*, 1246–1254.

Marszalek, J.R., Ruiz-Lozano, P., Roberts, E., Chien, K.R., and Goldstein, L.S. (1999). Situs inversus and embryonic ciliary morphogenesis defects in mouse mutants lacking the KIF3A subunit of kinesin-II. Proc. Natl. Acad. Sci. *96*, 5043–5048.

Mi, H., Muruganujan, A., Casagrande, J.T., and Thomas, P.D. (2013). Large-scale gene function analysis with the PANTHER classification system. Nat. Protoc. *8*, 1551–1566.

Oh, E.C., and Katsanis, N. (2013). Context-Dependent Regulation of Wnt Signaling through the Primary Cilium. J. Am. Soc. Nephrol. *24*, 10–18.

Ouspenskaia, T., Matos, I., Mertz, A.F., Fiore, V.F., and Fuchs, E. (2016). WNT-SHH Antagonism Specifies and Expands Stem Cells prior to Niche Formation. Cell *164*, 156–169.

De Raedt, T., Beert, E., Pasmant, E., Luscan, A., Brems, H., Ortonne, N., Helin, K., Hornick, J.L., Mautner, V., Kehrer-Sawatzki, H., et al. (2014). PRC2 loss amplifies Ras-driven transcription and confers sensitivity to BRD4-based therapies. Nature *514*, 247–251.

Ramírez, F., Ryan, D.P., Grüning, B., Bhardwaj, V., Kilpert, F., Richter, A.S., Heyne, S., Dündar, F., and Manke, T. (2016). deepTools2: a next generation web server for deep-sequencing data analysis. Nucleic Acids Res. *44*, W160–W165.

Robinson, J.T., Thorvaldsdóttir, H., Winckler, W., Guttman, M., Lander, E.S., Getz, G., and Mesirov, J.P. (2011). Integrative genomics viewer. Nat. Biotechnol. *29*, 24–26.

Robinson, M.D., McCarthy, D.J., and Smyth, G.K. (2010). edgeR: a Bioconductor package for differential expression analysis of digital gene expression data. Bioinformatics *26*, 139–140.

Rubinfeld, B., Robbins, P., El-Gamil, M., Albert, I., Porfiri, E., and Polakis, P. (1997). Stabilization of beta-catenin by genetic defects in melanoma cell lines. Science *275*, 1790–1792.

Scatolini, M., Grand, M.M., Grosso, E., Venesio, T., Pisacane, A., Balsamo, A., Sirovich, R., Risio, M., and Chiorino, G. (2010). Altered molecular pathways in melanocytic lesions. Int. J. Cancer *126*, 1869–1881.

Schneider, C.A., Rasband, W.S., and Eliceiri, K.W. (2012). NIH Image to ImageJ: 25 years of image analysis. Nat. Methods *9*, 671–675.

Serrano, M., Lee, H.W., Chin, L., Cordon-Cardo, C., Beach, D., and DePinho, R.A. (1996). Role of the INK4a locus in tumor suppression and cell mortality. Cell *85*, 27–37.

Sharma, P., Hu-Lieskovan, S., Wargo, J.A., and Ribas, A. (2017). Primary, Adaptive, and Acquired Resistance to Cancer Immunotherapy. Cell *168*, 707–723.

Shpak, M., Goldberg, M.M., and Cowperthwaite, M.C. (2014). Cilia gene expression patterns in cancer. Cancer Genomics Proteomics *11*, 13–24.

Smith, A.P., Hoek, K., and Becker, D. (2005). Whole-genome expression profiling of the melanoma progression pathway reveals marked molecular differences between nevi/melanoma in situ and advanced-stage melanomas. Cancer Biol. Ther. *4*, 1018–1029.

Souroullas, G.P., Jeck, W.R., Parker, J.S., Simon, J.M., Liu, J., Paulk, J., Xiong, J., Clark, K.S., Fedoriw, Y., Qi, J., et al. (2016). An oncogenic Ezh2 mutation induces tumors through global redistribution of histone 3 lysine 27 trimethylation. Nat. Med. *22*, 632–640.

Spranger, S., Bao, R., and Gajewski, T.F. (2015). Melanoma-intrinsic β-catenin signalling prevents anti-tumour immunity. Nature *523*, 231–235.

Talantov, D., Mazumder, A., Yu, J.X., Briggs, T., Jiang, Y., Backus, J., Atkins, D., and Wang, Y. (2005). Novel genes associated with malignant melanoma but not benign melanocytic lesions. Clin. Cancer Res. *11*, 7234–7242.

TCGA Network (2015). Genomic Classification of Cutaneous Melanoma. Cell *161*, 1681–1696.

Ulloa, F., and Briscoe, J. (2007). Morphogens and the Control of Cell Proliferation and Patterning in the Spinal Cord. Cell Cycle *6*, 2640–2649.

Valenta, T., Gay, M., Steiner, S., Draganova, K., Zemke, M., Hoffmans, R., Cinelli, P., Aguet, M., Sommer, L., and Basler, K. (2011). Probing transcription-specific outputs of β-catenin in vivo. Genes Dev. *25*, 2631–2643.

Verfaillie, A., Imrichova, H., Atak, Z.K., Dewaele, M., Rambow, F., Hulselmans, G., Christiaens, V., Svetlichnyy, D., Luciani, F., Van den Mooter, L., et al. (2015). Decoding the regulatory landscape of melanoma reveals TEADS as regulators of the invasive cell state. Nat. Commun. *6*, 6683.

Vo, B.T., Li, C., Morgan, M.A., Theurillat, I., Finkelstein, D., Wright, S., Hyle, J., Smith, S.M.C., Fan, Y., Wang, Y.-D., et al. (2017). Inactivation of Ezh2 Upregulates Gfi1 and Drives Aggressive Myc-Driven Group 3 Medulloblastoma. Cell Rep. *18*, 2907–2917.

Waaler, J., Machon, O., Tumova, L., Dinh, H., Korinek, V., Wilson, S.R., Paulsen, J.E., Pedersen, N.M., Eide, T.J., Machonova, O., et al. (2012). A Novel Tankyrase Inhibitor Decreases Canonical Wnt Signaling in Colon Carcinoma Cells and Reduces Tumor Growth in Conditional APC Mutant Mice. Cancer Res. *72*, 2822–2832.

Wong, S.Y., Seol, A.D., So, P.-L., Ermilov, A.N., Bichakjian, C.K., Epstein, E.H., Dlugosz, A. a, and Reiter, J.F. (2009). Primary cilia can both mediate and suppress Hedgehog pathway–dependent tumorigenesis. Nat. Med. *15*, 1055–1061.

Xue, G., Romano, E., Massi, D., and Mandalà, M. (2016). Wnt/β-catenin signaling in melanoma: Preclinical rationale and novel therapeutic insights. Cancer Treat. Rev. *49*, 1–12.

Ye, J., Coulouris, G., Zaretskaya, I., Cutcutache, I., Rozen, S., and Madden, T.L. (2012). Primer-BLAST: A tool to design target-specific primers for polymerase chain reaction. BMC Bioinformatics *13*, 134.

Yu, Q., Verheyen, E., and Zeng, Y. (2016). Mammary Development and Breast Cancer: A Wnt Perspective. Cancers (Basel). *8*, 65.

Zhan, T., Rindtorff, N., and Boutros, M. (2017). Wnt signaling in cancer. Oncogene *36*, 1461–1473.

Zhang, H., Qi, J., Reyes, J.M., Li, L., Rao, P.K., Li, F., Lin, C.Y., Perry, J.A., Lawlor, M.A., Federation, A., et al. (2016). Oncogenic Deregulation of EZH2 as an Opportunity for Targeted Therapy in Lung Cancer. Cancer Discov. *6*, 1006–1021.

Zingg, D., Debbache, J., Schaefer, S.M., Tuncer, E., Frommel, S.C., Cheng, P., Arenas-Ramirez, N., Haeusel, J., Zhang, Y., Bonalli, M., et al. (2015). The epigenetic modifier EZH2 controls melanoma growth and metastasis through silencing of distinct tumour suppressors. Nat. Commun. *6*, 6051.

Zingg, D., Arenas-Ramirez, N., Sahin, D., Rosalia, R.A., Antunes, A.T., Haeusel, J., Sommer, L., and Boyman, O. (2017). The Histone Methyltransferase Ezh2 Controls Mechanisms of Adaptive

Resistance to Tumor Immunotherapy. Cell Rep. *20*, 854–867.

FIGURE LEGENDS

Figure 1. EZH2 overexpression accelerates melanomagenesis

(A) *EZH2* mRNA expression in TCGA human skin cutaneous melanoma (SKCM) dataset segregated according to *EZH2* copy numbers. Copy numbers, n < 2, 15 specimens; n = 2, 101 specimens; n > 2, 162 specimens. RPKM, reads per kilobase million.

(B) *EZH2* mRNA expression in nevus (ne) and melanoma (me) datasets. GSE4587 (ne, n = 4; me, n = 9), GSE3189 (ne, n = 18; me, n = 45), GSE12391 (ne, n = 29; me, n = 23), GSE46517 (ne, n = 9; me, n = 104). NE, normalized expression.

(C) Clonogenicity of A375 transfected with empty vector, $EZH2^{WT}$, or $EZH2^{Y646N}$-expression plasmids and treated with GSK503. n = 3 independent experiments.

(D) Strategy used to infect RIH cells with retro-empty vector, $EZH2^{WT}$, or $EZH2^{Y646N}$ and transplant into Nude-*Foxn1*$^{nu/nu}$ mice.

(E) Tumor growth curves of mice in (D). Empty vector, $EZH2^{WT}$, each n = 8; $EZH2^{Y646N}$, each n = 7 mice.

(F) Strategy used to infect RIM-1 cells with retro-empty vector, $EZH2^{WT}$, or $EZH2^{Y646N}$, transplant into Nude mice, and treat with vehicle or tamoxifen (TM) to delete *Ezh2*.

(G) Tumor growth curves of mice in (F). n = 5 mice per group.

Data are represented as median ± interquartile range (box) and ± 100% range (whiskers) (A and B) or as mean ± standard error of the mean (SEM) (C and G). p values calculated with analysis of variance (ANOVA) and Fisher's least significant difference (LSD) test (A, C, and G) or unpaired Student's *t*-test (B). NS, not significant, *p < 0.05, **p < 0.01, ***p < 0.001, ****p < 0.0001. See also Figure S1.

Figure 2. *Ezh2*^{Y646N} promotes murine melanoma formation

(A and B) Mouse genotypes (A) and strategies (B) used to analyze the effects of conditional *Ezh2*^{Y646N} activation in the melanocytic lineage of adult *Braf*^{V600E};*Pten*$^{-/-}$ or *Nras*^{Q61K};*Cdkn2a*$^{-/-}$ mice. 4-OHT, 4-hydroxytamoxifen.

(C and D) Quantification of proliferative cells in tumors of *Braf*^{V600E};*Pten*$^{-/-}$ (C), n = 5 of 5; *Braf*^{V600E};*Pten*$^{-/-}$;*Ezh2*^{Y646N} (C), n = 6 of 6; *Nras*^{Q61K};*Cdkn2a*$^{-/-}$ (D), n = 12 of 9; and *Nras*^{Q61K};*Cdkn2a*$^{-/-}$;*Ezh2*^{Y646N} (D) n = 12 of 10 mice. Hyperplasia in (D), each n = 5 of 5 mice.

(E) Kaplan-Meier curves comparing melanoma-specific survival of *Pten*$^{-/-}$;*Ezh2*^{Y646N}, n = 3; *Braf*^{V600E};*Pten*$^{-/-}$, n = 12; and *Braf*^{V600E};*Pten*$^{-/-}$;*Ezh2*^{Y646N}, n = 8 mice.

(F) Melanoma count at time point of sacrifice. *Cdkn2a*$^{-/-}$;*Ezh2*^{Y646N}, n = 5; *Nras*^{Q61K};*Cdkn2a*$^{-/-}$, n = 31; and *Nras*^{Q61K};*Cdkn2a*$^{-/-}$;*Ezh2*^{Y646N}, n = 21 mice.

(G) *Nras*^{Q61K};*Cdkn2a*$^{-/-}$ and *Nras*^{Q61K};*Cdkn2a*$^{-/-}$;*Ezh2*^{Y646N} animal 3 months post TM.

(H) Kaplan-Meier curves comparing melanoma-free survival. Mouse numbers as in (F).

(I–K) Immunofluorescence staining for PAX3 and tdTomato (exemplified by *Nras*^{Q61K};*Cdkn2a*$^{-/-}$;*Ezh2*^{Y646N} samples) (I) and quantification of recombination efficiencies (J) and recombination categories (K). D, dermis; E, epidermis. Arrowhead, PAX3^{+} tdTomato^{+} cell; empty arrowhead, PAX3^{+} tdTomato^{-} cell. Scale bars, 50 μm. Hyperplasia, each n = 10 of 10 mice. Tumors, *Nras*^{Q61K};*Cdkn2a*$^{-/-}$, n = 25 of 16 (J), n = 36 of 21 (K); and *Nras*^{Q61K};*Cdkn2a*$^{-/-}$;*Ezh2*^{Y646N}, n = 35 (J), n = 49 (K) of 19 mice.

Data are represented as mean ± SEM (C, D, and F) or as mean ± 100% range (J). p values calculated with unpaired Student's *t*-test (C and F), ANOVA and Fisher's LSD test (D and J), or log-rank (Mantel-Cox) test (E and H). See also Figure S2.

Figure 3. *Ezh2*^{Y646N} is a driver of murine metastatic melanoma

(A and B) Mouse genotypes (A) and strategies (B) used to analyze the effects of conditional *Ezh2*^{Y646N} expression in the melanocytic lineage of adult *Braf*^{V600E} and *Nras*^{Q61K} mice.

(C) Immunofluorescence staining for DCT to quantify hyperplasia size 5 months post TM. HF, hair follicle. Scale bars, 50 μm. Mouse numbers, WT, *Ezh2*^{Y646N}, n = 2; *Nras*^{Q61K}, n = 3; *Nras*^{Q61K};*Ezh2*^{Y646N}, n = 4.

(D and E) Kaplan-Meier curves comparing melanoma-free survival of *Ezh2*^{Y646N} (D), n = 5; *Nras*^{Q61K} (D), n = 30; *Nras*^{Q61K};*Ezh2*^{Y646N} (D), n = 15; *Braf*^{V600E} (E), n = 29; and *Braf*^{V600E};*Ezh2*^{Y646N} (E), n = 24 mice.

(F–I) Immunofluorescence staining for tdTomato on dorsal skin (F) and lymph nodes (LNs) (H) to quantify skin tumors (G) and metastatic burden (I). Scale bars, 1 mm. Mouse numbers as in (D and E).

(J) Quantifications of recombination efficiencies in skin tumors and LN metastases. Each, n = 10 of 10 mice.

(K and L) Bar plots summarizing correlation between skin tumors and LN metastases within mouse cohorts from (D and E).

Data are represented as median ± interquartile range (box) and ± 100% range (whiskers) (C) or as mean ± SEM (G, I, and J). p values calculated with unpaired Student's *t*-test (C, G, and I), log-rank (Mantel-Cox) test (D and E), or Spearman's rank correlation coefficient (r_S) (K and L). See also Figure S3.

Figure 4. EZH2 suppresses transcription of primary cilium genes

(A) PANTHER GO-slim cellular component analysis using Overrepresentation Test and Fisher's Exact test with FDR multiple test correction on RNA-seq data from murine FACS-isolated *Nras*^{Q61K};*Ezh2*^{Y646N} versus (vs.) *Nras*^{Q61K} hyperplasia cells.

(B) Genes commonly changed in *Nras*^{Q61K};*Ezh2*^{Y646N} vs. *Nras*^{Q61K} RNA-seq and in microarrays on M010817 and M050829 human melanoma cell cultures after *EZH2* RNAi (GSE63165).

(C) PANTHER GO cellular component complete analysis using Overrepresentation Test and Bonferroni correction on genes changed in $n \geq 2$ of the datasets in (B).

(D) Overlap of SYSCILIA genes and genes changed in $n \geq 2$ of the datasets in (B), and heatmap depicting fold changes (FCs) of these genes. Colored squares, significant FCs over *Nras*^{Q61K} cells ($p < 0.01$) or siCo transfected cells ($p < 0.05$).

(E and F) Heatmaps (E) and enrichment plots (F) showing normalized read densities of H3K27me3 at the transcription start site (TSS) of SYSCILA and random genes (each n = 760) in MM034 (E and F) and MM118 (F) human melanoma cell cultures (GSE60666). Tracks are centered to the TSS and extend ± 5 Kb.

(G) Genome browser tracks showing H3K27me3 at *WDR19* and *TULP3* loci in human melanoma cell cultures (GSE60666).

(H) Heatmaps showing H3K27me3 enrichments flanking TSS of ciliary genes in murine samples and p values from comparisons of individual groups. ChIP-qPCR normalized to input and H3K27me3 enrichment in *Rpl30* Intron 2 (I2) and intergenic region 1 (Interg1) of *Nras*^{Q61K} and *Braf*^{V600E} hyperplasia samples. Hyperplasia, each n = 5 of 5 mice; Tumors, n = 4 of 3 mice.

(I) Heatmaps showing ciliary gene FCs in murine samples and p values from comparisons of individual groups. *Nras*^{Q61K}, *Nras*^{Q61K};*Ezh2*^{Y646N} hyperplasia, n = 6 of 6; *Nras*^{Q61K};*Ezh2*^{Y646N} tumors, n = 4 of 3; and *Braf*^{V600E}, *Braf*^{V600E};*Ezh2*^{Y646N} hyperplasia, n = 4 of 4 mice.

(J) Heatmaps showing *EZH2* and ciliary gene FCs in nevus and melanoma datasets and p values from comparisons of individual groups. N/A, not available. Datasets as in Figure 1B.

p values calculated with ANOVA and Fisher's LSD test (G, H, and I). See also Figure S4 and Table S1.

Figure 5. EZH2 expression leads to deconstruction of the primary cilium organelle

(A and B) Immunofluorescence staining for MART1, acetylated tubulin (AcTub), and EZH2 on melanocytic lesions (A) to correlate ciliation and nuclear EZH2 intensity (B). Arrowhead, MART1^{+} AcTub (cilia)$^{+}$ EZH2^{low} cell; empty arrowhead, MART1^{+} AcTub$^{–}$ EZH2^{high} cell. Nevi, congenital, intradermal, each n = 3; junctional, compound, each n = 4; Primary melanomas, n = 8; Metastases, skin, lymph node, each n = 5; distant, n = 7.

(C) Immunofluorescence staining for ARL13B and PCNT to quantify ciliated melanoma cells during GSK503 treatment.

(D) Endogenous ZsGreen1 (EZH2 expression vector) fluorescence and immunofluorescence staining for ARL13B and PCNT to quantify ciliated A375 cells transfected with empty vector, EZH2^{WT}, or EZH2^{Y646N}-expression plasmids and treated with GSK503.

(E–G) Immunofluorescence stainings for ARL13B and SOX10, DCT, tdTomato, or β-Gal to quantify ciliated melanocytic cells. Arrowhead, ARL13B (cilia)$^{+}$ and SOX10^{+}, DCT^{+}, tdTomato^{+}, or β-Gal^{+} cell; empty arrowhead, ARL13B$^{–}$ and SOX10^{+}, DCT^{+}, or tdTomato^{+} cell. Tumors, *Braf*^{V600E};*Pten*$^{–/–}$, n = 5 of 5; and *Braf*^{V600E};*Pten*$^{–/–}$;*Ezh2*^{Y646N}, *n* = 6 of 6 mice (E). Tumors and adjacent hyperplasia, *Nras*^{Q61K};*Cdkn2a*$^{–/–}$, n = 8 of 7; *Nras*^{Q61K};*Cdkn2a*$^{–/–}$;*Ezh2*^{Y646N}, n = 8 of 8; and *Nras*^{Q61K};*Cdkn2a*$^{–/–}$;*Ezh2*$^{–/–}$, n = 8 of 5 mice (F). *Nras*^{Q61K}, *Nras*^{Q61K};*Ezh2*^{Y646N} hyperplasia (5 months post TM), n = 6 of 6; and *Nras*^{Q61K};*Ezh2*^{Y646N} tumors (endpoint), n = 8 of 6 mice (G).

Scale bars, 25 μm. Data are represented as mean ± standard deviation (SD) (B) or mean ± SEM (C–G) of 4 independent experiments (C and D). p values calculated with Spearman's r_S (B), unpaired Student's *t*-test (C and E), or ANOVA and Fisher's LSD test (D, F, and G). See also Figure S5.

Figure 6. Loss of primary cilia induces WNT/β-catenin signaling

(A) Luciferase reporter assays on A375 co-transfected with siCo, siWDR19, or siFUZ and empty vector, *TCF/LEF*, or *GLI1* reporter plasmid after 3 hr stimulation with vehicle, WNT3A, or SHH. Relative luciferase units (RLU) calculated by normalizing firefly luciferase to Renilla luciferase luminescence.

(B) Western blots for total and non-phosphorylated (nonP) β-catenin on cytoplasmic and nuclear fractions of A375 transfected with siCo, siWDR19, or siFUZ, treated with JW55, and stimulated with WNT3A.

(C and D) Immunofluorescence staining for MART1, AcTub, and β-catenin on melanocytic lesions (C) to correlate ciliation and nuclear β-catenin localization (D). Arrowhead, MART1^{+} AcTub^{+} β-catenin^{low} cell; empty arrowhead, MART1^{+} AcTub^{-} β-catenin^{high} cell. Sample numbers as in Figure 5B.

(E) Western blots for EZH2, H3K27me3, total, and nonP-β-catenin on cytoplasmic and nuclear fractions of A375 transfected with empty vector, EZH2^{WT}, or EZH2^{Y646N}-expression plasmids, treated with GSK503 and JW55, and stimulated with WNT3A.

(F) Luciferase reporter assays on RIH cells co-transfected with empty vector, EZH2^{WT}, or EZH2^{Y646N}-expression and *TCF/LEF* reporter plasmids and treated with JW55 or PRI-724. All samples stimulated with WNT3A.

(G) *Axin2* mRNA expression in mouse hyperplasia and tumor samples. Numbers as in Figure 4I.

(H) *Axin2* mRNA expression in mouse tumor samples. Numbers as in Figure S4Q.

(I) Immunofluorescence staining for nonP-β-catenin to quantify nuclear β-catenin in M130604 transfected with siCo, siWDR19, or siFUZ, treated with GSK503, and stimulated with WNT3A.

Scale bars, 25 μm. Data are represented as mean ± SEM (A and F–H) of 3 independent experiments (A and F), as mean ± SD (D), or as median ± interquartile range (box) and ± 100% range (whiskers) of 2 independent experiments (I). p values calculated with ANOVA and Fisher's LSD test (A and F–I), Spearman's r_S (D), or unpaired Student's *t*-test (G). See also Figure S6.

Figure 7. Primary cilium disassembly and WNT/β-catenin signaling promote melanoma growth

(A and B) Colony formation assay (A) to quantify clonogenicity (B) of A375 transfected with siCo, siWDR19, or siFUZ and treated with JW55 or PRI-724.

(C) Clonogenicity of RIH-1 infected with lenti-shCo, shWdr19, or shKif3a and treated with JW55 or PRI-724.

(D and E) Colony formation assay (D) to quantify clonogenicity (E) of M130604 transfected with siCo, siWDR19, or siFUZ and treated with GSK503, JW55, or PRI-724.

(F) Colony formation assay to quantify clonogenicity of M130604 transfected with empty vector or CTNNB1^{S33Y}-expression plasmid and treated with Chiron or GSK503.

Data are represented as mean ± SEM of 4 independent experiments. p values calculated with ANOVA and Fisher's LSD test. See also Figure S7.

Figure 8. Primary cilium deconstruction is sufficient to initiate metastatic melanoma

(A) Strategy used to infect RIM-3 cells with lenti-shCo or shWdr19, transplanted into Nude mice, and treated with vehicle or GSK503.

(B) Tumor growth curves of mice in (A). shCo + vehicle, n = 12; shCo + GSK503, n = 10; other groups, n = 5 mice.

(C) Weight of tumors in (B) at endpoint.

(D) *Axin2* mRNA expression in tumors from (B).

(E) Strategy used to infect RIH cells with lenti-shCo, shWdr19, shKif3a, empty vector, or CTNNB1^{S33Y} and transplant into Nude mice.

(F) Picture of shWdr19 mice in (E) at endpoint of shCo animals.

(G and H) Tumor growth curves of shWdr19 (G) and shKif3a (H) mice in (E). shCo, each n = 14; shWdr19#2, each n = 8; other groups, each n = 5 mice.

(I) FACS analyses to quantify GFP$^+$ td-tomato$^+$ RIH cells in lungs from mice in (G and H).

(J) Tumor growth curves of CTNNB1^{S33Y} mice in (E). Empty vector, each n = 5; CTNNB1^{S33Y}, each n = 8 mice.

(K) FACS analyses to quantify GFP$^+$ td-tomato$^+$ RIH cells in lungs from mice in (J).

(L) Western blots to quantify β-catenin intensities in second-generation tumors derived from RIH-1–EZH2^{Y646N} (Figure 1E), RIH-2–shWdr19#2 (G), or RIH-2–shWdr19#1 (H) tumors and treated with vehicle or JW55. n = 5 mice per group.

(M) Tumor growth curves of mice in (L).

Data are represented as mean ± SEM of 2 independent experiments (B–D and G–I) or one experiment (J–M). p values calculated with ANOVA and Fisher's LSD test (B–D and M), Kruskal-Wallis test with Dunn's multiple comparisons test (I), Mann-Whitney *U* test (K), or unpaired Student's *t*-test (L). See also Figure S8.

STAR METHODS

CONTACT FOR REAGENT AND RESOURCE SHARING

Further information and requests for resources and reagents should be directed to and will be fulfilled by the Lead Contact, Lukas Sommer (lukas.sommer@anatomy.uzh.ch).

EXPERIMENTAL MODEL AND SUBJECT DETAILS

Mice

3-month-old female Hsd:Athymic Nude-*Foxn1*$^{nu/nu}$ mice were purchased (Envigo). Mice carrying a Cre-inducible *Braf–lox-stop-lox-*(*LSL*)*–Braf*^{V600E}, *R26R-LSL-LacZ*, or *R26R-LSL-tdTomato* allele, a floxed *Pten* allele, or a *Tyr::CreER*^{T2} transgene were derived from The Jackson Laboratory. Mice carrying a floxed *Ezh2* allele (Hirabayashi et al., 2009), a Cre-inducible *ColA1-LSL-Ezh2*^{Y646N} allele (Béguelin et al., 2013), or a *Tyr::Nras*^{Q61K} transgene (Ackermann et al., 2005), and mice deficient for the *Cdkn2a* (*INK4a*) locus (Serrano et al., 1996) were kind gifts of Haruhiko Koseki (RIKEN Center for Integrative Medical Sciences, Japan), Kwok-Kin Wong (Dana-Farber Cancer Institute, USA), Friedrich Beermann (Swiss Federal Institute of Technology Lausanne, Switzerland), and Manuel Serrano (Centro Nacional de Investigaciones Oncologicas, Spain), respectively. These individual transgenic lines were crossed to achieve mouse genotypes indicated in (Figures 2A, 3A, S3A, and S4P). Genetic background of experimental animals was mixed. Mice were born with the expected ratio of Mendelian inheritance, and no changes in gender ratios were observed. Experimental mice were of both genders, and no apparent phenotypic differences between genders were observed. No statistical methods were used to predetermine sample size. For all experiments presented in this study, the sample size was large enough to measure the effect size. The experiments were not randomized and the investigators were not blinded to allocation during experiments and outcome assessment. The mouse colony was housed in a certified animal facility with a 12-hour light/dark cycle in a temperature-controlled room (22 ± 1 °C) with free access to water and food, in accordance with Swiss guidelines. All animal experiments were approved by the veterinary authorities of Canton of Zurich, Switzerland, and were performed in accordance with Swiss law and GlaxoSmithKline policy on the Care, Welfare, and Treatment of Animals.

Human Material

Primary human materials were provided by the Tumor Biopsy and the Live Cell Biobanks of the University Research Priority Program (URPP) "Translational Cancer Research" (Mitchell P. Levesque, University Hospital Zurich). Biobanking of surplus, human material from consenting melanoma patients was performed according to the Declaration of Helsinki on Human Rights, and was approved by the Institutional Review Board (IRB) of Zurich (EK.647/800). All research on surplus human material was conducted under the IRB approval KEK-Zh.Nr 2014-0425. To ensure patient confidentiality no informations on age, gender, and ethnicity were provided to the investigators of this study.

Cell Lines and Primary Cultures

The human cell lines A375 (#CRL-1619, ATCC), HEK-293T (#CRL-3216, ATCC) SK-MEL-28 (#HTB-72, ATCC), WM852 (#WM852-01-0001, Rockland), and WM983B (#WM983B-01-0001, Rockland) were purchased. Human melanoma cell lines 501Mel and 888Mel were described before (Rubinfeld et al., 1997). Human melanoma short-term cell cultures M990514, M010817, M050829, M070302, M080423, M130604, and M140130 were established and genotyped by the URPP Live Cell Biobank (University of Zurich). HEK-293T cells were grown in DMEM (#41965, Thermo Fisher Scientific) supplemented with 10% fetal bovine serum (FBS, #16140, Thermo Fisher Scientific). Melanoma cells were cultured in growth medium, which was RPMI 1640 (#42401, Thermo Fisher Scientific) supplemented with 10% FBS, 4 mM L-Glutamine (#25030, Thermo Fisher Scientific), Penicillin-Streptomycin (#15070, Thermo Fisher Scientific), and Fungizone Antimycotic (#15290, Thermo Fisher Scientific). Murine primary cells derived from a *Nras*^{Q61K};*Cdkn2a*(*INK4a*)$^{-/-}$ melanoma (RIM-3), a *Nras*^{Q61K};*Cdkn2a*(*INK4a*)$^{-/-}$;*Tyr::CreER*^{T2};*Ezh2*$^{lox/lox}$ melanoma (RIM-1), or *Nras*^{Q61K};*Cdkn2a*(*INK4a*)$^{-/-}$ hyperplasia (RIH-1, RIH-2) were cultured on plates coated with fibronectin (#F1141, Sigma-Aldrich) using melanocyte medium, which was DMEM/F-12 (#21041, Thermo Fisher Scientific) supplemented with 10% FBS, Penicillin-Streptomycin, and 200 nM 12-O-tetradecanoylphorbol 13-acetate (TPA, #P1585, Sigma-Aldrich). Prior to subjecting cells to functional *in vitro* assays, cells were grown for 48 hr in starvation medium, which was

growth medium supplemented with 1% FBS. All cells were cultured in CO_2 cell culture incubators (Binder) at 37 °C with 5% CO_2.

METHOD DETAILS

Mouse genotyping

Mouse biopsies were digested overnight at 55 °C using 150 µg/ml Proteinase K (#03115828001, Roche) in lysis buffer, which was 5 mM ethylenediaminetetraacetic acid (EDTA, #AM9261, Thermo Fisher Scientific), 200 mM sodium chloride (NaCl, #71380, Sigma-Aldrich), 0.2% sodium dodecylsulfate (SDS, #A2263, AppliChem), and 100 mM Tris hydrochloride (Tris-HCl, #A3452, AppliChem). Genomic DNA was precipitated with isopropanol (#1096341000, Merck Millipore) and resolved in water according to standard protocols followed by PCR using KAPA Taq ReadyMix with dye (#KK1024, Kapa Biosystems) and primers either recommended by The Jackson Laboratory or indicated in (Table S2). PCR products were segregated using agarose (#A8963, AppliChem) gel electrophoresis.

In vivo gene activation and deletion

To conditionally induce *Ezh2*^{Y646N}, *tdTomato*, and *Braf*^{V600E} expression, either *Tyr::CreER*^{T2};*R26R-LSL-tdTomato;ColA1-LSL-Ezh2*^{Y646N};(*Tyr::Nras*^{Q61K};*Cdkn2a*$^{-/-}$) or *Tyr::CreER*^{T2};*R26R-LSL-tdTomato;Braf-LSL-Braf*^{V600E};*ColA1-LSL-Ezh2*^{Y646N} mice were subjected to 5 consecutive daily intraperitoneal (IP) injections of 2 mg tamoxifen (TM, #T5648, Sigma-Aldrich) at an age of 4 weeks. To conditionally ablate *Ezh2* alleles, *Tyr::CreER*^{T2};*R26R-LSL-LacZ;Ezh2*$^{lox/lox}$;*Tyr::Nras*^{Q61K};*Cdkn2a*$^{-/-}$ animals were subjected to 5 consecutive daily IP injections of 2 mg TM at an age of 5 to 7 months, when skin melanomas had become macroscopically measureable (Ø ≥ 2 mm), as described before (Zingg et al., 2015). In *Tyr::CreER*^{T2};*Braf-LSL-Braf*^{V600E};*Pten*$^{lox/lox}$;*ColA1-LSL-Ezh2*^{Y646N} animals, *Pten* deletion and gene activation was achieved by topical administration of 80 µg 4-hydroxytamoxifen (4-OHT, #H7904, Sigma-Aldrich) onto 2 cm^2 of shaved back skin of 6-week-old mice. TM was diluted (10 mg/ml) in ethanol

(#20821.296, VWR Chemicals) and sunflower seed oil (#S5007, Sigma-Aldrich) (1:9), while 4-OHT was diluted (4 mg/ml) in dimethyl sulfoxide (DMSO, #D2650, Sigma-Aldrich) and ethanol (1:4).

Trunk skin depilation

To stimulate hair cycle progression in wild-type (WT) or *Ezh2*^{Y646N} mice, animals were anaesthetized with isoflurane (#430024079, Piramal Healthcare) and dorsal skin was depilated using wax strips (Veet). First depilation was performed at 2 months of age and serially repeated every 1.5 months for three times. Mice were sacrificed 14 days after the last depilation, when stimulated hair cycle anagen was peaking.

Quantification of skin melanomas and lymph node metastasis

After 4-OHT application, melanoma growth on *Braf*^{V600E};*Pten*$^{-/-}$;(*Ezh2*^{Y646N}) animals was monitored every second day. Mice were sacrificed, when tumors showed ulceration. After TM administration, mice with a melanoma-prone genotype, i.e. *Nras*^{Q61K};(*Ezh2*^{Y646N}), *Nras*^{Q61K};*Cdkn2a*$^{-/-}$;(*Ezh2*^{Y646N}), and *Braf*^{V600E};(*Ezh2*^{Y646N}), were monitored weekly for appearance of skin melanomas. Developing trunk skin lesions were considered as melanomas when reaching a diameter of 2 mm (Ø ≥ 2 mm). Animals were sacrificed at an endpoint defined by adverse clinical symptoms including large skin tumors (Ø > 10 mm), ulcerating tumors, weight loss (Δm > 15%), or hunched back. At day of sacrifice, a final skin melanoma count was established. To quantify lymph nodes affected by metastatic melanoma, accessory axillary, proper axillary, sciatic, and subiliac lymph nodes (total of eight) were subjected to histological analysis identifying tdTomato^{+} melanoma cells. When conditionally deleting *Ezh2* in *Nras*^{Q61K};*Cdkn2a*$^{-/-}$ mice bearing established skin melanoma, animals were monitored as described (Zingg et al., 2015) and sacrificed 4 weeks post TM administration.

Isolation of primary murine cells

Short-term cell cultures isolated from *Nras*^{Q61K};*Cdkn2a*$^{-/-}$ tumors (RIM-1, RIM-3) were previously characterized (Zingg et al., 2015). To isolate dermal hyperplasia cells (RIH-1, RIH-2) from *Tyr::CreER*^{T2};*R26R-LSL-tdTomato;Tyr::Nras*^{Q61K};*Cdkn2a*$^{-/-}$ mice, melanocytic cells were fluorescently labeled in 3-month-old mice via Cre-mediated *tdTomato* activation using TM. To isolate hyperplasia cells from *Tyr::CreER*^{T2};*R26R-LSL-tdTomato*;*Tyr::Nras*^{Q61K};(*ColA1-LSL-Ezh2*^{Y646N}) or *Tyr::CreER*^{T2};*R26R-LSL-tdTomato;Braf-LSL-Braf*^{V600E};(*ColA1-LSL-Ezh2*^{Y646N}) mice, *tdTomato* and transgenes were activated in melanocytic cells of 6-week-old animals. 4 weeks post recombination, dorsal trunk skin was dissected into small pieces and tissue was digested using 0.25 mg/ml Liberase DH Research Grade (#05401054001, Roche) in RPMI 1640 for 1 hr at 37 °C followed by a treatment with 0.2 mg/ml DNase I (#10104159001, Roche) for 15 min at 37 °C. Single cells were separated from remaining tissue using 40 µm Falcon Cell Strainers (#352340, Thermo Fisher Scientific) and resuspended in phosphate buffered saline (PBS, #10010, Thermo Fisher Scientific) containing 2 mM EDTA. Live tdTomato-traced cells were discriminated from dead cells using the LIVE/DEAD Fixable Near-IR Dead Cell Stain Kit (#L34975, Thermo Fisher Scientific) and isolated with a BD FACSAria III Cell Sorter (BD Biosciences) equipped with a 100 µm nozzle. Cells were collected into 1.5 ml Protein LoBind Tubes (#0030108116, Eppendorf) containing either 100% FBS for downstream live cell applications or Buffer RLT (#79216, Qiagen) with 1% 2-mercaptoethanol (#M3148, Sigma-Aldrich) for total RNA isolation.

Allografting of primary murine cells

Immunocompromised Nude recipient mice were subcutaneously (SC) engrafted with 100,000 RIH or 300,000 RIM cells suspended in RPMI 1640. When tumors became palpable, tumor size was measured every other day using a caliper. Mice were sacrificed when tumors reached a maximal volume of 1,500 mm^3. Tumor volume was calculated as follows: $V = 2/3 \times \pi \times ((a + b)/4)^3$, a (mm) was the length and b

(mm) was the width of the tumor. All treatments of mice were initialized when tumors reached about a volume of 100 mm^3. To block EZH2 activity *in vivo*, mice harboring RIM-3 tumors were subjected to daily IP injections of 150 mg/kg GSK503 EZH2 inhibitor (GlaxoSmithKline) until termination of the experiment. GSK503 was diluted (15 mg/ml) in 20% Captisol solution (#RC-0C7-100, Ligand Pharmaceuticals) and pH was adjusted to 5.3 using 1 M acetic acid (#320099, Sigma-Aldrich). *In vivo* efficacy of GSK503 has previously been evaluated (Béguelin et al., 2013; Zingg et al., 2015, 2017). To conditionally ablate *Ezh2*, mice harboring RIM-1 tumors were subjected to 5 consecutive daily IP injections of 2 mg TM as described previously (Zingg et al., 2015). To block canonical WNT/β-catenin signaling *in vivo*, mice harboring second-generation tumors originating from RIH cells were subjected to daily oral gavage administrations of 100 mg/kg JW55 tankyrase inhibitor (#406502, MedKoo Biosciences) until termination of the experiment. JW55 was diluted (20 mg/ml) in DMSO, ethanol, and tap water (3:3:4) and pH was adjusted to 5 using 1 M acetic acid. *In vivo* efficacy of JW55 was previously evaluated (Waaler et al., 2012).

FACS analysis of tumors and lungs from allografted mice

Upon sacrifice, tumors and lungs from Nude mice engrafted SC with RIH or RIM cells were dissociated using Liberase DH Research Grade and DNase I as described for $Nras^{Q61K}$;$Cdkn2a^{-/-}$ mouse skin digestion. Single cells were separated from remaining tissue using a 40 μm cell strainer and resuspended in PBS with 2 mM EDTA. Live cells were distinguished from dead cells using the LIVE/DEAD Fixable Near-IR Dead Cell Stain Kit. tdTomato and ZsGreen1 or GFP double-positive cells were quantified with a BD FACSCanto II Flow Cytometer (BD Biosciences) and FlowJo software (Tree Star).

Immunofluorescence on human and mouse tissue sections

3 µm sections of human paraffin-embedded nevus and melanoma biopsies were provided by the URPP Tumor Biopsy Biobank (University of Zurich). Mouse skin, tumor, and lymph node samples were fixed in 4% Roti-Histofix (#P087.3, Carl Roth) overnight at 4 °C, embedded in paraffin, and sliced into 5 µm sections. Sections were deparaffinized as described before (Zingg et al., 2015). Sections were subjected to an antigen-unmasking step in citrate buffer (#S2369, Dako) using a microwave histoprocessor (Milestone) for 10 min at 110 °C and blocked with 1% BSA (#A4503, Sigma-Aldrich) in PBS and 0.05% Triton X-100 (#T8787, Sigma-Aldrich) for 1 hr. Primary antibodies against acetylated tubulin (AcTub, #T7451, Sigma-Aldrich, 1:200), ARL13B (#17711-1-AP, Proteintech, 1:200), β-catenin (#sc-7199, Santa Cruz Biotechnology, 1:100), β-galactosidase (β-Gal, #ab9361, Abcam, 1:1,000), DCT (#ab74073, Abcam, 1:200), DCT (#sc-10451, Santa Cruz Biotechnology, 1:200), EZH2 (#5246, Cell Signaling Technology, 1:200), H3K27me3 (#9733, Cell Signaling Technology, 1:500), KI67 (#652402, BioLegend, 1:100), MART1 (#ab785, Abcam, 1:100), PAX3 (#38-1801, Thermo Fisher Scientific, 1:100), SOX10 (#sc-17342, Santa Cruz Biotechnology, 1:100), and tdTomato (#LS-C340696, LifeSpan BioSciences, 1:500) were applied in Antibody Diluent (#S0809, Dako) overnight at 4 °C. Slides were washed with PBS 3 times for 5 min. Primary antibodies were visualized using Alexa Fluor (AF)-488 anti-goat (#705-545-147, Jackson ImmunoResearch, 1:500), AF-488 anti-mouse IgG2b (#A-21141, Thermo Fisher Scientific, 1:500), AF-488 anti-rabbit (#711-545-152, Jackson ImmunoResearch, 1:500), AF-488 anti-rat (#711-545-153, Jackson ImmunoResearch, 1:500), Cy3 anti-goat (#705-165-147, Jackson ImmunoResearch, 1:500), Cy3 anti-rabbit (#711-165-152, Jackson ImmunoResearch, 1:500), Cy3 anti-rat (#711-165-153, Jackson ImmunoResearch, 1:500), AF-647 anti goat (#705-605-147, Jackson ImmunoResearch, 1:500), and AF-633 anti-mouse IgG1 (#A-21126, Thermo Fisher Scientific, 1:500) secondary antibodies in Antibody Diluent for 1 hr at room temperature. For visualization of β-Gal and SOX10, biotinylated anti-chicken (#AP194B, Merck Millipore, 1:500) and anti-goat (#705-065-003, Jackson ImmunoResearch, 1:500) secondary antibodies were combined with further signal amplification using horseradish peroxidase-streptavidin (#016-030-084, Jackson ImmunoResearch, 1:300) and the TSA Plus Cy3 Kit (#NEL744001KT, PerkinElmer, 1:50) according to manufacturers' protocols. Subsequently, nuclear DNA

was stained with Hoechst 33342 (#14533, Sigma-Aldrich) and slides were mounted with Fluorescent Mounting Medium (#S3023, Dako). For skin derived from WT mice, samples were fixed in 4% Roti-Histofix for 4 hr at 4 °C, immersed in 30% sucrose (#S0389, Sigma-Aldrich) overnight at 4 °C, and cryo-preserved in Tissue-Tek O.C.T. Compound (#4583, Sakura). 12 µm cryo-sections were post-fixed in 2% formaldehyde (#F8775, Sigma-Aldrich) for 5 min. Immunofluorescent stainings were done as described for paraffin sections, except, to preserve endogenous tdTomato signal, antigen retrieval was avoided. Sections were recorded using either a DMI 6000B microscope (Leica) or an Axio Scan.Z1 slide scanner (Zeiss).

Quantification of immunofluorescence on human and mouse tissue sections

To quantify recombined hair follicles in murine WT skin, at least 100 hair follicles per sample were counted manually. For each mouse dermal hyperplasia sample, at least 15 dermal interfollicular areas were quantified. For each murine melanoma as well as human nevus or melanoma sample, at least 10 fields were quantified. Therefore, DCT^+ cells; $tdTomato^+$ per $PAX3^+$ or DCT^+ cells; $KI67^+$ per $SOX10^+$ or $PAX3^+$ cells; ARL13B $(cilia)^+$ per $SOX10^+$, DCT^+, $tdTomato^+$, or $\beta\text{-}Gal^+$ cells; or AcTub $(cilia)^+$ per $MART1^+$ cells were identified and counted manually with ImageJ 1 software (Schneider et al., 2012). To measure nuclear H3K27me3 fluorescence intensity on murine melanoma sections, single fluorescence channels for H3K27me3, DCT or SOX10, and nuclear DNA were overlaid as separate layers in Photoshop CS5 software (Adobe). $SOX10^+$ or DCT^+ cells and DNA^+ nuclei were selected using the "Magic Wand Tool". SOX10 or DCT and nuclei-negative areas were then superimposed as "Darken" layers onto the H3K27me3 layer generating SOX10 or DCT and nuclei-specific H3K27me3 images. These images were quantified with CellProfiler software (Carpenter et al., 2006) using algorithms to "Identify Primary Objects" and to "Measure Object Intensity". To quantify nuclear EZH2 and β-catenin fluorescence intensities on human nevi and melanoma samples, single fluorescence channels for EZH2 or β-catenin,

MART1, and nuclear DNA were processed with Photoshop CS5 and CellProfiler software as described for H3K27me3.

Construction of CTNNB1^{S33Y} lentivector

Human *CTNNB1*^{S33Y} cDNA was PCR-amplified from a pcDNA3.1-FLAG-CTNNB1^{S33Y} plasmid (Valenta et al., 2011) by using High Fidelity PCR Master (#12140314001, Roche) and primers indicated in (Table S2) containing a BamHI or EcoRI restriction site. PCR product was segregated by agarose gel electrophoresis and purified with the QIAquick Gel Extraction Kit (#28704, Qiagen). PCR product and pMuLE-ENTR-CMV-L1-R5 vector (#62090, Addgene) were digested with FastDigest BamHI and EcoRI (#FD0054, #FD0274, Thermo Fisher Scientific), purified, and ligated using Anza T4 DNA Ligase Master Mix (#IVGN2108, Thermo Fisher Scientific). pMuLE-ENTR-CMV-CTNNB1^{S33Y}-L1-R5, pMuLE-ENTR-SV40-eGFP-L5-L2 (#62144, Addgene), and pLenti-X1-Puro-DEST (#17297, Addgene) vectors were subjected to L/R recombination using Gateway LR Clonase II Enzyme mix (#11791020, Thermo Fisher Scientific) as described previously (Albers et al., 2015). One Shot Stbl3 Chemically Competent *E. coli* (#C737303, Thermo Fisher Scientific) were transformed with pLenti-X1-Puro-CMV-CTNNB1^{S33Y}-SV40-eGFP vector, and plasmid was purified using QIAprep Spin Miniprep Kit (#27104, Qiagen) or NucleoBond Xtra Maxi Plus kit (#740416.10, Macherey-Nagel).

Lentivirus and retrovirus production

For lentivirus production, HEK-293T cells were co-transfected with 1 μg/ml of pLenti-eGFP, pLenti-CTNNB1^{S33Y}-eGFP, or plasmids expressing pGIPZ-non-silencing shRNA-TurboGFP (shCo, #RHS4346, Dharmacon), pGIPZ-shKif3a-TurboGFP (shKif3a#1/2, #RMM4431-20031-7419/8662, Dharmacon), or pGIPZ-shWdr19-TurboGFP (shWdr19#1/2, #VGM5520-20037-9129/7417, Dharmacon), in combination

with 0.25 µg/ml pMD2.G envelope-expressing plasmid (#12259, Addgene) and 0.55 µg/ml psPAX2 packaging plasmid (#12260, Addgene). For retrovirus production, HEK-293T cells were transfected with 1 µg/ml of pRetroX-IRES-ZsGreen1 (#632520, Clontech), pRetroX-EZH2^{WT}-IRES-ZsGreen1, or pRetroX-EZH2^{Y646N}-IRES-ZsGreen1, which have previously been validated (Béguelin et al., 2013; Zingg et al., 2015). Retroviral plasmids were combined with 1 µg/ml pCL-Ampho Retrovirus Packaging Vector (#NBP2-29541, Novus Biologicals). Efficient transfection was achieved with 2.5 M calcium chloride ($CaCl_2$, #C1016, Sigma-Aldrich) in HEPES (#H4034, Sigma-Aldrich) buffer according to standard protocols. Supernatant containing viral particles was collected daily starting 24 hr post transfection.

Stable gene silencing and expression

Murine RIH or RIM cells were exposed to virus supernatant (50% supernatant, 50% melanocyte medium) containing either lentiviral particles encapsulating shCo-TurboGFP, shKif3a#1/2-TurboGFP, shWdr19#1/2-TurboGFP, eGFP, or CTNNB1^{S33Y}-eGFP plasmids, or retroviral particles encapsulating ZsGreen1, EZH2^{WT}-IRES-ZsGreen1, or EZH2^{Y646N}-IRES-ZsGreen1 plasmids in combination with 10 µg/ml Polybrene (#sc-134220, Santa Cruz Biotechnology) for 48 hr. Cells infected with retrovirus were directly subjected to experiments. Cells infected with lentivirus were selected with 1 µg/ml puromycin (#A11138-02, Thermo Fisher Scientific) for 1 week before subjection to experiments.

Transient gene silencing and expression

For transient gene silencing, human cells were transfected with Stealth siRNA Negative Control Med GC Duplex #2 (siCo, #12935112, Thermo Fisher Scientific) or siRNAs targeting *FUZ* (siFUZ#1/2/3, #HSS12946-0/2/1, Thermo Fisher Scientific), *IFT81* (siIFT81#1/2/3, #HSS12077-6/7/5, Thermo Fisher Scientific), or *WDR19* (siWDR19#1/2/3, #HSS1-26738/26737/84043, Thermo Fisher Scientific).

Therefore, 25 nM siRNA was applied in combination with jetPRIME Transfection Reagent (#114-15, Polyplus Transfection) according to manufacturer's guidelines. For all functional assays, the most efficient siRNAs defined in (Figure S6A) were used. For transient gene expression, human cells were transfected with 1 µg/ml pLenti-eGFP, pLenti-CTNNB1^{S33Y}-eGFP, pRetroX-IRES-ZsGreen1, pRetroX-EZH2^{WT}-IRES-ZsGreen1, or pRetroX-EZH2^{Y646N}-IRES-ZsGreen1 plasmid in combination with jetPRIME Transfection Reagent according to manufacturer's guidelines. 24 hr after transfections, growth medium was replaced by starvation medium and cells were subjected to further assays after 48 hr of starvation.

In vitro inhibitor and growth factor applications

To pharmacologically inhibit EZH2, cells were treated with either vehicle (DMSO) or 1 µM GSK503 for 6 days in growth medium and for 48 hr in starvation medium before subjection to further assays. *In vitro* efficiency of GSK503 has been validated previously (Béguelin et al., 2013; Zingg et al., 2015). GSK503 was only replenished upon medium exchange or passaging of cells. To prevent phosphorylation of β-catenin via GSK-3 inhibition, cells were treated with either vehicle (DMSO) or 1 µM Chiron (CHIR99021, #1748-5, BioVision). To stimulate WNT/β-catenin or SHH/GLI signaling, cells were treated with vehicle (0.1% BSA in PBS), 100 ng/ml WNT3A (#5036-WN, R&D Systems), or 50 ng/ml SHH (#100-45, PeproTech) for 3 hr in starvation medium. To block canonical WNT/β-catenin signaling via tankyrase or CREB-binding protein inhibition, cells were threated with either vehicle (DMSO), 10 µM JW55 (#406502, MedKoo Biosciences), or 20 µM PRI-724 (#S8262, Selleckchem), respectively, for 48 hr in starvation medium before subjection to further assays. *In vitro* efficiencies of JW55 and PRI-724 have previously been validated (Emami et al., 2004; Waaler et al., 2012). JW55 and PRI-724 were replenished daily.

Luciferase reporter assay

To report WNT/β-catenin or SHH/GLI signaling, cells were transfected with 300 ng/ml plasmid mix (40:1 mixture of inducible firefly luciferase construct and constitutively expressing Renilla luciferase construct) from the TCF/LEF or the GLI Reporter Assay Kit (#336841, #CCS-018L and #CCS-6030L, Qiagen), respectively, using jetPRIME Transfection Reagent. Where applicable, cells were co-transfected with 300 ng/ml luciferase reporter construct mix and either 25 nM siRNA or 1 µg/ml gene expression plasmid. Cells were starved and, where applicable, treated with WNT3A, SHH, GSK503, Chiron, JW55, or PRI-724 as described above. Luciferase activity was measured with the Dual-Luciferase Reporter Assay System (#E1910, Promega) using a GloMax 96 Luminometer (#E5331, Promega). To standardize the transfection efficiency, luminescence levels of firefly luciferase were normalized to Renilla luciferase values.

Colony formation and cell proliferation assays

Cells transfected with siRNAs or plasmids were subjected to colony formation and cell proliferation assays 24 hr post transfection. To measure clonogenic potential, 500 cells per well were plated in 6-well plates in growth medium and, where applicable, subjected to GSK503, Chiron, JW55, or PRI-724 treatment. When colonies reached a considerable size (n > 50 cells), cells were fixed with 4% Roti-Histofix for 10 min and stained with Crystal violet solution (#HT90132, Sigma-Aldrich) for 30 min. Colonies (n > 50 cells) were counted manually using ImageJ 1 software. To measure cell proliferation, 1,000 cells per well were plated in 96-well plates in growth medium and, where applicable, subjected to GSK503 treatment. Cell density was determined with the Cell Proliferation Kit I (MTT) (#11465007001, Roche) according to the supplier's protocol starting 24 hr post seeding of the cells. Optical density was measured using a DTX 880 Multimode Detector (Beckman Coulter) at 595 nm.

Immunofluorescence on cells

Cells were grown on glass cover slips, fixed with 4% Roti-Histofix for 8 min, and blocked with 1% BSA in PBS and 0.05% Triton X-100 for 1 hr. Cells were subjected to immunofluorescent labeling using primary antibodies against AcTub (#T7451, Sigma-Aldrich, 1:200), ARL13B (#17711-1-AP, Proteintech, 1:500), non-phospho (nonP)-β-catenin (#8814, Cell Signaling Technology, 1:200), GFP (#GFP-1020, Aves Labs, 1:500), and PCNT (#ab28144, Abcam, 1:1,000) in blocking buffer overnight at 4 °C. Cells were washed with PBS 3 times for 5 min. Primary antibodies were visualized using AF-488 anti-mouse IgG2b (#A-21141, Thermo Fisher Scientific, 1:500), AF-488 anti-rabbit (#711-545-152, Jackson ImmunoResearch, 1:500), AF-546 anti-mouse (#A-11030, Thermo Fisher Scientific, 1:500), Cy3 anti-rabbit (#711-165-152, Jackson ImmunoResearch, 1:500), AF-633 anti-mouse (#A-21052, Thermo Fisher Scientific, 1:500), AF-633 anti-mouse IgG1 (#A-21126, Thermo Fisher Scientific, 1:500), and AF-647 anti-chicken (#103-605-155, Jackson ImmunoResearch, 1:500) secondary antibodies in blocking buffer for 1 hr at room temperature. Nuclei were stained with Hoechst 33342, and cells were recorded with a DMI 6000B microscope.

For each replica, at least 10 fields were quantified. Therefore, $AcTub^+$ or $ARL13B^+$ cells or $ARL13B^+$ per GFP^+ or $ZsGreen1^+$ cells were identified and counted manually with ImageJ 1 software. To measure nuclear β-catenin fluorescence intensity, single fluorescence channels for β-catenin and nuclear DNA were overlaid as separate layers in Photoshop CS5 software and DNA^+ nuclei were selected using the "Magic Wand Tool". Areas devoid of nuclei were superimposed as "Darken" layer onto the β-catenin layer. These nuclear β-catenin images were quantified with CellProfiler software using algorithms to "Identify Primary Objects" and to "Measure Object Intensity".

Protein isolation

For total protein isolation, cultured cells (500,000) and tumor biopsies (60 mg) were lysed in RIPA buffer (#89900, Thermo Fisher Scientific) containing Halt Protease and Phosphatase Inhibitor Cocktail (#78440,

Thermo Fisher Scientific). Homogenization of tumor biopsies was achieved by using a Polytron PT 2100 tissue disperser (Kinematica). Cell lysis was completed using a SONOPULS HD 2070 Ultrasonic Homogenizer (Bandelin). To separate cytoplasmic and nuclear protein fractions, 10 Mio cells were subjected to sequential cytoplasmic and nuclear lysis using NE-PER Nuclear and Cytoplasmic Extraction Reagents (#78833, Thermo Fisher Scientific) containing Halt Protease and Phosphatase Inhibitor Cocktail according to manufacturer's recommendations. Lysis of nuclear fraction was completed using a SONOPULS HD 2070 Ultrasonic Homogenizer. Protein concentrations were determined with the BCA Protein Assay Kit (#23227, Thermo Fisher Scientific) using a DTX 880 Multimode Detector at 562 nm.

Western blotting

Protein samples were denatured for 5 min at 95 °C with Laemmli Sample Buffer (#1610747, Bio-Rad) containing 10% 2-mercaptoethanol. 20 µg of protein per lane was loaded onto 4-20% Mini-PROTEAN TGX Gels (#4561094, #4561096, Bio Rad) and SDS-PAGE was carried out in Tris/Glycine/SDS Buffer (#1610732, Bio-Rad) for 1 hr with 120 V. Protein was transferred to nitrocellulose membranes using Nitrocellulose/Filter Paper Sandwiches (#1620215, Bio-Rad) with Tris/Glycine Buffer (#1610734, Bio-Rad) containing 20% methanol (#106009, Merck-Millipore) for 1 hr at 4 °C with 2 mA. Nitrocellulose membranes were blocked with Odyssey blocking buffer (#927–40000, LI-COR Biosciences) for 1 hr. Primary antibodies against β-actin (#A5316, Sigma-Aldrich, 1:10,000), total β-catenin (#sc-7199, Santa Cruz Biotechnology, 1:1,000), nonP-β-catenin (#8814, Cell Signaling Technology, 1:1,000), EZH2 (#5246, Cell Signaling Technology, 1:1,000), histone 3 (#3638, Cell Signaling Technology, 1:2,000), H3K27me2 (#9728, Cell Signaling Technology, 1:1,000), or H3K27me3 (#9733, Cell Signaling Technology, 1:2,000) were applied in Odyssey blocking buffer overnight at 4 °C. Membranes were washed with PBS containing 0.1% TWEEN 20 (#P1379, Sigma-Aldrich) (PBS-T) 3 times for 10 min. Primary antibodies were visualized using IRDye-800CW anti-mouse (#926-32212, LI-COR Biosciences, 1:10,000) and IRDye-680LT anti-rabbit (#926-68023, LI-COR Biosciences, 1:10,000) secondary

antibodies in Odyssey blocking buffer for 45 min at room temperature. To remove antibodies, nitrocellulose membranes were treated with NewBlot Nitro Stripping Buffer (#928-40030, LI-COR Biosciences) for 15 min. Prior to antibody re-exposure, membranes were washed with PBS-T 3 times for 10 min. Blots were scanned with an Odyssey imaging system (LI-COR Biosciences) and quantified with ImageJ 1 software. Quantified band intensities were normalized using either β-actin or histone 3 as housekeeping protein. Histone 3 was used as marker to survey accurate protein fractionation.

RNA isolation and reverse transcriptase reaction

Cultured cells (500,000) were lysed in Buffer RLT containing 1% 2-mercaptoethanol, while frozen tumor biopsies (40 mg) were homogenized in such buffer using a Polytron PT 2100 tissue disperser. Subsequent total RNA extraction and DNase treatment of samples was performed using the RNeasy Mini Kit (#74104, Qiagen) and the RNase-Free DNase Set (#79254, Qiagen) according to manufacturer's guidelines. Purified RNA was quantified using a NanoDrop ND-1000 Spectrophotometer (Thermo Fisher Scientific) and subjected to reverse transcriptase (RT) reaction using the Maxima First Strand cDNA Synthesis Kit (K1641, Thermo Fisher Scientific) followed by a RNase H (EN0202, Thermo Fisher Scientific) digestion step according to manufacturer's recommendations. At least 20,000 tdTomato-traced hyperplasia cells from *Nras*^{Q61K};(*Ezh2*^{Y646N}) or *Braf*^{V600E};(*Ezh2*^{Y646N}) mice were FACS-isolated into 1.5 ml Protein LoBind Tubes containing Buffer RLT with 1% 2-mercaptoethanol. Subsequent total RNA extraction and DNase treatment of samples was performed using the RNeasy Micro Kit (#74004, Qiagen) according to manufacturer's guidelines. Total RNA was subjected to Quantiscript RT reaction and REPLI-g SensiPhi DNA amplification using the REPLI-g WTA Single Cell Kit (#150063, Qiagen) according to manufacturer's recommendations.

Genomic DNA isolation from tumor biopsies

Frozen tumor biopsies (25 mg) were lysed and genomic DNA was purified with the QIAamp Fast DNA Tissue Kit (#51404, Qiagen) following manufacturer's guidelines.

Chromatin isolation and ChIP of human cells

Chromatin isolation and chromatin immunoprecipitation (ChIP) of human cultured cells was performed with the SimpleChIP Enzymatic Chromatin IP Kit (#9003, Cell Signaling Technology) according to manufacturer's guidelines. 10 Mio cultured cells were crosslinked on culture plates with 1% formaldehyde for 10 min and subjected to chromatin isolation. Isolated nuclei were digested with 5 µl micrococcal nuclease for 30 min at 37 °C and nuclei were lysed using a SONOPULS HD 2070 Ultrasonic Homogenizer. Chromatin digestion efficiency was verified by agarose gel electrophoresis and chromatin concentration was determined with a NanoDrop ND-1000 Spectrophotometer. The ChIP was performed with 20 µg chromatin and a primary antibody against H3K27me3 (#9733, Cell Signaling Technology, 1:100) or an IgG control antibody (#2729, Cell Signaling Technology, 1:100).

Chromatin isolation and ChIP of mouse tissue and cells

Frozen mouse tumors (100 mg) were chopped into small pieces, resuspended in PBS, and crosslinked with 1% formaldehyde for 10 min. Reaction was stopped with 100 mM glycine (#G8898, Sigma-Aldrich). Tissue suspensions were washed twice with PBS and homogenized with a Dounce tissue grinder set (Sigma-Aldrich) until single cell suspensions were obtained. The cell pellet was resuspended in buffer A, which was 100 mM Tris-HCl with 10 mM DL-Dithiothreitol (#43815, Sigma-Aldrich), and incubated for 15 min on ice followed by shaking for 15 min at 30 °C. Cells were centrifuged at 3,000 x g and resuspended in buffer B, which was 10 mM EDTA, 10 mM EGTA (#E3889, Sigma-Aldrich), 10 mM HEPES, and 0.25% Triton X-100, and incubated for 10 min on ice. Next, the cell pellet was resuspended

in buffer C, which was 10 mM EDTA, 0.5 mM EGTA, 10 mM HEPES, and 200 mM NaCl, and incubated for 5 min on ice. Chromatin was treated with 90 units Nuclease S7 (#10107921001, Roche) in 500 µl MNase buffer, which was 300 mM sucrose, 50 mM Tris-HCl, 30 mM potassium chloride (#P9333, Sigma-Aldrich), 7.5 mM NaCl, 4 mM $CaCl_2$, 0.125% Nonidet P 40 Substitute (NP-40, #74385, Sigma-Aldrich), and 0.25% sodium deoxycholate (#30970, Sigma-Aldrich), supplemented with Halt Protease and Phosphatase Inhibitor Cocktail, for 1 hr at 37 °C. Nuclease S7 digestion was stopped with 5 mM EDTA and 0.01% SDS. Samples were sonicated for 5 cycles using a Bioruptor sonication device (Diagenode). Chromatin digestion quality and concentration was verified by agarose gel electrophoresis.

At least 50,000 tdTomato-traced hyperplasia cells from *Nras*^{Q61K};(*Ezh2*^{Y646N}) or *Braf*^{V600E};(*Ezh2*^{Y646N}) mice were FACS-isolated into 1.5 ml Protein LoBind Tubes containing 100% FBS. Cells were pelleted at 3,000 x g, resuspended in 10% FBS in PBS, and crosslinked with 1% formaldehyde for 10 min. Reaction was stopped with 100 mM glycine for 10 min. Cells were washed once with 10% FBS in PBS, and chromatin preparation was done as described previously (Gilfillan et al., 2012). Briefly, chromatin was treated with 0.1 units Nuclease S7 in 100 µl MNase digestion buffer, which was 50 mM Tris-HCl, 1 mM $CaCl_2$, and 0.2% Triton X-100, supplemented with Halt Protease and Phosphatase Inhibitor Cocktail, for 30 min at 37 °C. Nuclease S7 digestion was stopped with 11 mM Tris-HCl, 5.5 mM EDTA, and 0.1% SDS. Samples were sonicated for 5 cycles using a Bioruptor sonication device.

The ChIP was performed with 20 µg chromatin diluted in ChIP buffer, which was 16.7 mM Tris-HCl, 167 mM NaCl, 1.2 mM EDTA, 0.01 % SDS, and 1.1 % Triton X-100. Chromatin was pre-cleared with Protein A-Sepharose CL-4B (#17-0780-01, GE Healthcare) on rotation for 2 hr at 4 °C. Supernatant was transferred to a clean 1.5 ml tube and incubated with primary antibody against H3K27me3 (#39155, Active Motif, 1:100) on rotation overnight at 4 °C. Immunoprecipitation was done with Dynabeads Protein A (#10002D, Thermo Fisher Scientific) with rotation for 4 hr at 4 °C. Beads were immobilized on a magnetic rack (#Z5342, Promega) and washed for 5 min twice with wash buffer 1, which was 16.7 mM Tris-HCl, 0.167 M NaCl, 0.1% SDS, and 1% Triton X-100; once with wash buffer 2, which was 16.7 mM

Tris-HCl, 0.5 M NaCl, 0.1 % SDS, and 1% Triton X-100; and twice with wash buffer 3, which was 0.25 M lithium chloride (#L4408, Sigma-Aldrich), 0.5% sodium deoxycholate, 10 mM Tris-HCl, 1 mM EDTA, and 0.5% NP-40. Chromatin was eluted from the beads with 300 µl of 1% SDS and 100 mM sodium bicarbonate (#S6297, Sigma-Aldrich) for 30 min at 37 °C. Beads were immobilized on a magnetic rack and supernatant was transferred to a clean 1.5 ml tube. For reverse-crosslinking, 50 mM Tris-HCl, 250 mM NaCl, and 12.5 mM EDTA were added and chromatin was incubated with 21.2 mg/ml Proteinase K for 1 hr at 50 °C, then overnight at 65 °C. DNA was purified with 300 µl Phenol-Chloroform-Isoamyl Alcohol (#P3803, Sigma-Aldrich). Water phase was collected in a clean 1.5 mL tube containing 30 µl of 3 M sodium acetate (#W302406, Sigma-Aldrich) and 1 µl of glycogen (#G0885, Sigma-Aldrich). DNA was precipitated with ethanol and resolved in water.

Quantitative real-time PCR

Quantitative real-time PCR (qPCR) was performed with LightCycler 480 Multiwell Plates (#04729692001, Roche) and a LightCycler 480 System (Roche). For cDNA and genomic DNA, qPCR was done with LightCycler 480 SYBR Green I Master (#4707516001, Roche). Primers were designed with Primer-BLAST (Ye et al., 2012) and are indicated in (Table S2). Where indicated, a Custom RT^2 PCR Array (#330171, Qiagen) spotted with primers for human primary cilium genes and *GAPDH* was used. Relative quantified cDNA was normalized using either mouse *Usf1*, human *USF1,* or, for primary cilium PCR plates, *GAPDH* as housekeeping transcript. Relative quantified genomic DNA was normalized using murine *Rpl30* Intron 2 (#7015P, Cell Signaling Technology) as housekeeping sequence. For DNA derived from ChIPs, qPCR was done with KAPA SYBR Fast qPCR Kit Master Mix (#KR0389, KAPA Biosystems). ChIP Primers were specified to amplify genomic DNA from a region flanking the transcriptional start site (TSS) –500 bp to +100 bp devoid of local CpG islands defined by The UCSC Genome Browser (Kent et al., 2002) and CpG island prediction (Li and Dahiya, 2002). Primers were designed with Primer-BLAST and are indicated in (Table S2). Relative enrichment was normalized to

chromatin inputs and to mouse intergenic region 1 (Interg1), mouse *Rpl30* Intron 2, or human *RPL30* Exon 3 (#7014P, Cell Signaling Technology) genomic DNA negative control sequences.

RNA-sequencing

Total RNA was purified as described above for *Nras*^{Q61K};(*Ezh2*^{Y646N}) hyperplasia cells. Total RNA quantity and quality was determined using the Qubit 4 Quantitation Starter Kit (#Q33227, Thermo Fisher Scientific) and a 4200 TapeStation System (#G2991AA, Agilent). Illumina sequencing libraries were prepared with the SMARTer Stranded Total RNA-Seq Kit - Pico Input Mammalian (#635005, Clontech) including ribosomal cDNA cleavage following manufacturer's recommendations. Quantity and quality of the enriched libraries were validated using the Qubit 4 Quantitation Starter Kit and a 4200 TapeStation System aiming for an average fragment size of approximately 360 bp. The libraries were normalized to a 10 nM concentration in 10 mM Tris-HCl and 0.1% TWEEN 20. Clusters were generated with 10 pM of pooled normalized libraries using the HiSeq 3000/4000 SR Cluster Kit (#GD-410-1001, Illumina) and a cBot 2 System (#SY-312-2001, Illumina). Sequencing was performed using the HiSeq 3000/4000 SBS Kit (#FC-410-1001, Illumina) on a HiSeq 4000 Sequencing System (#SY-401-4001, Illumina) at 125 bp single-end reads.

RNA-sequencing analyses

Raw reads were quality-checked using FastQC (Babraham Bioinformatics) and sequencing adapters were removed with Trimmomatic (Bolger et al., 2014). At least 20-base-long reads with an overall average Phred quality score greater than 10 were aligned to the reference genome of *M. musculus* (GRCm38/mm10) using STAR 2.5.1b (Dobin et al., 2013) with default settings for single-end reads. Distribution of the reads across genomic isoform expression and differentially expressed genes were

quantified with Bioconductor 3.0 software using the R packages GenomicRanges (Lawrence et al., 2013) and edgeR (Robinson et al., 2010), respectively. Genes were considered differentially expressed when displaying at least 10 counts in at least half of the samples of one group, FDR < 0.005, p < 0.01, and Log2 FC > 0.7 / < –0.7. PANTHER gene ontology (GO)-slim biological processes and cellular component analyses were performed using Overrepresentation Test and Fisher's Exact test with FDR multiple test correction (Mi et al., 2013).

ChIP-sequencing analyses

The published genomic H3K27me3 ChIP-seq profiles on malignant melanoma cell cultures GSE60666 (Verfaillie et al., 2015) were analyzed for H3K27me3 peak enrichment in the TSS of SYSCILIA genes (van Dam et al., 2013) versus random genes. Heatmaps and enrichment profiles were plotted ± 5 Kb from TSS using deepTools2 with plotHeatmap and plotProfile functions (Ramírez et al., 2016). Genome browser track snapshots were generated with Integrative Genomic Viewer (Robinson et al., 2011).

Microarray and TCGA analyses

The microarray gene expression analysis of GSE63165 has been described previously (Zingg et al., 2015). PANTHER GO cellular component complete analysis was performed using Overrepresentation Test and Bonferroni correction (Mi et al., 2013). The published gene expression datasets on benign nevus and malignant melanoma samples GSE4587 (Smith et al., 2005), GSE3189 (Talantov et al., 2005), GSE12391 (Scatolini et al., 2010), and GSE46517 (Kabbarah et al., 2010) were analyzed for expression of *EZH2* and selected cilia genes by normalizing individual values to the mean of nevus samples within each dataset. The Cancer Genome Atlas (TCGA)'s normalized RSEM gene expression, GISTIC2 copy number, and oncotated mutation files for skin cutaneous melanoma (SKCM) (TCGA Network, 2015) were downloaded

from the Broad Institute's GDAC Firehose (https://gdac.broadinstitute.org). All TCGA analyses were performed in R.

QUANTIFICATION AND STATISTICAL ANALYSIS

Statistical analyses are described in each figure legend and were performed using GraphPad Prism 7 or R. For comparison of two groups, p values were calculated with a two-sided unpaired Student's *t*-test. For comparison of more than two groups, p values were calculated using analysis of variance (ANOVA) with Geisser-Greenhouse correction and Fisher's least significant difference (LSD) test. For comparing FACS analyses, p values were calculated with a nonparametric two-sided Mann-Whitney *U* test or a nonparametric Kruskal-Wallis test with Geisser-Greenhouse correction and Dunn's multiple comparisons test. For comparison of Kaplan-Meier curves, p values were calculated with the log-rank (Mantel-Cox) test. Significance of correlations was calculated by using Spearman's rank correlation coefficient (r_S). For all statistical analyses, the expected variance was similar between the groups that were compared, and significance was accepted at the 95% confidence level (*$p < 0.05$, **$p < 0.01$, ***$p < 0.001$, ****$p < 0.0001$).

DATA AND SOFTWARE AVAILABILITY

The accession number for the data reported in this paper is GSE112677 and can be accessed via the following link https://www.ncbi.nlm.nih.gov/geo/query/acc.cgi?acc=GSE112677

KEY RESOURCES TABLE

REAGENT or RESOURCE	SOURCE	IDENTIFIER
Antibodies		
Mouse IgG2b Monoclonal Anti-Acetylated Tubulin Antibody	Sigma-Aldrich	Cat# T7451; RRID: AB_609894
Mouse IgG2a Monoclonal Anti-β-Actin Antibody	Sigma-Aldrich	Cat# A5316; RRID: AB_476743
Rabbit Polyclonal Anti-ARL13B Antibody	Proteintech	Cat# 17711-1-AP; RRID: AB_2060867
Rabbit Polyclonal Anti-β-Catenin Antibody	Santa Cruz Biotechnology	Cat# sc-7199; RRID: AB_634603
Rabbit Monoclonal Anti-Non-Phospho β-Catenin Antibody	Cell Signaling Technology	Cat# 8814; RRID: AB_11127203
Chicken Polyclonal Anti-β-Galactosidase Antibody	Abcam	Cat# ab9361; RRID: AB_307210
Rabbit Polyclonal Anti-DCT Antibody	Abcam	Cat# ab74073; RRID: AB_1524517
Goat Polyclonal Anti-DCT Antibody	Santa Cruz Biotechnology	Cat# sc-10451; RRID: AB_793582
Rabbit Monoclonal Anti-EZH2 Antibody	Cell Signaling Technology	Cat# 5246; RRID: AB_10694683
Chicken Polyclonal Anti-GFP Antibody	Aves Labs	Cat# GFP-1020; RRID: AB_10000240
Rabbit Monoclonal Anti-H3K27me2 Antibody	Cell Signaling Technology	Cat# 9728; RRID: AB_1281337
Rabbit Monoclonal Anti-H3K27me3 Antibody	Cell Signaling Technology	Cat# 9733; RRID: AB_2616029
Rabbit Polyclonal Anti-H3K27me3 Antibody	Active Motif	Cat# 39155; RRID: AB_2561020
Mouse IgG1 Monoclonal Anti-Histone 3 Antibody	Cell Signaling Technology	Cat# 3638; RRID: AB_1642229
Rat IgG2a Monoclonal Anti-KI67 Antibody	BioLegend	Cat# 652402; RRID: AB_11204254
Mouse IgG1 Monoclonal Anti-MART1 Antibody	Abcam	Cat# ab785; RRID: AB_306135
Rabbit Polyclonal Anti-PAX3 Antibody	Thermo Fisher Scientific	Cat# 38-1801; RRID: AB_2533359
Mouse IgG1 Monoclonal Anti-PCNT Antibody	Abcam	Cat# ab28144; RRID: AB_2160664
Goat Polyclonal Anti-SOX10 Antibody	Santa Cruz Biotechnology	Cat# sc-17342; RRID: AB_2195374
Goat Polyclonal Anti-tdTomato Antibody	LifeSpan BioSciences	Cat# LS-C340696
Rabbit IgG Control Antibody	Cell Signaling Technology	Cat# 2729; RRID: AB_1031062
Donkey Anti-Goat IgG (H+L) Secondary Antibody, Alexa Fluor 488	Jackson ImmunoResearch	Cat# 705-545-147; RRID: AB_2336933
Goat Anti-Mouse IgG2b Secondary Antibody, Alexa Fluor 488	Thermo Fisher Scientific	Cat# A-21141; RRID: AB_2535778
Donkey Anti-Rabbit IgG (H+L) Secondary Antibody, Alexa Fluor 488	Jackson ImmunoResearch	Cat# 711-545-152; RRID: AB_2313584
Donkey Anti-Rat IgG (H+L) Secondary Antibody, Alexa Fluor 488	Jackson ImmunoResearch	Cat# 712-545-153; RRID: AB_2340684
Goat anti-Mouse IgG (H+L) Secondary Antibody, Alexa Fluor 546	Thermo Fisher Scientific	Cat# A-11030; RRID: AB_2534089
Donkey Anti-Goat IgG (H+L) Secondary Antibody, Cy3	Jackson ImmunoResearch	Cat# 705-165-147; RRID: AB_2307351
Donkey Anti-Rabbit IgG (H+L) Secondary Antibody, Cy3	Jackson ImmunoResearch	Cat# 711-165-152; RRID: AB_2307443
Donkey Anti-Rat IgG (H+L) Secondary Antibody, Cy3	Jackson ImmunoResearch	Cat# 712-165-153; RRID: AB_2340667
Goat Anti-Mouse IgG (H+L) Secondary Antibody, Alexa Fluor 633	Thermo Fisher Scientific	Cat# A-21052; RRID: AB_2535719
Goat Anti-Mouse IgG1 Secondary Antibody, Alexa Fluor 633	Thermo Fisher Scientific	Cat# A-21126; RRID: AB_2535768
Goat Anti-Chicken IgY (H+L) Secondary Antibody, Alexa Fluor 647	Jackson ImmunoResearch	Cat# 103-605-155; RRID: AB_2337392
Donkey Anti-Goat IgG (H+L) Secondary Antibody, Alexa Fluor 647	Jackson ImmunoResearch	Cat# 705-605-147; RRID: AB_2340437
Donkey Anti-Chicken IgY (H+L) Secondary Antibody, Biotin	Merck Millipore	Cat# AP194B; RRID: AB_92675

Donkey Anti-Goat IgG (H+L) Secondary Antibody, Biotin	Jackson ImmunoResearch	Cat# 705-065-003; RRID: AB_2340396
Donkey Anti-Mouse IgG (H+L) Secondary Antibody, IRDye-800CW	LI-COR Biosciences	Cat# 926-32212; RRID: AB_621847
Donkey Anti-Rabbit IgG (H+L) Secondary Antibody, IRDye-680LT	LI-COR Biosciences	Cat# 926-68023; RRID: AB_10706167
Bacterial and Virus Strains		
One Shot Stbl3 Chemically Competent *E. coli*	Thermo Fisher Scientific	Cat# C737303
Lentiviral-shCo-TurboGFP	This paper	N/A
Lentiviral-shWdr19#1-TurboGFP	This paper	N/A
Lentiviral-shWdr19#2-TurboGFP	This paper	N/A
Lentiviral-shKif3a#1-TurboGFP	This paper	N/A
Lentiviral-shKif3a#2-TurboGFP	This paper	N/A
Lentiviral-eGFP	This paper	N/A
Lentiviral-CTNNB1^{S33Y}-eGFP	This paper	N/A
Retroviral-ZsGreen1	This paper	N/A
Retroviral-EZH2^{WT}-IRES-ZsGreen1	This paper	N/A
Retroviral-EZH2^{Y646N}-IRES-ZsGreen1	This paper	N/A
Biological Samples		
Human: Benign nevus paraffin sections	URPP Tumor Biopsy Biobank, UZH	N/A
Human: Malignant melanoma paraffin sections	URPP Tumor Biopsy Biobank, UZH	N/A
Human: Melanoma short-term cell cultures	URPP Live Tumor Cell Biobank, UZH	N/A
Mouse: *Nras*^{Q61K};*Cdkn2a*$^{-/-}$, *Nras*^{Q61K};*Cdkn2a*$^{-/-}$;*Ezh2*^{Y646N} , *Nras*^{Q61K};*Cdkn2a*$^{-/-}$;*Ezh2*$^{-/-}$ tumors	This paper	N/A
Mouse: *Braf*^{V600E};*Pten*$^{-/-}$, *Braf*^{V600E};*Pten*$^{-/-}$;*Ezh2*^{Y646N} tumors	This paper	N/A
Mouse: Primary *Nras*^{Q61K};*Cdkn2a*$^{-/-}$ tdTomato^{+} dermal hyperplasia cells (RIH-1)	This paper	N/A
Mouse: Primary *Nras*^{Q61K};*Cdkn2a*$^{-/-}$ tdTomato^{+} dermal hyperplasia cells (RIH-2)	This paper	N/A
Mouse: Primary *Nras*^{Q61K};*Cdkn2a*$^{-/-}$;*Tyr::CreER*^{T2};*Ezh2*$^{lox/lox}$ melanoma cells (RIM-1)	(Zingg et al., 2015)	N/A
Mouse: Primary *Nras*^{Q61K};*Cdkn2a*$^{-/-}$ melanoma cells (RIM-3)	(Zingg et al., 2015)	N/A
Chemicals, Peptides, and Recombinant Proteins		
Acetic acid, 99.7%	Sigma-Aldrich	Cat# 320099; CAS# 64-19-7
Agarose	AppliChem	Cat# A8963; CAS# 9012-36-6
Antibody Diluent	Dako	Cat# S0809
Bovine Serum Albumin (BSA)	Sigma-Aldrich	Cat# A4503; CAS# 9048-46-8
Calcium chloride	Sigma-Aldrich	Cat# C1016; CAS# 10043-52-4
Captisol	Ligand Pharmaceuticals	Cat# RC-0C7-100
Chiron (CHIR99021), GSK-3 inhibitor	BioVision	Cat# 1748-5; CAS# 252917-06-9
Crystal violet solution	Sigma-Aldrich	Cat# HT90132; CAS# 548-62-9
Dimethyl sulfoxide (DMSO)	Sigma-Aldrich	Cat# D2650; CAS# 67-68-5
DL-Dithiothreitol	Sigma-Aldrich	Cat# 43815; CAS# 3483-12-3
DNase I	Roche	Cat# 10104159001; CAS# 9003-98-9
Dynabeads Protein A	Thermo Fisher Scientific	Cat# 10002D
Ethanol absolut	VWR Chemicals	Cat# 20821.296; CAS# 64-17-5
Ethylenediaminetetraacetic acid (EDTA), 0.5 M	Thermo Fisher Scientific	Cat# AM9261; CAS# 60-00-4
EGTA	Sigma-Aldrich	Cat# E3889; CAS# 67-42-5
Falcon Cell Strainers, 40 µm	Thermo Fisher Scientific	Cat# 352340
Fetal Bovine Serum (FBS)	Thermo Fisher Scientific	Cat# 16140
Fibronectin	Sigma-Aldrich	Cat# F1141
Fluorescent Mounting Medium	Dako	Cat# S3023
Formaldehyde Solution, 37%	Sigma-Aldrich	Cat# F8775; CAS# 50-00-0
Fungizone Antimycotic	Thermo Fisher Scientific	Cat# 15290
Glycine	Sigma-Aldrich	Cat# G8898; CAS# 56-40-6
Glycogen	Sigma-Aldrich	Cat# G0885; CAS# 9005-79-2

L-Glutamine	Thermo Fisher Scientific	Cat# 25030
GSK503, EZH2 inhibitor	GlaxoSmithKline	CAS# 1346572-63-1
Halt Protease and Phosphatase Inhibitor Cocktail	Thermo Fisher Scientific	Cat# 78440
HEPES	Sigma-Aldrich	Cat# H4034; CAS# 7365-45-9
Hoechst 33342	Sigma-Aldrich	Cat# 14533; CAS# 23491-52-3
Horseradish Peroxidase-Streptavidin	Jackson ImmunoResearch	Cat# 016-030-084
4-Hydroxytamoxifen (4-OHT)	Sigma-Aldrich	Cat# H7904; CAS# 68047-06-3
Isoflurane	Piramal Healthcare	Cat# 430024079
Isopropanol	Merck Millipore	Cat# 1096341000; CAS# 67-63-0
JW55, Tankyrase inhibitor	MedKoo Biosciences	Cat# 406502; CAS# 664993-53-7
Laemmli Sample Buffer, 4X	Bio-Rad	Cat# 1610747
Liberase, DH Research Grade	Roche	Cat# 05401054001
LightCycler 480 Multiwell Plate 96, white	Roche	Cat# 04729692001
Lithium chloride	Sigma-Aldrich	Cat# L4408; CAS# 7447-41-8
Medium, DMEM	Thermo Fisher Scientific	Cat# 41965
Medium, DMEM/F-12	Thermo Fisher Scientific	Cat# 21041
Medium, RPMI 1640	Thermo Fisher Scientific	Cat# 42401
2-Mercaptoethanol	Sigma-Aldrich	Cat# M3148; CAS# 60-24-2
Methanol	Merck Millipore	Cat# 106009; CAS# 67-56-1
4-20% Mini-PROTEAN TGX Gels	Bio-Rad	Cat# 4561094, 4561096
NewBlot Nitro Stripping Buffer, 5X	LI-COR Biosciences	Cat# 928-40030
Nitrocellulose/Filter Paper Sandwiches	Bio-Rad	Cat# 1620215
Nonidet P 40 Substitute	Sigma-Aldrich	Cat# 74385; CAS# 9016-45-9
Nuclease S7	Roche	Cat# 10107921001; CAS# 9013-53-0
Odyssey Blocking Buffer	LI-COR Biosciences	Cat# 927-40000
Penicillin-Streptomycin	Thermo Fisher Scientific	Cat# 15070
Phenol-Chloroform-Isoamyl Alcohol	Sigma-Aldrich	Cat# P3803
Phosphate Buffered Saline (PBS), pH 7.4	Thermo Fisher Scientific	Cat# 10010
Polybrene	Santa Cruz Biotechnology	Cat# sc-134220
Potassium chloride	Sigma-Aldrich	Cat# P9333; CAS# 7447-40-7
PRI-724, Canonical WNT signaling inhibitor	Selleckchem	Cat# S8262; CAS# 847591-62-2
Protein A-Sepharose CL-4B	GE Healthcare	Cat# 17-0780-01
Protein LoBind Tubes	Eppendorf	Cat# 0030108116
Proteinase K, recombinant PCR grade	Roche	Cat# 03115828001
Puromycin	Thermo Fisher Scientific	Cat# A11138-02
RIPA Buffer	Thermo Fisher Scientific	Cat# 89900
RLT Buffer	Qiagen	Cat# 79216
RNase H	Thermo Fisher Scientific	Cat# EN0202
Roti-Histofix, 4%	Carl Roth	Cat# P087.3
SHH, Recombinant human protein	PeproTech	Cat# 100-45
Sodium acetate, anhydrous	Sigma-Aldrich	Cat# W302406; CAS# 127-09-3
Sodium bicarbonate	Sigma-Aldrich	Cat# S6297; CAS# 144-55-8
Sodium chloride	Sigma-Aldrich	Cat# 71380; CAS# 7647-14-5
Sodium deoxycholate	Sigma-Aldrich	Cat# 30970; CAS# 302-95-4
Sodium dodecylsulfate	AppliChem	Cat# A2263; CAS# 151-21-3
Sucrose	Sigma-Aldrich	Cat# S0389; CAS# 57-50-1
Sunflower seed oil	Sigma-Aldrich	Cat# S5007; CAS# 8001-21-6
Tamoxifen (TM)	Sigma-Aldrich	Cat# T5648; CAS# 10540-29-1
Target Retrieval Solution, Citrate pH 6	Dako	Cat# S2369
Tetradecanoylphorbol 13-acetate (TPA)	Sigma-Aldrich	Cat# P1585; CAS# 16561-29-8
Tissue-Tek O.C.T. Compound	Sakura	Cat# 4583
Tris Hydrochloride	AppliChem	Cat# A3452; CAS# 1185-53-1
Tris/Glycine Buffer, 10X	Bio-Rad	Cat# 1610734
Tris/Glycine/SDS Buffer, 10X	Bio-Rad	Cat# 1610732
Triton X-100	Sigma-Aldrich	Cat# T8787; CAS# 9002-93-1
Trypsin-EDTA, 0.25%	Thermo Fisher Scientific	Cat# 25200
TWEEN 20	Sigma-Aldrich	Cat# P1379; CAS# 9005-64-5

Wax strips	Veet	N/A
WNT3A, Recombinant human protein	R&D Systems	Cat# 5036-WN
Critical Commercial Assays		
Anza T4 DNA Ligase Master Mix	Thermo Fisher Scientific	Cat# IVGN2108
BCA Protein Assay Kit	Thermo Fisher Scientific	Cat# 23227
Cell Proliferation Kit I (MTT)	Roche	Cat# 11465007001
Cignal Reporter Assay Kit, *GLI1*	Qiagen	Cat# 336841, CCS-6030L
Cignal Reporter Assay Kit, *TCF/LEF*	Qiagen	Cat# 336841, CCS-018L
Dual-Luciferase Reporter Assay System	Promega	Cat# E1910
FastDigest BamHI	Thermo Fisher Scientific	Cat# FD0054
FastDigest EcoRI	Thermo Fisher Scientific	Cat# FD0274
High Fidelity PCR Master	Roche	Cat# 12140314001
HiSeq 3000/4000 SBS Kit	Illumina	Cat# FC-410-1001
HiSeq 3000/4000 SR Cluster Kit	Illumina	Cat# GD-410-1001
Gateway LR Clonase II Enzyme mix	Thermo Fisher Scientific	Cat# 11791020
jetPRIME Transfection Reagent	Polyplus Transfection	Cat# 114-15
KAPA SYBR Fast qPCR Kit Master Mix	Kapa Biosystems	Cat# KR0389
KAPA Taq ReadyMix With Dye	Kapa Biosystems	Cat# KK1024
LightCycler 480 SYBR Green I Master	Roche	Cat# 4707516001
LIVE/DEAD Fixable Near-IR Dead Cell Stain Kit	Thermo Fisher Scientific	Cat# L34975
Maxima First Strand cDNA Synthesis Kit	Thermo Fisher Scientific	Cat# K1641
NE-PER Nuclear and Cytoplasmic Extraction Reagents	Thermo Fisher Scientific	Cat# 78833
NucleoBond Xtra Maxi Plus kit	Macherey-Nagel	Cat# 740416.10
QIAamp Fast DNA Tissue Kit	Qiagen	Cat# 51404
QIAprep Spin Miniprep Kit	Qiagen	Cat# 27104
QIAquick Gel Extraction Kit	Qiagen	Cat# 28704
Qubit 4 Quantitation Starter Kit	Thermo Fisher Scientific	Cat# Q33227
REPLI-g WTA Single Cell Kit	Qiagen	Cat# 150063
RNase-Free DNase Set	Qiagen	Cat# 79254
RNeasy Micro Kit	Qiagen	Cat# 74004
RNeasy Mini Kit	Qiagen	Cat# 74104
SimpleChIP Enzymatic Chromatin IP Kit	Cell Signaling Technology	Cat# 9003
SMARTer Stranded Total RNA-Seq Kit - Pico Input Mammalian	Clontech	Cat# 635005
TSA Plus Cy3 Kit	PerkinElmer	Cat# NEL744001KT
Deposited Data		
Human: Microarray data	(Talantov et al., 2005)	GEO: GSE3189
Human: Microarray data	(Smith et al., 2005)	GEO: GSE4587
Human: Microarray data	(Scatolini et al., 2010)	GEO: GSE12391
Human: Microarray data	(Kabbarah et al., 2010)	GEO: GSE46517
Human: Microarray data	(Zingg et al., 2015)	GEO: GSE63165
Human: TCGA-SKCM, normalized RSEM gene expression, GISTIC2 copy number, and oncotated mutation files	(TCGA Network, 2015), Broad Institute, GDAC Firehose	https://gdac.broadinstitute.org
Human: ChIP-sequencing data	(Verfaillie et al., 2015)	GEO: GSE60666
Mouse: RNA-sequencing data	This paper	GEO: GSE112677
Experimental Models: Cell Lines		
Human: A375 cell line	ATCC	Cat# CRL-1619; RRID: CVCL_0132
Human: HEK-293T cell line	ATCC	Cat# CRL-3216; RRID: CVCL_0063
Human: SK-MEL-28 cell line	ATCC	Cat# HTB-72; RRID: CVCL_0526
Human: WM852 cell line	Rockland	Cat# WM852-01-0001; RRID:CVCL_6804
Human: WM983B cell line	Rockland	Cat# WM983B-01-0001; RRID:CVCL_6809
Human: 501Mel cell line	(Rubinfeld et al., 1997)	RRID: CVCL_4633
Human: 888Mel cell line	(Rubinfeld et al., 1997)	RRID: CVCL_4632
Human: M990514 short-term cell culture	URPP Live Tumor Cell Biobank, UZH	N/A

Human: M010817 short-term cell culture	URPP Live Tumor Cell Biobank, UZH	N/A
Human: M050829 short-term cell culture	URPP Live Tumor Cell Biobank, UZH	N/A
Human: M070302 short-term cell culture	URPP Live Tumor Cell Biobank, UZH	N/A
Human: M080423 short-term cell culture	URPP Live Tumor Cell Biobank, UZH	N/A
Human: M130604 short-term cell culture	URPP Live Tumor Cell Biobank, UZH	N/A
Human: M140130 short-term cell culture	URPP Live Tumor Cell Biobank, UZH	N/A
Mouse: RIM-1 short-term cell culture	(Zingg et al., 2015)	N/A
Mouse: RIM-3 short-term cell culture	(Zingg et al., 2015)	N/A
Mouse: RIH-1 short-term cell culture	This paper	N/A
Mouse: RIH-2 short-term cell culture	This paper	N/A
Experimental Models: Organisms/Strains		
Mouse: Hsd:Athymic Nude-*Foxn1*$^{nu/nu}$	Envigo	N/A
Mouse: *Tyr::CreER*^{T2}: B6.Cg-Tg(Tyr-cre/ERT2)13Bos/J	The Jackson Laboratory	Cat# 012328; RRID: IMSR_JAX:012328
Mouse: *R26R-LSL-LacZ*: B6;129S4-*Gt(ROSA)26Sor*^{tm1Sor}/J	The Jackson Laboratory	Cat# 003309; RRID: IMSR_JAX:003309
Mouse: *R26R-LSL-tdTomato*: B6.Cg-*Gt(ROSA)26Sor*$^{tm14(CAG-tdTomato)Hze}$/J	The Jackson Laboratory	Cat# 007914; RRID: IMSR_JAX:007914
Mouse: *Braf-LSL-Braf*^{V600E}: B6.129P2(Cg)-*Braf*^{tm1Mmcm}/J	The Jackson Laboratory	Cat# 017837; RRID: IMSR_JAX:017837
Mouse: *Pten*^{lox}: B6.129S4-*Pten*^{tm1Hwu}/J	The Jackson Laboratory	Cat# 006440; RRID: IMSR_JAX:006440
Mouse: *Ezh2*^{lox}: B6;B6129-Ezh2<tm1Yugo>/Hko	(Hirabayashi et al., 2009)	RIKEN_BRCM:RBRC05555
Mouse: *ColA1-LSL-Ezh2*^{Y646N}: Col1a1$^{tm1(CAG-Ezh2*)Meln}$	(Béguelin et al., 2013)	MGI: 5519911
Mouse: *Tyr::Nras*^{Q61K}: Tg(Tyr-NRAS*Q61K)1Bee	(Ackermann et al., 2005)	MGI: 3768645
Mouse: *Cdkn2a*$^{-/-}$: Cdkn2a^{tm1Rdp}	(Serrano et al., 1996)	MGI: 1857942
Oligonucleotides		
Mouse: Genotyping Primers, *Braf-LSL-Braf*^{V600E}	The Jackson Laboratory	Cat# 017837
Mouse: Genotyping Primers, *Pten*^{lox}	The Jackson Laboratory	Cat# 006440
Mouse: Genotyping Primers, *R26R-LSL-tdTomato*	The Jackson Laboratory	Cat# 007914
Mouse: Genotyping Primers, See Table S2	Microsynth	N/A
Mouse: Genomic DNA Primers, *Rpl30* Intron 2	Cell Signaling Technology	Cat# 7015P
Human: Genomic DNA Primers, *RPL30* Exon 3	Cell Signaling Technology	Cat# 7014P
Custom Genomic DNA Primers, See Table S2	Microsynth	N/A
Human: Custom RT^2 PCR Array, Spotted with Primary Cilium Gene and *GAPDH* primers	Qiagen	Cat# 330171
Custom cDNA Primers, See Table S2	Microsynth	N/A
Recombinant DNA		
Stealth siRNA Negative Control Med GC Duplex #2 (siCo)	Thermo Fisher Scientific	Cat# 12935112
Stealth siRNA targeting *FUZ* (siFUZ#1)	Thermo Fisher Scientific	Cat# HSS12946-0
Stealth siRNA targeting *FUZ* (siFUZ#2)	Thermo Fisher Scientific	Cat# HSS12946-2
Stealth siRNA targeting *FUZ* (siFUZ#3)	Thermo Fisher Scientific	Cat# HSS12946-1
Stealth siRNA targeting *IFT81* (siIFT81#1)	Thermo Fisher Scientific	Cat# HSS12077-6
Stealth siRNA targeting *IFT81* (siIFT81#2)	Thermo Fisher Scientific	Cat# HSS12077-7
Stealth siRNA targeting *IFT81* (siIFT81#3)	Thermo Fisher Scientific	Cat# HSS12077-5
Stealth siRNA targeting *WDR19* (siWDR19#1)	Thermo Fisher Scientific	Cat# HSS1-26738
Stealth siRNA targeting *WDR19* (siWDR19#2)	Thermo Fisher Scientific	Cat# HSS1-26737
Stealth siRNA targeting *WDR19* (siWDR19#3)	Thermo Fisher Scientific	Cat# HSS1-84043
pGIPZ-non-silencing shRNA-TurboGFP (shCo)	Dharmacon	Cat# RHS4346
pGIPZ-shKif3a-TurboGFP (shKif3a#1)	Dharmacon	Cat# RMM4431-20031-7419; Clone ID: V2LMM_122
pGIPZ-shKif3a-TurboGFP (shKif3a#2)	Dharmacon	Cat# RMM4431-20031-8662; Clone ID: V2LMM_14535

pGIPZ-shWdr19-TurboGFP (shWdr19#1)	Dharmacon	Cat# VGM5520-20037-9129; Clone ID: V3LMM_457206
pGIPZ-shWdr19-TurboGFP (shWdr19#2)	Dharmacon	Cat# VGM5520-20037-7417; Clone ID: V3LMM_457210
pcDNA3.1-FLAG-CTNNB1^{S33Y}	(Valenta et al., 2011)	N/A
pMuLE-ENTR-CMV-L1-R5	(Albers et al., 2015), Addgene	Cat# 62090
pMuLE-ENTR-SV40-eGFP-L5-L2	(Albers et al., 2015), Addgene	Cat# 62144
pLenti-X1-Puro-DEST	(Albers et al., 2015), Addgene	Cat# 17297
pMD2.G	D. Trono Lab, Addgene	Cat# 12259
psPAX2	D. Trono Lab, Addgene	Cat# 12260
pRetroX-IRES-ZsGreen1	Clontech	Cat# 632520
pRetroX-EZH2^{WT}-IRES-ZsGreen1	(Béguelin et al., 2013)	N/A
pRetroX-EZH2^{Y646N}-IRES-ZsGreen1	(Béguelin et al., 2013)	N/A
pCL-Ampho Retrovirus Packaging Vector	Novus Biologicals	Cat# NBP2-29541
Software and Algorithms		
Adobe Photoshop CS5	Adobe	http://www.adobe.com/products/photoshop.html
Bioconductor 3.0	N/A	https://www.bioconductor.org
CellProfiler 2.1.1	(Carpenter et al., 2006)	http://cellprofiler.org
deepTools2	(Ramírez et al., 2016)	https://deeptools.readthedocs.io/en/latest/
FastQC	Babraham Bioinformatics	http://www.bioinformatics.babraham.ac.uk/projects/fastqc/
FlowJo 7.6	Tree Star	https://www.flowjo.com
GraphPad Prism 7	GraphPad Software	https://www.graphpad.com
ImageJ 1	(Schneider et al., 2012)	http://imagej.net/ImageJ
Integrative Genomic Viewer	(Robinson et al., 2011)	http://software.broadinstitute.org/software/igv/
MethPrimer 2.0	(Li and Dahiya, 2002)	http://www.urogene.org/cgi-bin/methprimer/methprimer.cgi
PANTHER Classification System	(Mi et al., 2013)	http://www.pantherdb.org
Primer-BLAST	(Ye et al., 2012)	https://www.ncbi.nlm.nih.gov/tools/primer-blast/
R	The R Foundation	https://www.r-project.org
R package edgeR	(Robinson et al., 2010)	https://bioconductor.org/packages/release/bioc/html/edgeR.html
R package GenomicRanges	(Lawrence et al., 2013)	https://bioconductor.org/packages/release/bioc/html/GenomicRanges.html
STAR 2.5.1b	(Dobin et al., 2013)	https://github.com/alexdobin/STAR/releases
The UCSC Genome Browser	(Kent et al., 2002)	https://genome.ucsc.edu/index.html
Trimmomatic	(Bolger et al., 2014)	http://www.usadellab.org/cms/index.php?page=trimmomatic

Figure 1

Click here to download Figure Figure 1.tif

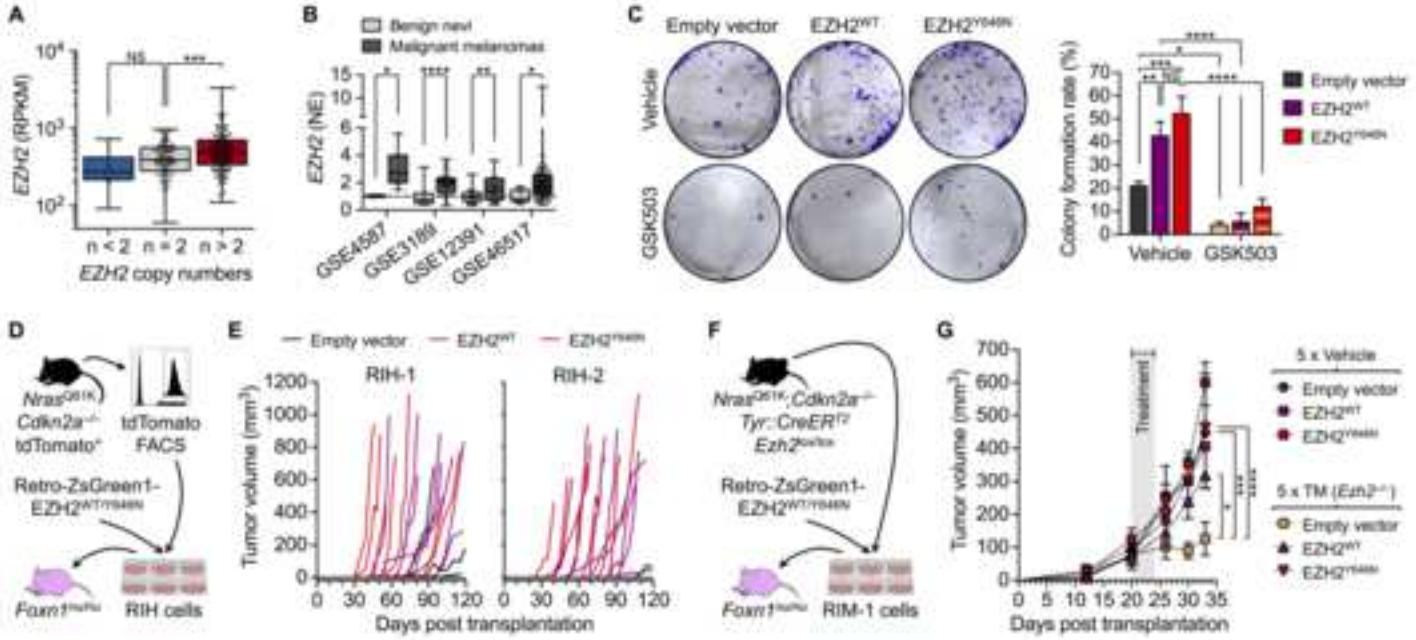

Figure 2

Click here to download Figure Figure 2.tif

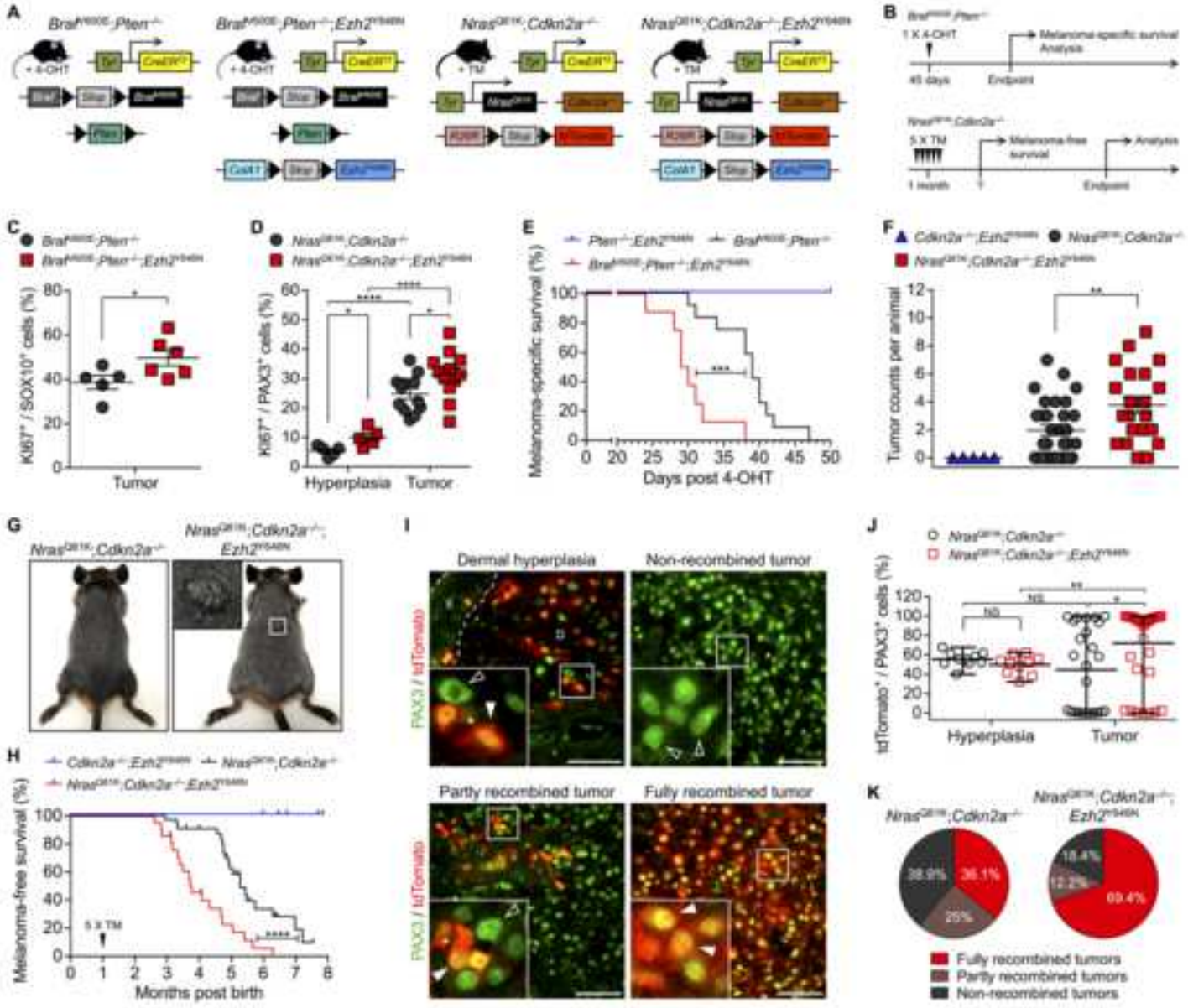

Figure 3

Click here to download Figure Figure 3.tif

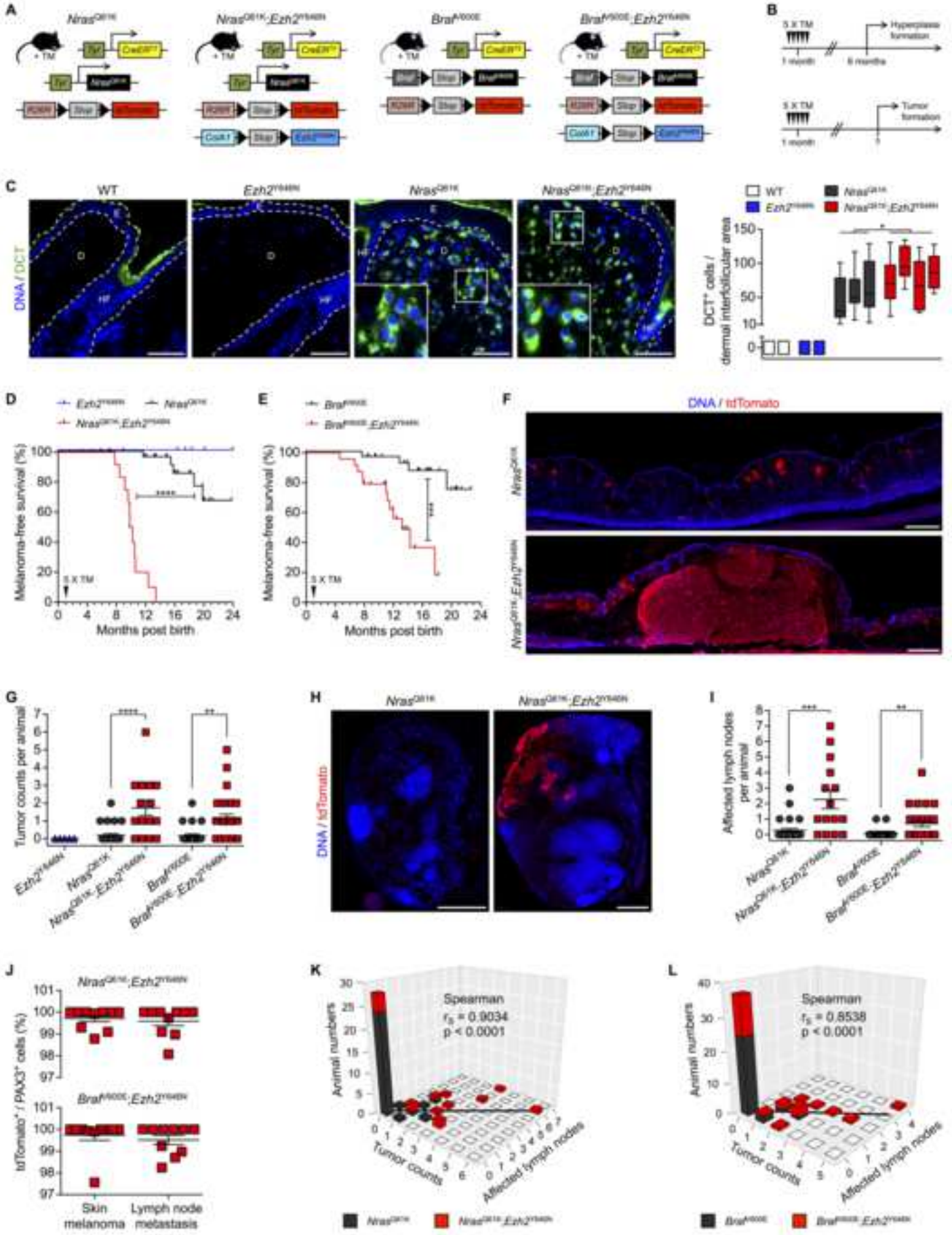

Figure 4

Click here to download Figure Figure 4.tif

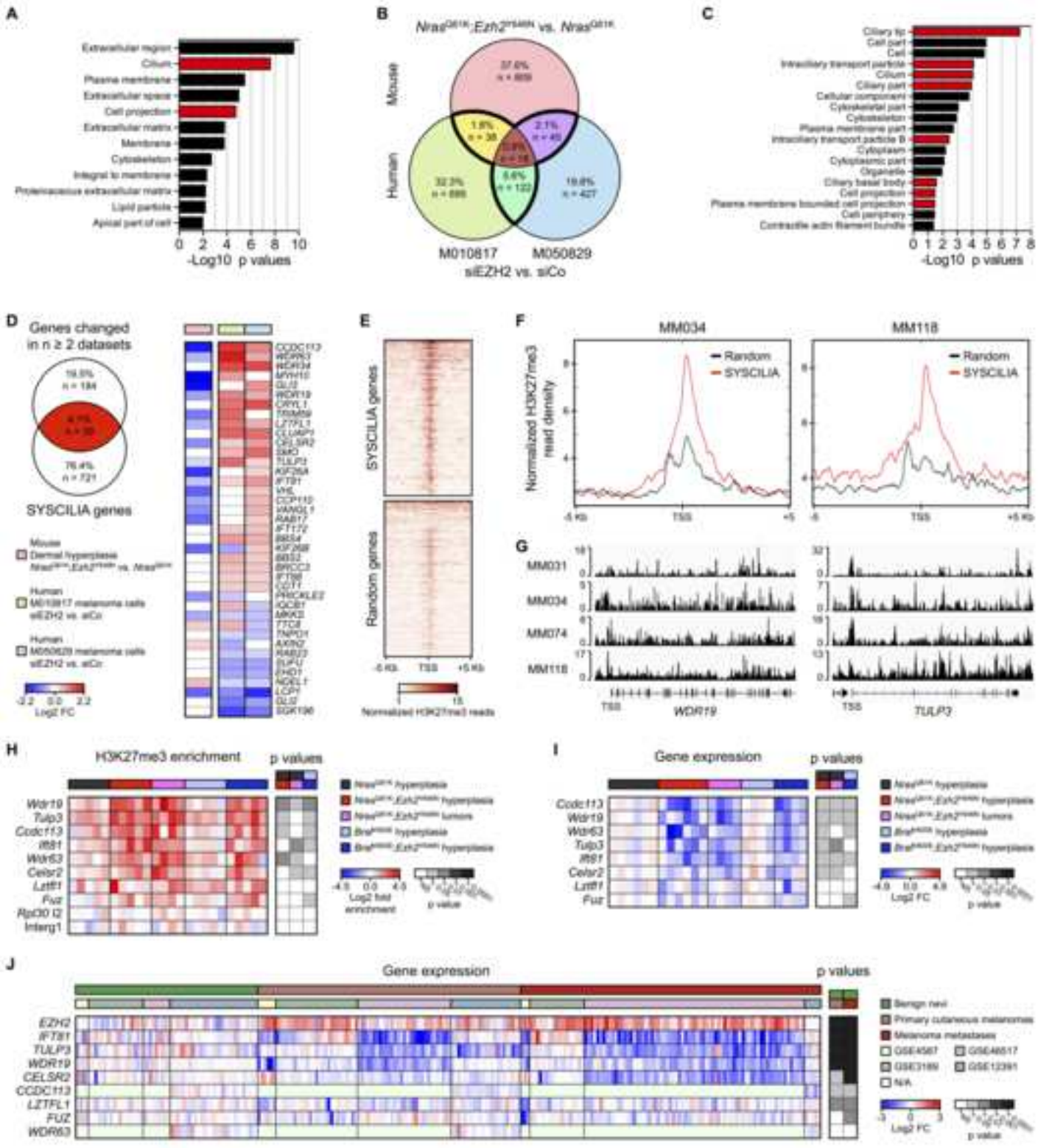

Figure 5

Click here to download Figure Figure 5.tif

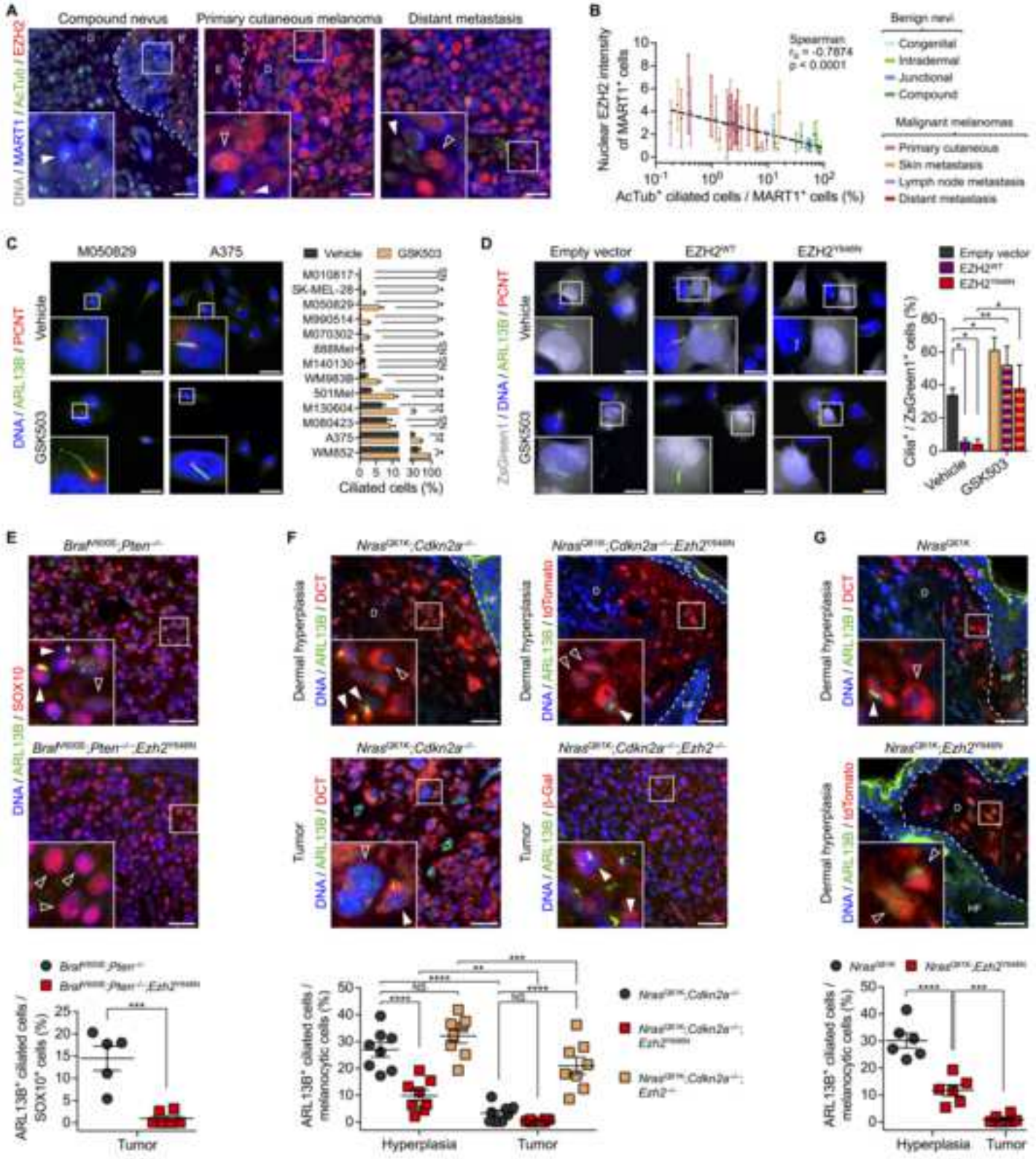

Figure 6

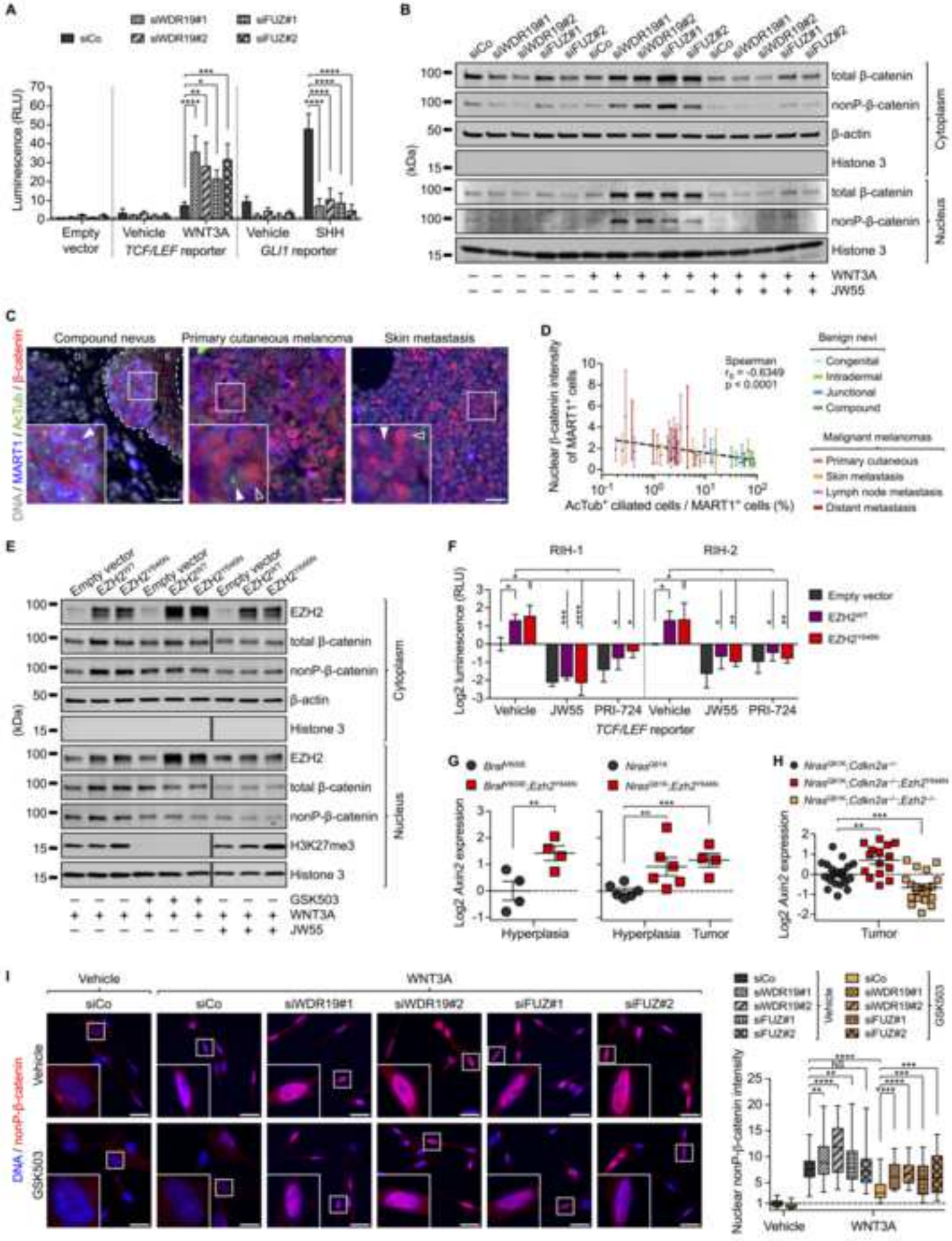

Figure 7

Click here to download Figure Figure 7.tif

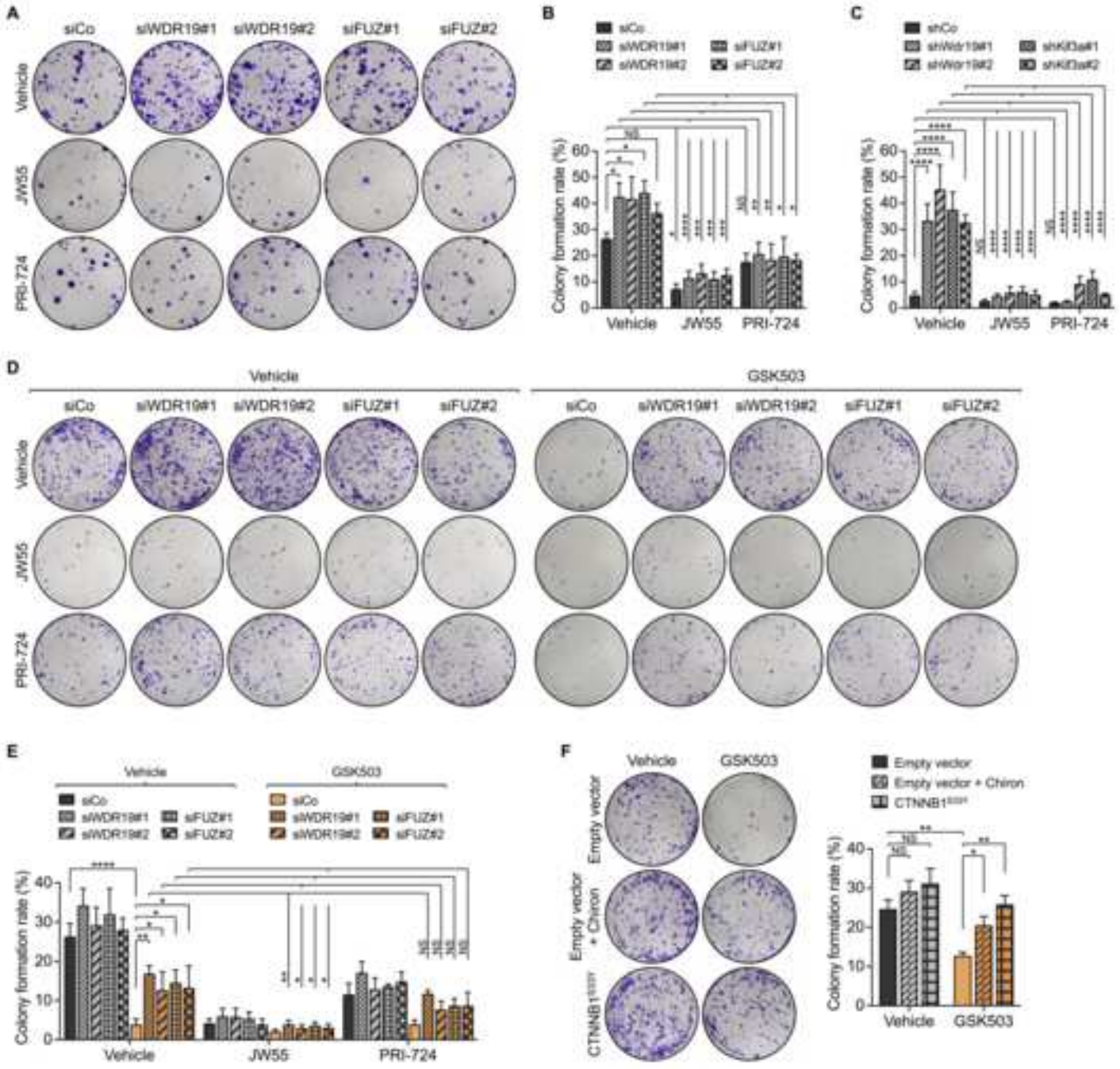

Figure 8

Click here to download Figure Figure 8.tif

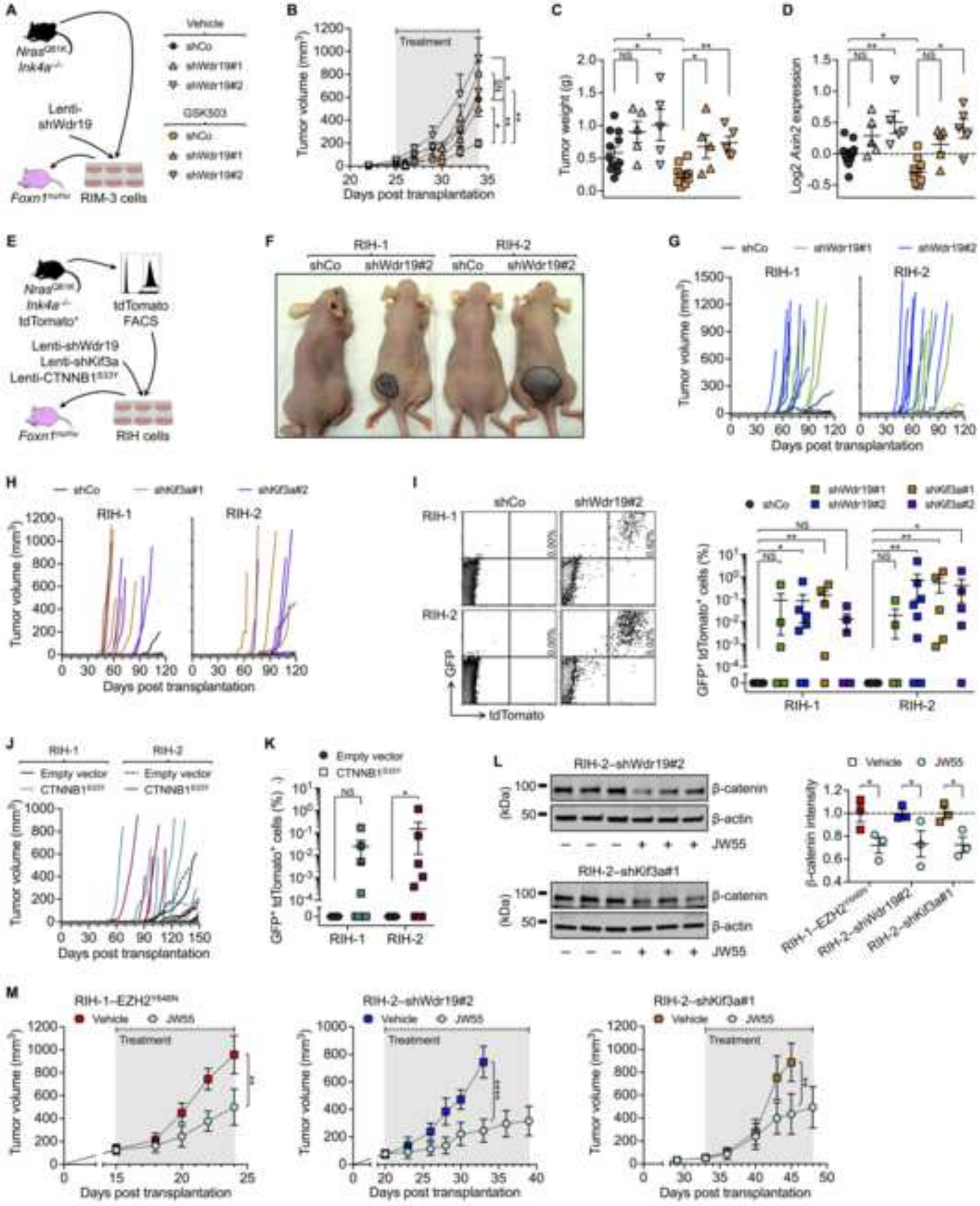

Supplemental Text and Figures

Click here to download Supplemental Text and Figures
180519_Zingg et al._SI.pdf

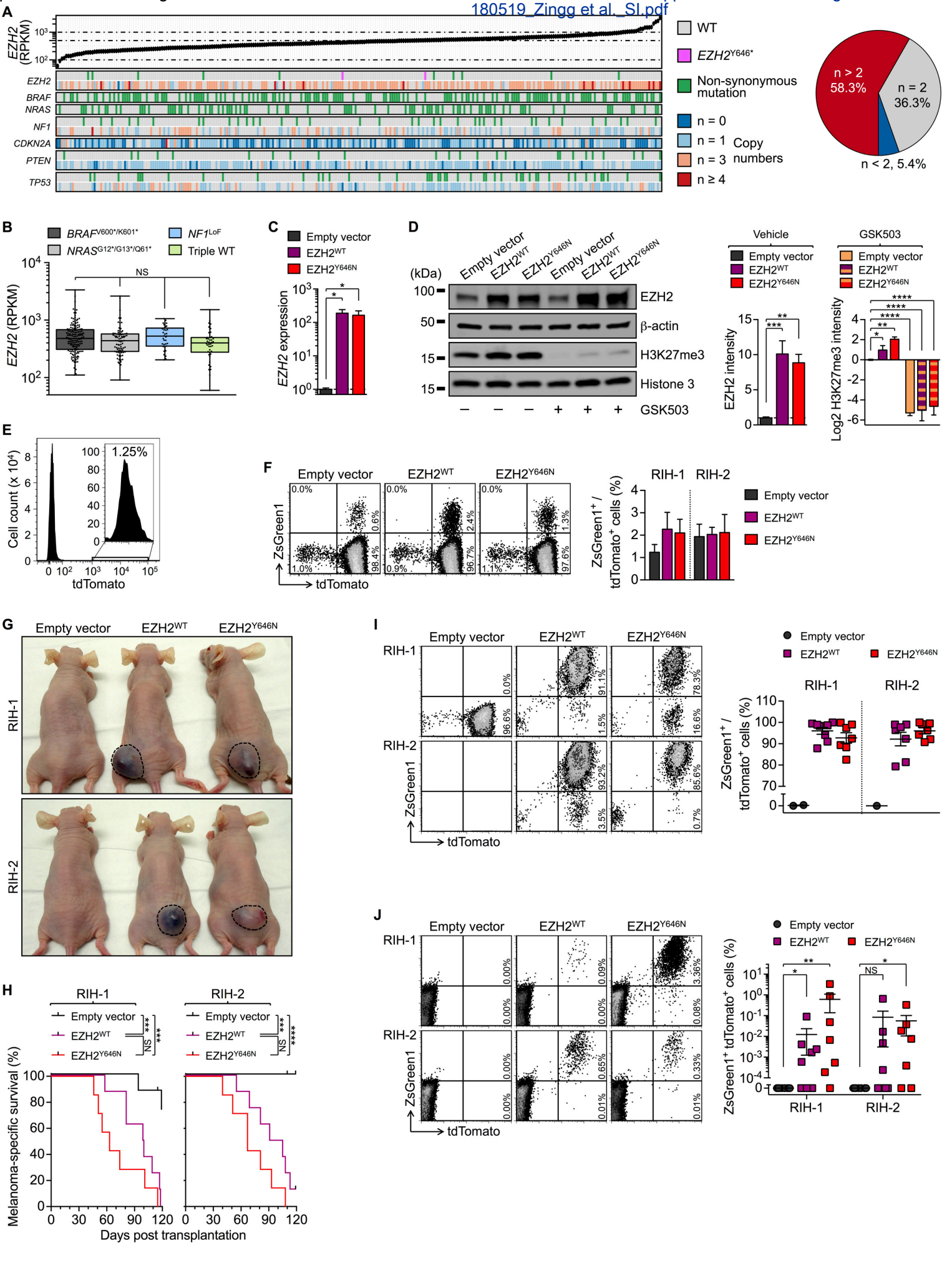

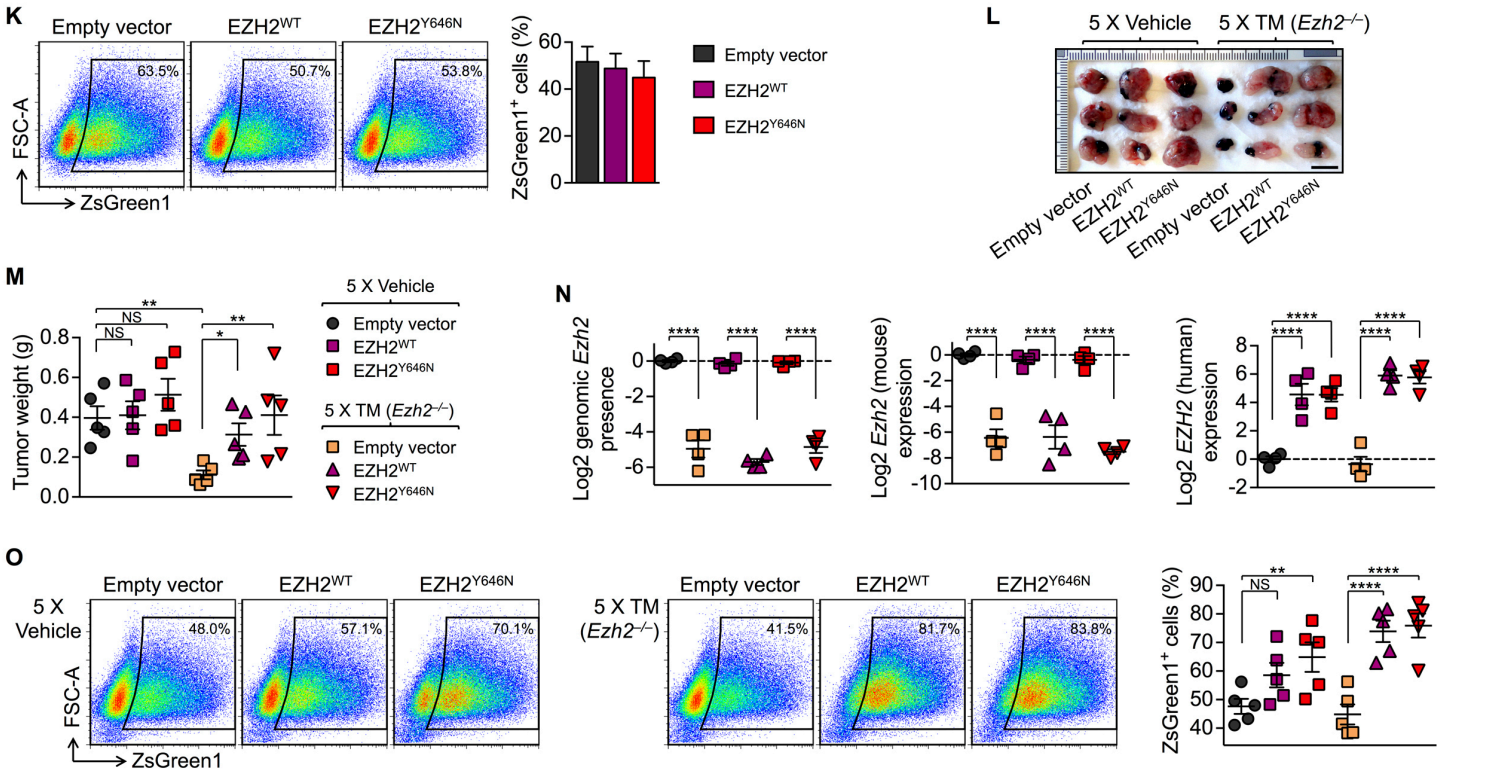

Figure S1, related to Figure 1. EZH2 overexpression accelerates melanomagenesis.

(A) Color-coded matrix of individual non-synonymous mutations and copy number changes arranged according to *EZH2* mRNA expression, and frequency of *EZH2* copy number changes (pie chart). Based on human skin cutaneous melanoma (SKCM) RSEM-normalized RNAseq, GISTIC2 copy number, and oncotated mutation datasets from The Cancer Genome Atlas (TCGA Network, 2015). Total specimen number, n = 278. (B) *EZH2* mRNA expression in TCGA-SKCM dataset segregated according to genetic subtypes. $BRAF^{V600*/K601*}$, n = 158; $NRAS^{G12*,G13*,Q61*}$, n = 83; $NF1^{LoF}$, n = 35; Triple wild-type (WT), n = 43. *NF1* loss-of-function (LoF) defined by *NF1* missense or nonsense mutation, frame shift insertion or deletion, and/or copy number loss, but $BRAF^{WT}$ and $NRAS^{WT}$. (C) *EZH2* mRNA expression in A375 after transfection with empty vector, $EZH2^{WT}$, or $EZH2^{Y646N}$-expression plasmids. (D) Western blots to quantify EZH2 protein and H3K27me3 intensities in A375 transfected with empty vector, $EZH2^{WT}$, or $EZH2^{Y646N}$-expression plasmids and treated with GSK503. (E) Fluorescence-activated cell sorting (FACS) to isolate tdTomato-traced RIH cells from homogenized dorsal skin (4 weeks post TM, 4-month-old mice). (F) FACS analyses to quantify retro-ZsGreen1-empty vector, $EZH2^{WT}$, or $EZH2^{Y646N}$ infection efficiencies in $tdTomato^{+}$ RIH cells. (G and H) Pictures (G) and Kaplan-Meier curves (H) comparing melanoma-specific survival of mice inoculated with RIH cells infected with retro-empty vector, $EZH2^{WT}$, or $EZH2^{Y646N}$. Empty vector, $EZH2^{WT}$, each n = 8; $EZH2^{Y646N}$, each n = 7 mice. (I) FACS analyses to quantify $ZsGreen1^{+}$ per $tdTomato^{+}$ cells in tumors from mice in (H). (J) FACS analyses to quantify $ZsGreen1^{+}$ $td\text{-}tomato^{+}$ RIH cells in lungs from mice in (H). (K) FACS analyses to quantify retro-ZsGreen1-empty vector, $EZH2^{WT}$, or $EZH2^{Y646N}$ infection efficiencies in RIM-1 cells. (L and M) Picture (L) and weight (M) of tumors derived from RIM-1 cells infected with retro-empty vector, $EZH2^{WT}$, or $EZH2^{Y646N}$, transplanted into Nude-$Foxn1^{nu/nu}$ mice, and treated with vehicle or tamoxifen (TM) to delete *Ezh2*. n = 5 mice per group. (N) Murine genomic *Ezh2* deletion, murine *Ezh2* mRNA expression, and human *EZH2* mRNA expression in tumors from (M). cDNA primers are specific for mouse *Ezh2* and human *EZH2*, respectively. Genomic primers amplify a fragment from murine *Ezh2* Intron 18, which lies within the floxed segment of the *Ezh2* locus (Hirabayashi et al., 2009). (O) FACS analyses to quantify $ZsGreen1^{+}$ cells in tumors from (M). Scale bars, 50 μm. Data are represented as median ± interquartile range (box) and ± 100% range (whiskers) (B) or as mean ± standard error of the mean (SEM) (C, D, F, I–K, and M–O) of 3 (C) or 5 (D) independent experiments. p values calculated with analysis of variance (ANOVA) and Fisher's least significant difference (LSD) test (B–D, J, and M–O), log-rank (Mantel-Cox) test (H), Kruskal-Wallis test with Dunn's multiple comparisons test (J), or unpaired Student's *t*-test (N). NS, not significant, *$p < 0.05$, **$p < 0.01$, ***$p < 0.001$, ****$p < 0.0001$.

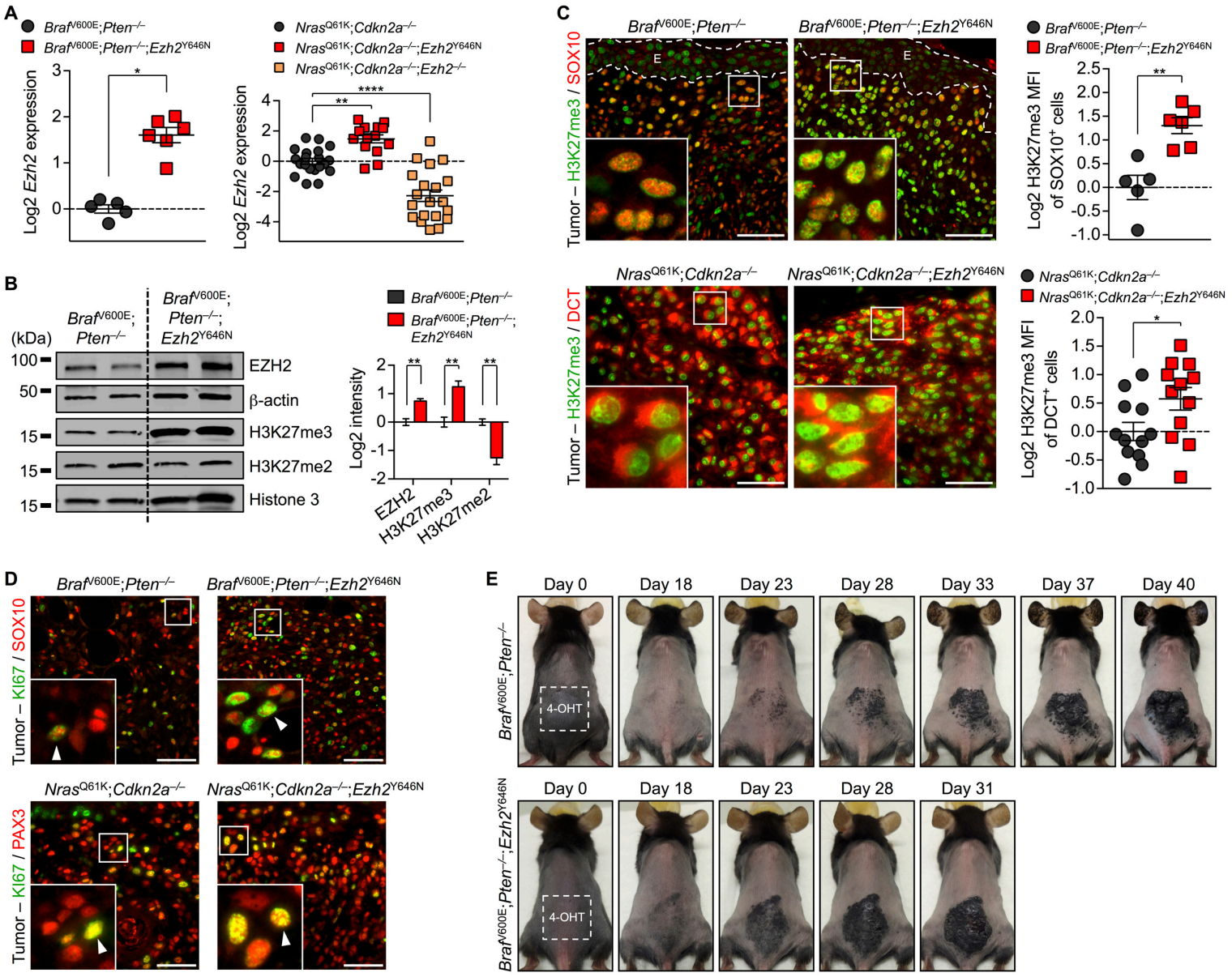

Figure S2, related to Figure 2. *Ezh2*^{Y646N} promotes murine melanoma formation.

(A) *Ezh2* mRNA expression in melanomas. *Braf*^{V600E};*Pten*$^{-/-}$, n = 5 of 5; *Braf*^{V600E};*Pten*$^{-/-}$;*Ezh2*^{Y646N}, n = 6 of 6; *Nras*^{Q61K};*Cdkn2a*$^{-/-}$, n = 20 of 14; *Nras*^{Q61K};*Cdkn2a*$^{-/-}$;*Ezh2*^{Y646N}, n = 15 of 10; and *Nras*^{Q61K};*Cdkn2a*$^{-/-}$;*Ezh2*$^{-/-}$, n = 20 of 13 mice. (B) Western blots to quantify EZH2 protein, H3K27me3, and H3K27me2 intensities. n = 3 tumors of 3 mice per group. (C) Immunofluorescence staining for H3K27me3 and SOX10 or DCT to quantify H3K27me3 intensities. E, epidermis. Tumors, *Braf*^{V600E};*Pten*$^{-/-}$, n = 5 of 5; *Braf*^{V600E};*Pten*$^{-/-}$;*Ezh2*^{Y646N}, n = 6 of 6; *Nras*^{Q61K};*Cdkn2a*$^{-/-}$, n = 12 of 9; and *Nras*^{Q61K};*Cdkn2a*$^{-/-}$;*Ezh2*^{Y646N}, n = 12 of 10 mice. (D) Immunofluorescence staining for KI67 and SOX10 or PAX3. Quantifications are in Figures 2C and 2D. Arrowhead, KI67^{+} and SOX10^{+} or PAX3^{+} cell. (E) *Braf*^{V600E};*Pten*$^{-/-}$ and *Braf*^{V600E};*Pten*$^{-/-}$;*Ezh2*^{Y646N} animal during melanoma development post topical 4 hydroxytamoxifen (4-OHT) application. Scale bars, 50 μm. Data are represented as mean ± SEM. p values calculated with unpaired Student's *t*-test (A–C) or ANOVA and Fisher's LSD test (A).

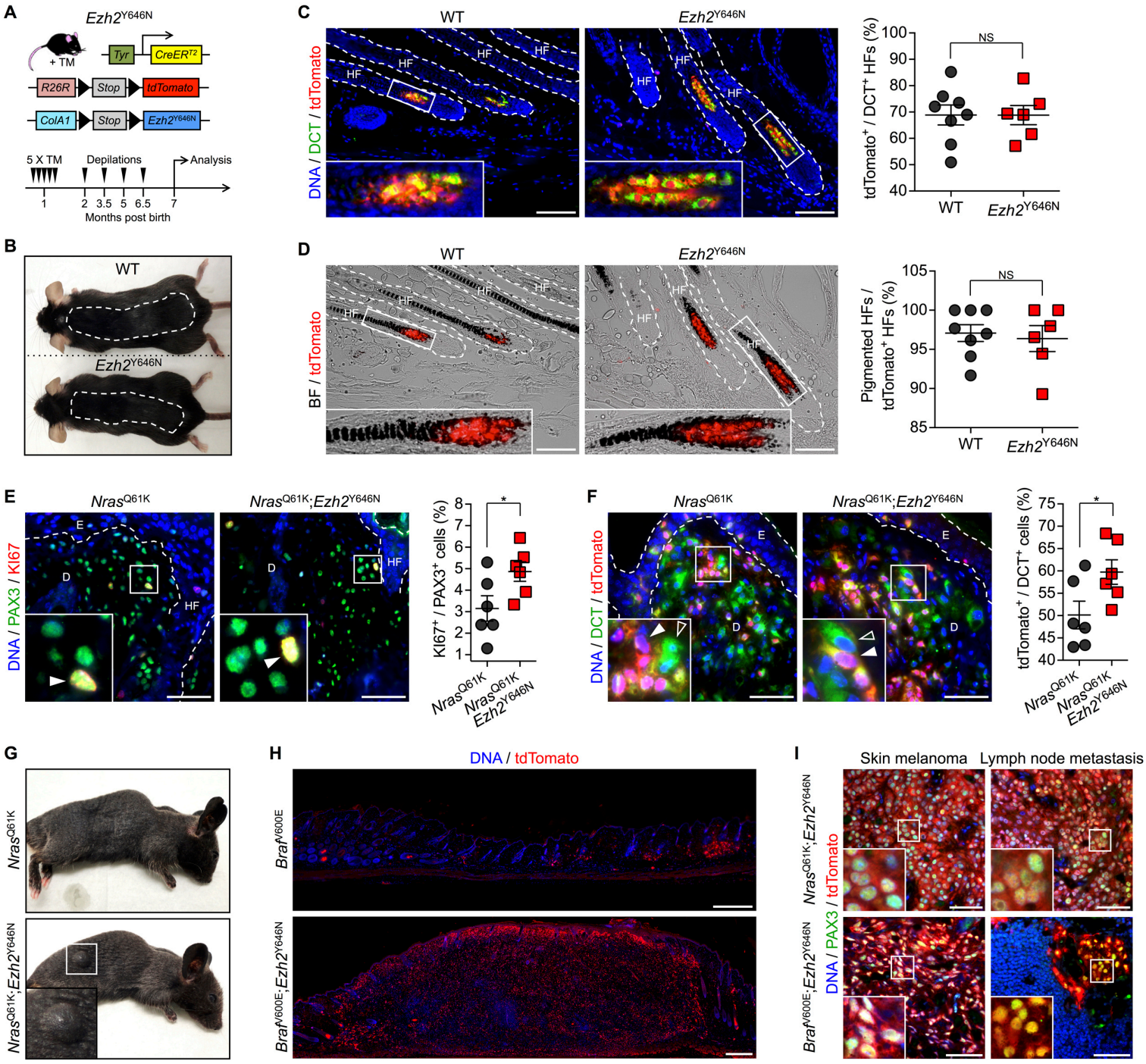

Figure S3, related to Figure 3. *Ezh2*^{Y646N} is a driver of murine metastatic melanoma.

(A) Mouse genotype and strategy used to analyze the effect of conditional *Ezh2*^{Y646N} activation in the melanocytic lineage of adult WT mice. (B) WT and *Ezh2*^{Y646N} animal post TM administration and 4 cycles of hair depilation in labeled area on back skin. (C and D) Endogenous tdTomato fluorescence and immunofluorescence staining for DCT or bright field (BF) to quantify recombined hair follicles (HF) (C) and pigmented HFs (D) in dorsal skin. Scale bars, 100 µm. WT, n = 8; *Ezh2*^{Y646N}, n = 6 mice. (E and F) Immunofluorescence staining for PAX3, DCT, KI67, and tdTomato on dermal hyperplasia to quantify proliferative (E) and recombined (F) cells 5 months post TM administration. D, dermis. Arrowhead, PAX3^{+} KI67^{+} or DCT^{+} tdTomato^{+} cell; empty arrowhead, DCT^{+} tdTomato^{-} cell. Scale bars, 50 µm. n = 6 mice per group. (G) *Nras*^{Q61K} and *Nras*^{Q61K};*Ezh2*^{Y646N} animal 12 months post TM administration. (H) Immunofluorescence staining for tdTomato on dorsal skin. Quantifications are in Figure 3G. Scale bars, 1 mm. (I) Immunofluorescence staining for PAX3 and tdTomato on skin melanomas and lymph node metastases. Quantifications are in Figure 3J. Scale bars, 50 µm. Data are represented as mean ± SEM. p values calculated with unpaired Student's *t*-test.

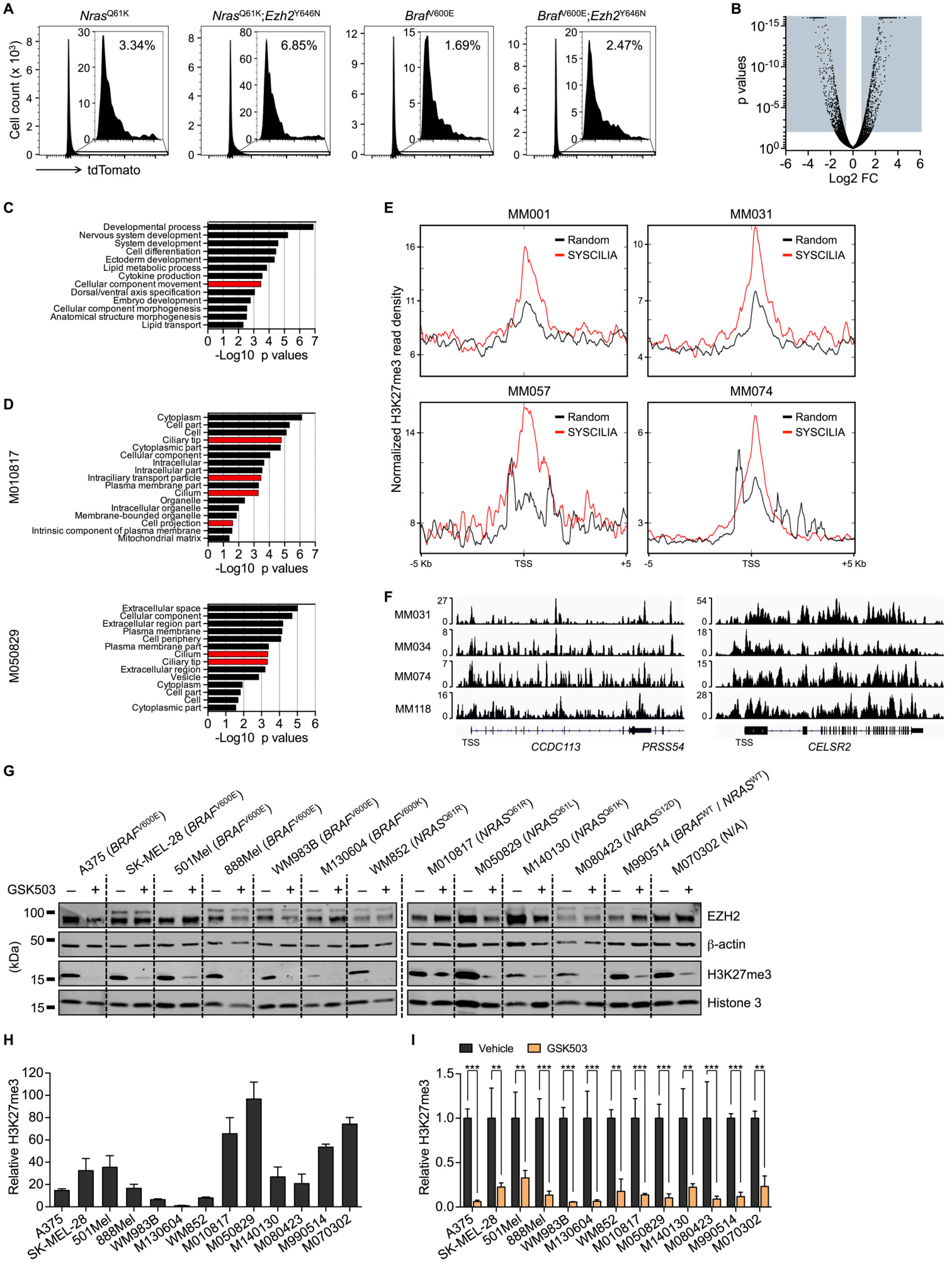
A
Nras^Q61K
Nras^Q61K;Ezh2^Y646N
Braf^V600E
Braf^V600E;Ezh2^Y646N
3.34%
6.85%
1.69%
2.47%
Cell count (x 10^3)
tdTomato
B
p values
Log2 FC
C
Developmental process
Nervous system development
System development
Cell differentiation
Ectoderm development
Lipid metabolic process
Cytokine production
Cellular component movement
Dorsal/ventral axis specification
Embryo development
Cellular component morphogenesis
Anatomical structure morphogenesis
Lipid transport
-Log10 p values
D
M010817
Cytoplasm
Cell part
Cell
Ciliary tip
Cytoplasmic part
Cellular component
Intracellular
Intracellular part
Intraciliary transport particle
Plasma membrane part
Cilium
Organelle
Intracellular organelle
Membrane-bounded organelle
Cell projection
Intrinsic component of plasma membrane
Mitochondrial matrix
-Log10 p values
M050829
Extracellular space
Cellular component
Extracellular region part
Plasma membrane
Cell periphery
Plasma membrane part
Cilium
Ciliary tip
Extracellular region
Vesicle
Cytoplasm
Cell part
Cell
Cytoplasmic part
-Log10 p values
E
MM001
MM031
MM057
MM074
Random
SYSCILIA
Normalized H3K27me3 read density
-5 Kb
TSS
+5
-5
+5 Kb
F
MM031
MM034
MM074
MM118
TSS
CCDC113
PRSS54
CELSR2
G
A375 (BRAF^V600E)
SK-MEL-28 (BRAF^V600E)
501Mel (BRAF^V600E)
888Mel (BRAF^V600E)
WM983B (BRAF^V600E)
M130604 (BRAF^V600K)
WM852 (NRAS^Q61R)
M010817 (NRAS^Q61R)
M050829 (NRAS^Q61L)
M140130 (NRAS^Q61K)
M080423 (NRAS^G12D)
M990514 (BRAF^WT / NRAS^WT)
M070302 (N/A)
GSK503
(kDa)
EZH2
β-actin
H3K27me3
Histone 3
H
Relative H3K27me3
A375
SK-MEL-28
501Mel
888Mel
WM983B
M130604
WM852
M010817
M050829
M140130
M080423
M990514
M070302
I
Vehicle
GSK503
Relative H3K27me3

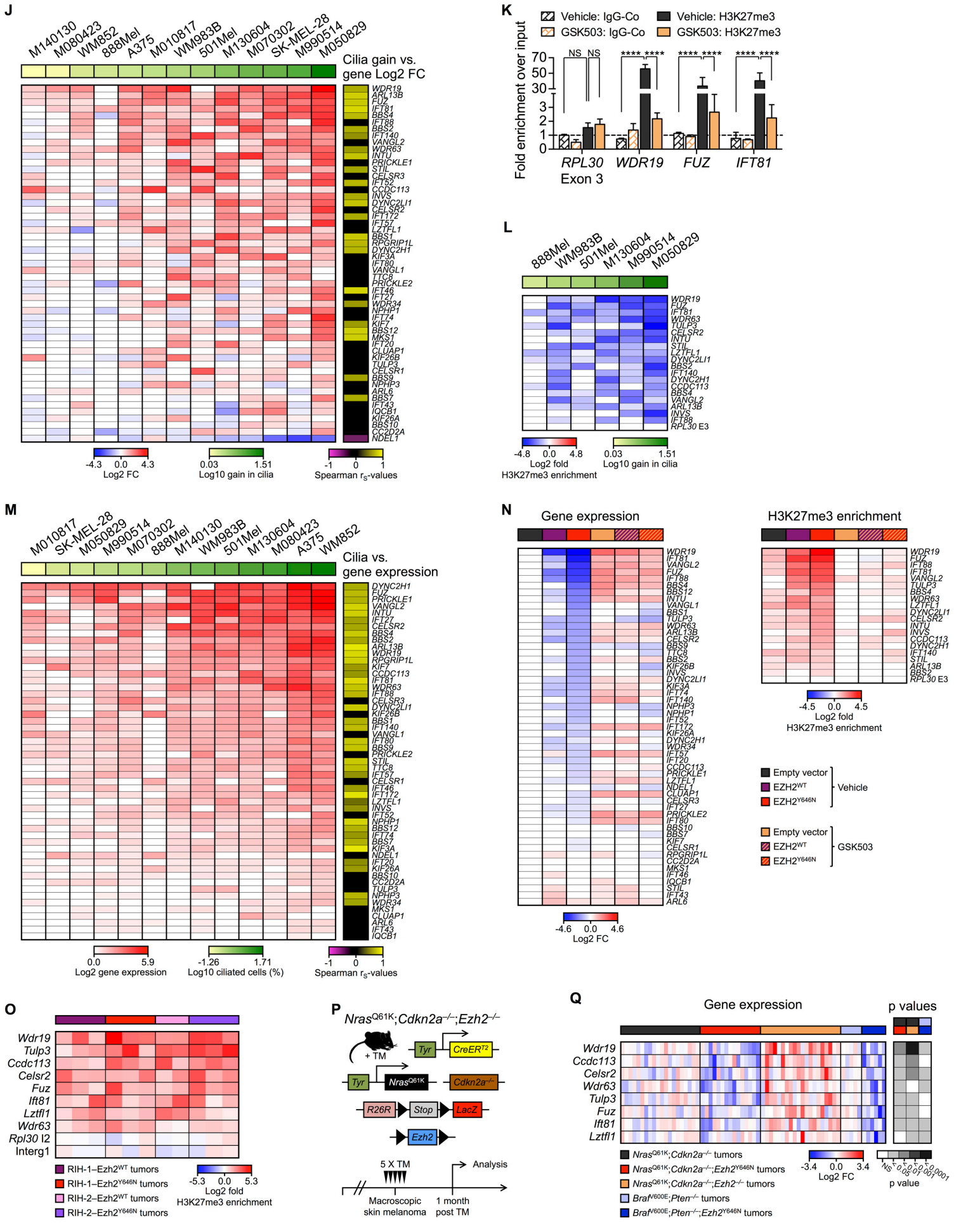
J
M140130
M080423
WM852
888Mel
A375
M010817
WM983B
501Mel
M130604
M070302
SK-MEL-28
M990514
M050829
Cilia gain vs.
gene Log2 FC
WDR19
ARL13B
FUZ
IFT81
BBS4
IFT88
BBS2
IFT140
VANGL2
WDR63
INTU
PRICKLE1
STIL
CELSR3
IFT52
CCDC113
INVS
DYNC2LI1
CELSR2
IFT172
IFT57
LZTFL1
BBS1
RPGRIP1L
DYNC2H1
KIF3A
IFT80
VANGL1
TTC8
PRICKLE2
IFT46
IFT27
WDR34
NPHP1
IFT74
KIF7
BBS12
MKS1
IFT20
CLUAP1
KIF26B
TULP3
CELSR1
BBS9
NPHP3
ARL6
BBS7
IFT43
IQCB1
KIF26A
BBS10
CC2D2A
NDEL1
-4.3 0.0 4.3
Log2 FC
0.03 1.51
Log10 gain in cilia
-1 0 1
Spearman rS-values
K
Vehicle: IgG-Co
Vehicle: H3K27me3
GSK503: IgG-Co
GSK503: H3K27me3
Fold enrichment over input
70
50
30
3
2
1
0
NS NS
**** ****
**** ****
**** ****
RPL30
WDR19
FUZ
IFT81
Exon 3
L
888Mel
WM983B
501Mel
M130604
M990514
M050829
WDR19
FUZ
IFT81
WDR63
TULP3
CELSR2
INTU
STIL
LZTFL1
DYNC2LI1
BBS2
IFT140
DYNC2H1
CCDC113
BBS4
VANGL2
ARL13B
INVS
IFT88
RPL30 E3
-4.8 0.0 4.8
Log2 fold
H3K27me3 enrichment
0.03 1.51
Log10 gain in cilia
M
M010817
SK-MEL-28
M050829
M990514
M070302
888Mel
M140130
WM983B
501Mel
M130604
M080423
A375
WM852
Cilia vs.
gene expression
DYNC2H1
FUZ
PRICKLE1
VANGL2
INTU
IFT27
CELSR2
BBS4
BBS2
ARL13B
WDR19
RPGRIP1L
KIF7
CCDC113
IFT81
WDR63
IFT88
CELSR3
DYNC2LI1
KIF26B
BBS1
IFT140
VANGL1
IFT80
BBS9
PRICKLE2
STIL
TTC8
IFT57
CELSR1
IFT46
IFT172
LZTFL1
INVS
IFT52
NPHP1
BBS12
IFT74
BBS7
KIF3A
NDEL1
IFT27
KIF26A
BBS10
CC2D2A
TULP3
NPHP3
WDR34
MKS1
CLUAP1
ARL6
IFT43
IQCB1
0.0 5.9
Log2 gene expression
-1.26 1.71
Log10 ciliated cells (%)
-1 0 1
Spearman rS-values
N
Gene expression
H3K27me3 enrichment
WDR19
IFT81
VANGL2
FUZ
IFT88
BBS4
BBS12
INTU
VANGL1
BBS1
TULP3
WDR63
ARL13B
CELSR2
BBS9
TTC8
BBS2
KIF26B
INVS
DYNC2LI1
KIF3A
IFT74
IFT140
NPHP3
NPHP1
IFT52
IFT172
KIF26A
DYNC2H1
WDR34
IFT57
IFT20
CCDC113
PRICKLE1
LZTFL1
NDEL1
CLUAP1
CELSR3
IFT27
PRICKLE2
IFT80
BBS10
BBS7
KIF7
CELSR1
RPGRIP1L
CC2D2A
MKS1
IFT46
IQCB1
STIL
IFT43
ARL6
FUZ
IFT88
IFT81
VANGL2
TULP3
BBS4
WDR63
LZTFL1
DYNC2LI1
CELSR2
INTU
CCDC113
DYNC2H1
IFT140
STIL
ARL13B
BBS2
RPL30 E3
-4.6 0.0 4.6
Log2 FC
-4.5 0.0 4.5
Log2 fold
H3K27me3 enrichment
Empty vector
EZH2WT
EZH2Y646N
Vehicle
Empty vector
EZH2WT
EZH2Y646N
GSK503
O
Wdr19
Tulp3
Ccdc113
Celsr2
Fuz
Ift81
Lztfl1
Wdr63
Rpl30 l2
Interg1
RIH-1–Ezh2WT tumors
RIH-1–Ezh2Y646N tumors
RIH-2–Ezh2WT tumors
RIH-2–Ezh2Y646N tumors
-5.3 0.0 5.3
Log2 fold
H3K27me3 enrichment
P
NrasQ61K;Cdkn2a−/−;Ezh2−/−
+ TM
Tyr
CreERT2
Tyr
NrasQ61K
Cdkn2a−/−
R26R
Stop
LacZ
Ezh2
5 X TM
Analysis
Macroscopic
skin melanoma
1 month
post TM
Q
Gene expression
p values
Wdr19
Ccdc113
Celsr2
Wdr63
Tulp3
Fuz
Ift81
Lztfl1
NrasQ61K;Cdkn2a−/− tumors
NrasQ61K;Cdkn2a−/−;Ezh2Y646N tumors
NrasQ61K;Cdkn2a−/−;Ezh2−/− tumors
BrafV600E;Pten−/− tumors
BrafV600E;Pten−/−;Ezh2Y646N tumors
-3.4 0.0 3.4
Log2 FC
Ns
0.05
0.01
0.001
0.0001
p value

Figure S4, related to Figure 4. EZH2 suppresses transcription of primary cilium genes.

(A) FACS to isolate tdTomato-traced *Nras*^{Q61K}, *Nras*^{Q61K};*Ezh2*^{Y646N}, *Braf*^{V600E}, and *Braf*^{V600E};*Ezh2*^{Y646N} hyperplasia cells from homogenized dorsal skin (4 weeks post TM, 10-week-old mice). (B) RNA-sequencing on murine FACS-isolated *Nras*^{Q61K};*Ezh2*^{Y646N} versus (vs.) *Nras*^{Q61K} hyperplasia cells. n = 2 per group. FDR < 0.005, p < 0.01, Log2 fold change (FC) > +0.7 / < –0.7 was considered significant. (C) PANTHER GO-slim biological processes analysis using Overrepresentation Test and Fisher's Exact test with FDR multiple test correction (Mi et al., 2013) on RNA-sequencing data from murine FACS-isolated *Nras*^{Q61K};*Ezh2*^{Y646N} vs. *Nras*^{Q61K} hyperplasia cells. (D) PANTHER GO cellular component complete analysis using Overrepresentation Test and Bonferroni correction (Mi et al., 2013) on transcriptome data from M010817 and M050829 melanoma cell cultures after *EZH2* RNAi (GSE63165). (E) Enrichment plots showing normalized read densities of H3K27me3 at the transcription start site (TSS) of SYSCILA (van Dam et al., 2013) and random genes (each n = 760) in human melanoma cell cultures (GSE60666). Tracks are centered to the TSS and extend ± 5 Kb. (F) Genome browser tracks showing H3K27me3 at *CCDC113* and *CELSR2* loci in human melanoma cell cultures (GSE60666). (G–I) Western blots for EZH2 and H3K27me3 (G) to quantify global H3K27me3 levels (H) and efficacy of GSK503 (I) in melanoma cell lines. N/A, not available. (J) Heatmap showing ciliary gene mRNA FCs in melanoma cell lines treated with GSK503 vs. vehicle and analyzed with Custom RT^2 PCR Array spotted with primers for human primary cilium genes. Log10 gains in cilia values are based on Figure 4C. Correlations are calculated across cell lines comparing FCs of individual genes versus Log10 gain in cilia. Colored squares indicate significant FC or Spearman's rank correlation coefficient (r_S) (p < 0.05). (K) ChIP-qPCR on chromatin from M050829 cells treated with GSK503 vs. vehicle. A control IgG antibody (IgG-Co) or an antibody against H3K27me3, primers amplifying the negative control genomic sequence of *RPL30* Exon 3 (E3), and primers flanking the transcriptional start sites (TSS) of key ciliary genes were used. Data was normalized to input and IgG-Co sample of cells treated with vehicle. (L) Heatmap showing H3K27me3 enrichments in TSS of ciliary genes. ChIP-qPCR normalized to input and H3K27me3 enrichments in vehicle-treated samples. Colored squares indicate significant fold enrichment (p < 0.05). Conditions as in (J). (M) Heatmap showing relative ciliary gene expression in melanoma cell lines. Log10 percentages of ciliated cells are based on Figure 4C. Correlations are calculated across cell lines comparing relative gene expression versus Log10 ciliated cells. Colored squares indicate significant relative increase in gene expression compared to the lowest value (normalized per gene) or significant Spearman's r_S (p < 0.05). (N) Heatmaps showing ciliary gene mRNA FCs and H3K27me3 enrichments in TSS of ciliary genes. Material from A375 transfected with empty vector, EZH2^{WT}, or EZH2^{Y646N}-expression plasmids and treated with GSK503 vs. vehicle. mRNA expressions analyzed with Custom RT^2 PCR Array spotted with primers for human primary cilium genes. ChIP-qPCR normalized to input and H3K27me3 enrichment in *RPL30* E3 of empty vector-transfected and vehicle-treated samples. Colored squares, significant FCs over this enrichment or individual gene expressions of empty vector-transfected and vehicle-treated samples (p < 0.05). (O) Heatmap showing H3K27me3 enrichments in TSS of ciliary genes. ChIP-qPCR normalized to input and H3K27me3 enrichment in *Rpl30* Intron 2 (I2) and intergenic region 1 (Interg1) of all RIH tumors. Tumors, RIH-2–EZH2^{WT}, n = 2 of 2; other groups, n = 3 of 3 mice. (P) Mouse genotypes and strategy used to analyze the effect of conditional *Ezh2* deletion in established melanoma of adult *Nras*^{Q61K};*Cdkn2a*$^{-/-}$ mice. (Q) Heatmaps showing ciliary gene FCs in murine samples and p values from comparisons of individual groups. Tumors, *Nras*^{Q61K};*Cdkn2a*$^{-/-}$, n = 20 of 14; *Nras*^{Q61K};*Cdkn2a*$^{-/-}$;*Ezh2*^{Y646N}, n = 15 of 10; *Nras*^{Q61K};*Cdkn2a*$^{-/-}$;*Ezh2*$^{-/-}$, n = 20 of 13; *Braf*^{V600E};*Pten*$^{-/-}$, n = 5 of 5; and *Braf*^{V600E};*Pten*$^{-/-}$;*Ezh2*^{Y646N}, n = 6 of 6 mice. Data are represented as mean ± SEM (H, I, and K) or as mean (J and L–N) of 3 independent experiments. p values calculated with unpaired Student's *t*-test (I, J, and L), Spearman's r_S (J and M), or ANOVA and Fisher's LSD test (K, M–O, and Q).

Table S1, related to Figure 4. Tumor suppressor genes.

Gene	FDR	Log2 FC	p value
Apc	0.9658	-0.05719	0.8367
Cdkn1a	0.1426	0.6449	0.01819
Cdkn1b	0.6288	-0.3408	0.2096
Coro1a	0.8688	-0.2961	0.5146
Cdkn2a	0.905	0.2504	0.6022
Cdkn2b	0.7617	0.2809	0.3303
Cdkn2c	0.9398	-0.109	0.7207
Nf1	0.7261	-0.2861	0.2923
Nf2	0.899	-0.148	0.5869
Pten	0.6614	-0.3319	0.2347
Rb1	0.9598	0.06783	0.8032
Trp53	0.7921	-0.2464	0.3684

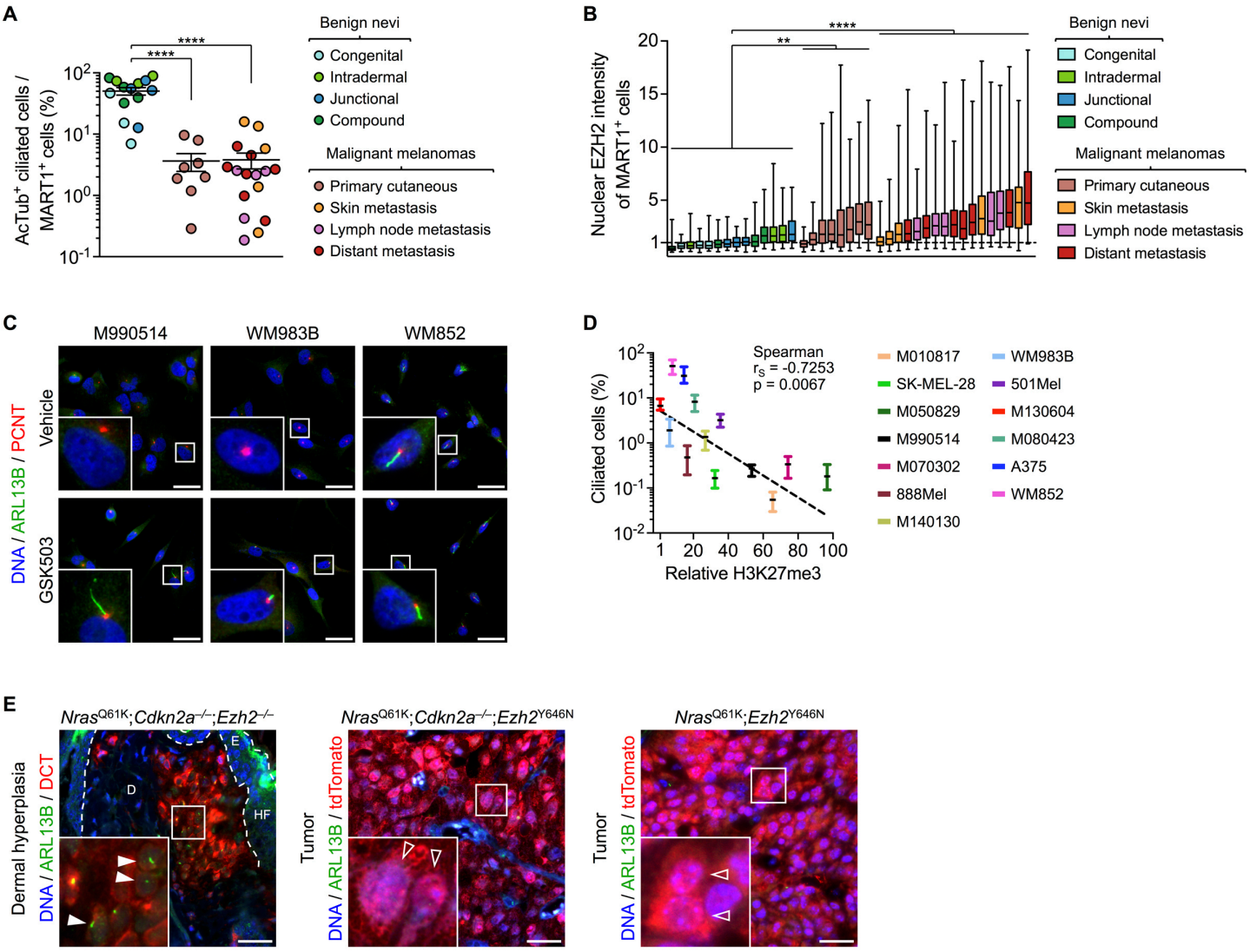

Figure S5, related to Figure 5. EZH2 expression leads to deconstruction of the primary cilium organelle.

(A and B). Quantifications of ciliation (A) and nuclear EZH2 intensity (B) of MART1^{+} melanocytic lesions. Based on immunofluorescence stainings in Figure 5A and sample numbers as in Figure 5B. (C) Immunofluorescence staining for ARL13B and PCNT to label ciliated melanoma cells during GSK503 treatment. Quantifications are in Figure 5C. (D) Correlation of relative H3K27me3 and percentages of ciliated melanoma cells. Based on data from Figures 5C and S4H. (E) Immunofluorescence stainings for ARL13B and DCT or tdTomato on melanomas and adjacent hyperplasia. Arrowhead, ARL13B (cilia)$^{+}$ DCT^{+} cell; empty arrowhead, ARL13B (cilia)$^{-}$ tdTomato^{+} cell. Quantifications are in Figures 5F and 5G. Scale bars, 25 µm. Data are represented as mean ± SEM (A), as median ± interquartile range (box) and ± 100% range (whiskers) (B), or as mean ± 100% range (D). p values calculated with ANOVA and Fisher's LSD test (A and B) or Spearman's r_S (D).

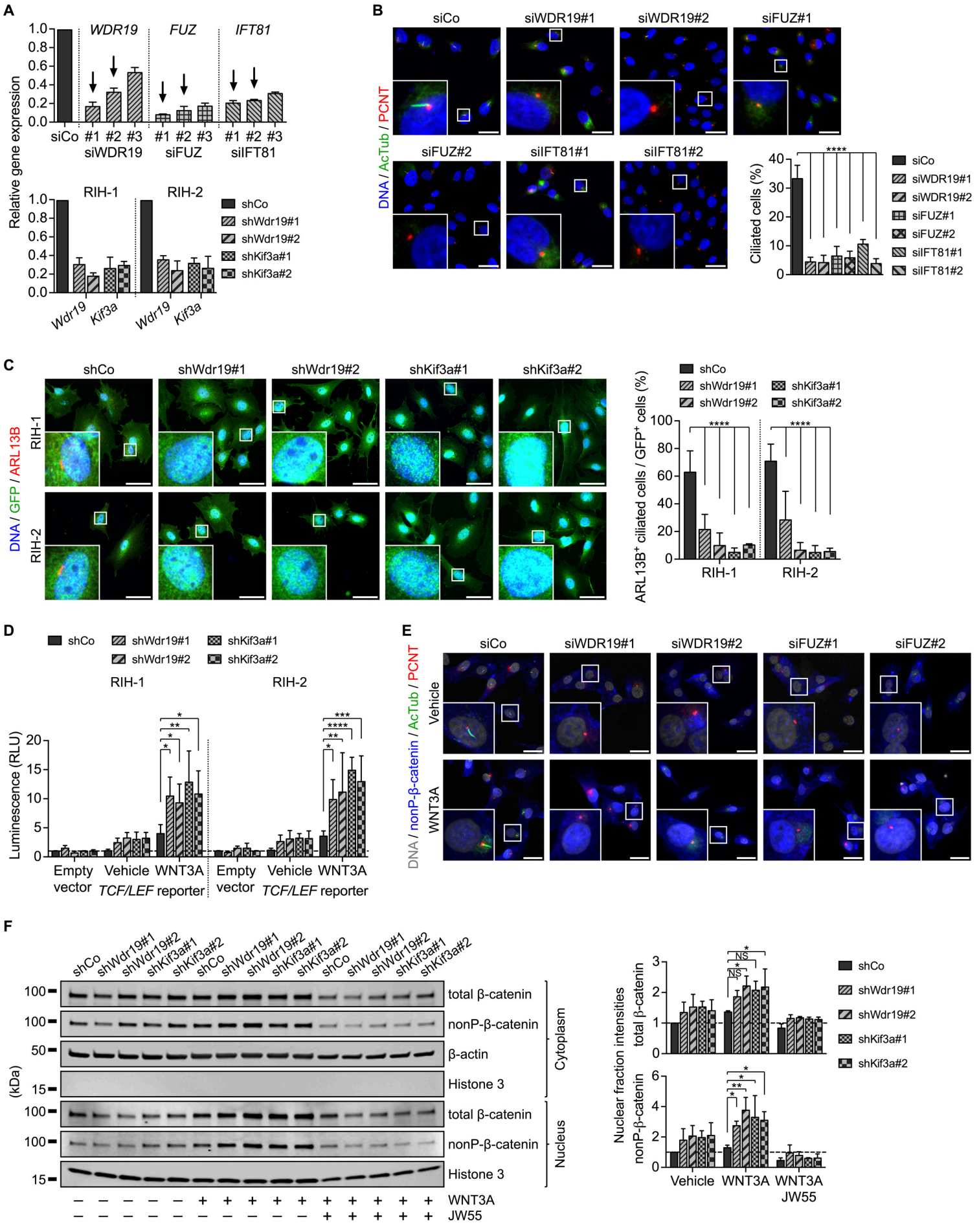
A
WDR19
FUZ
IFT81
Relative gene expression
siCo #1 #2 #3 #1 #2 #3 #1 #2 #3
siWDR19 siFUZ siIFT81
RIH-1
RIH-2
shCo
shWdr19#1
shWdr19#2
shKif3a#1
shKif3a#2
Wdr19 Kif3a Wdr19 Kif3a
B
siCo
siWDR19#1
siWDR19#2
siFUZ#1
siFUZ#2
siIFT81#1
siIFT81#2
DNA / AcTub / PCNT
Ciliated cells (%)
****
siCo
siWDR19#1
siWDR19#2
siFUZ#1
siFUZ#2
siIFT81#1
siIFT81#2
C
shCo
shWdr19#1
shWdr19#2
shKif3a#1
shKif3a#2
RIH-1
RIH-2
DNA / GFP / ARL13B
ARL13B+ ciliated cells / GFP+ cells (%)
****
****
RIH-1
RIH-2
D
shCo
shWdr19#1
shWdr19#2
shKif3a#1
shKif3a#2
RIH-1
RIH-2
Luminescence (RLU)
Empty vector
Vehicle
WNT3A
TCF/LEF reporter
E
siCo
siWDR19#1
siWDR19#2
siFUZ#1
siFUZ#2
Vehicle
WNT3A
DNA / nonP-β-catenin / AcTub / PCNT
F
shCo shWdr19#1 shWdr19#2 shKif3a#1 shKif3a#2
(kDa)
total β-catenin
nonP-β-catenin
β-actin
Histone 3
Cytoplasm
Nucleus
WNT3A
JW55
Nuclear fraction intensities
total β-catenin
nonP-β-catenin
NS
Vehicle
WNT3A
WNT3A JW55

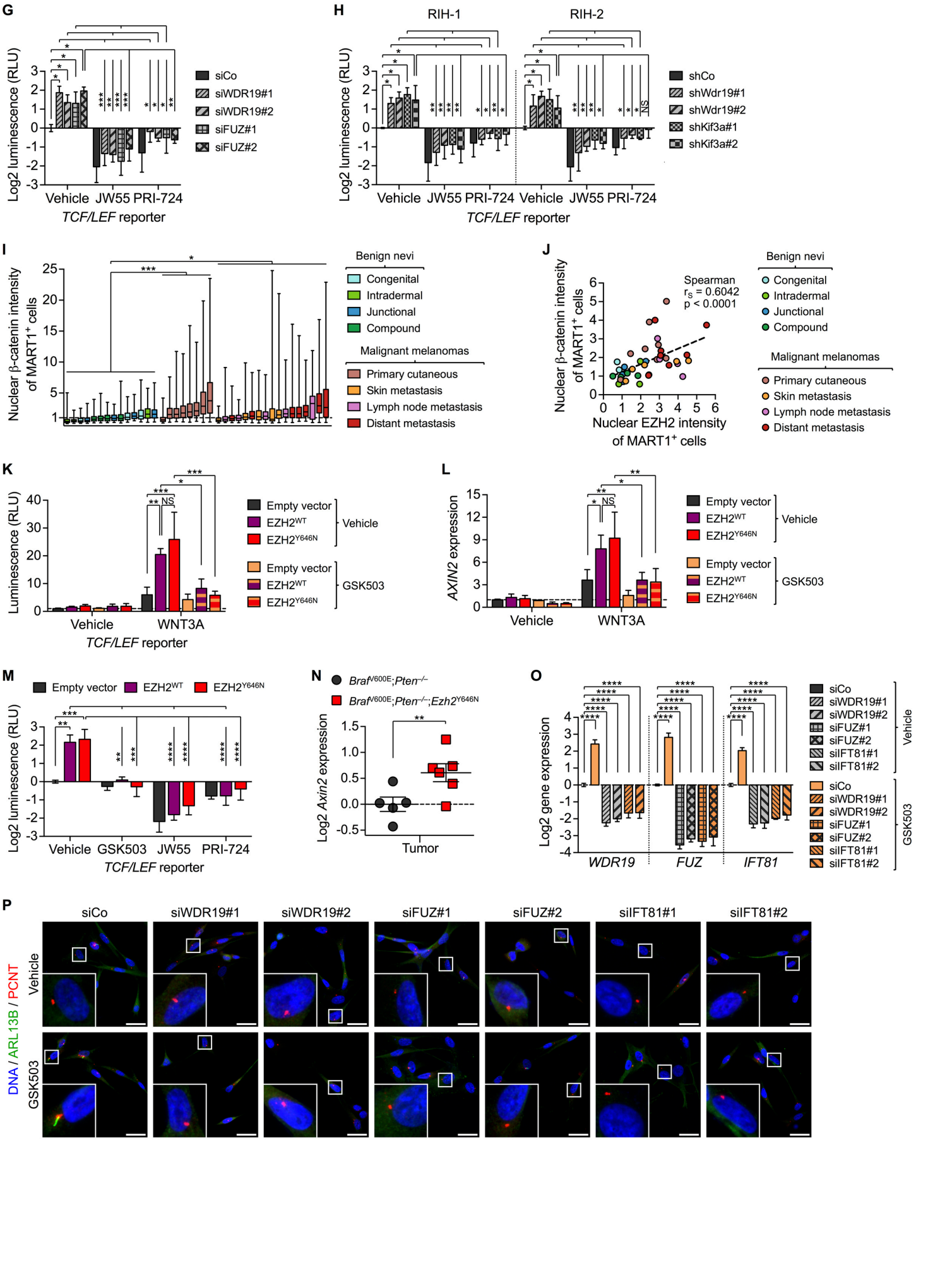
G
Log2 luminescence (RLU)
siCo
siWDR19#1
siWDR19#2
siFUZ#1
siFUZ#2
Vehicle JW55 PRI-724
TCF/LEF reporter
H
RIH-1
RIH-2
Log2 luminescence (RLU)
shCo
shWdr19#1
shWdr19#2
shKif3a#1
shKif3a#2
Vehicle JW55 PRI-724 Vehicle JW55 PRI-724
TCF/LEF reporter
I
Nuclear β-catenin intensity of MART1+ cells
Benign nevi
Congenital
Intradermal
Junctional
Compound
Malignant melanomas
Primary cutaneous
Skin metastasis
Lymph node metastasis
Distant metastasis
J
Nuclear β-catenin intensity of MART1+ cells
Spearman
rS = 0.6042
p < 0.0001
Nuclear EZH2 intensity of MART1+ cells
Benign nevi
Congenital
Intradermal
Junctional
Compound
Malignant melanomas
Primary cutaneous
Skin metastasis
Lymph node metastasis
Distant metastasis
K
Luminescence (RLU)
Empty vector
EZH2WT
EZH2Y646N
Vehicle
GSK503
Vehicle WNT3A
TCF/LEF reporter
L
AXIN2 expression
Empty vector
EZH2WT
EZH2Y646N
Vehicle
GSK503
Vehicle WNT3A
M
Empty vector
EZH2WT
EZH2Y646N
Log2 luminescence (RLU)
Vehicle GSK503 JW55 PRI-724
TCF/LEF reporter
N
BrafV600E;Pten−/−
BrafV600E;Pten−/−;Ezh2Y646N
Log2 Axin2 expression
Tumor
O
Log2 gene expression
siCo
siWDR19#1
siWDR19#2
siFUZ#1
siFUZ#2
siIFT81#1
siIFT81#2
Vehicle
GSK503
WDR19 FUZ IFT81
P
siCo
siWDR19#1
siWDR19#2
siFUZ#1
siFUZ#2
siIFT81#1
siIFT81#2
Vehicle
GSK503
DNA / ARL13B / PCNT

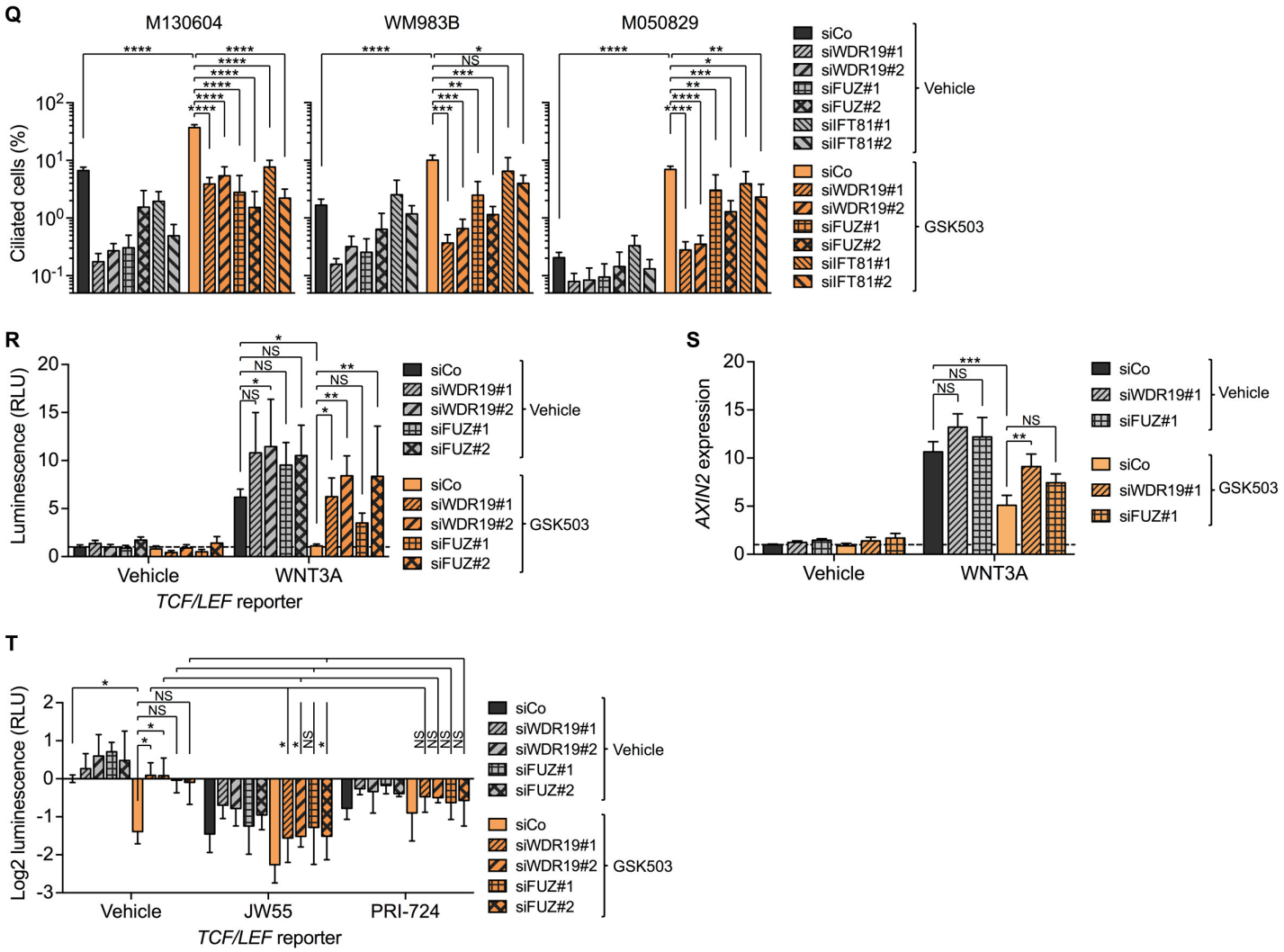

Figure S6, related to Figure 6. Loss of primary cilia induces WNT/β-catenin signaling.

(A) *WDR19*, *FUZ*, and *IFT81* mRNA expression in A375 cells after transfection with siRNAs targeting these genes (top panel), and *Wdr19* and *Kif3a* mRNA expression in RIH cells after infection with lenti-viruses targeting these genes (bottom panel). Black arrows, siRNAs chosen for further experiments. (B) Immunofluorescence staining for acetylated tubulin (AcTub) and PCNT to quantify ciliated A375 cells transfected with siCo, siWDR19, siFUZ, or siIFT81. Scale bars, 25 μm. (C) Immunofluorescence staining for GFP and ARL13B to quantify ciliated GFP^{+} RIH cells infected with lenti-GFP-shCo, shWdr19, or shKif3a. Scale bars, 50 μm. (D) Luciferase reporter assays on RIH cells infected with lenti-shCo, shWdr19, or shKif3a and transfected with empty vector or *TCF/LEF* reporter plasmid after 3 hr stimulation with vehicle or WNT3A. Relative luciferase units (RLU) calculated by normalizing firefly luciferase to Renilla luciferase luminescence. (E) Immunofluorescence staining for AcTub, PCNT, and non-phosphorylated (nonP) β-catenin on A375 transfected with siCo, siWDR19, or siFUZ and stimulated with WNT3A. Scale bars, 25 μm. (F) Western blots for total and nonP-β-catenin on cytoplasmic and nuclear fractions of RIH-1 infected with lenti-shCo, shWdr19, or shKif3a, treated with JW55, and stimulated with WNT3A. (G) Luciferase reporter assays on A375 co-transfected with siCo, siWDR19, or siFUZ and *TCF/LEF* reporter plasmid and treated with JW55 or PRI-724. All samples stimulated with WNT3A. (H) Luciferase reporter assays on RIH cells infected with lenti-shCo, shWdr19, or shKif3a, transfected with *TCF/LEF* reporter plasmid, and treated as in (G). (I) Quantification of nuclear β-catenin intensity of $MART1^{+}$ melanocytic lesions. Based on immunofluorescence stainings in Figure 6C and sample numbers as in Figure 5B. (J) Nuclear EZH2 and β-catenin intensities correlation across melanocytic lesions. Based on data from (I) and Figure S5B. (K) Luciferase reporter assays on A375 co-transfected with empty vector, $EZH2^{WT}$, or $EZH2^{Y646N}$-expression and *TCF/LEF* reporter plasmids, treated with GSK503, and stimulated with WNT3A. (L) *AXIN2* mRNA expression in A375. Conditions as in (K), except without *TCF/LEF* reporter plasmid. (M) Luciferase reporter assays on A375 transfected as in (K) and treated with GSK503, JW55, or PRI-724. All samples stimulated with WNT3A. (N) *Axin2* mRNA expression. Mouse tumor numbers as in Figure S4Q. (O)

WDR19, *FUZ*, and *IFT81* mRNA expression in M130604 after transfection with siRNAs targeting these genes and treatment with GSK503. (P and Q) Immunofluorescence staining for ARL13B and PCNT (P) to quantify ciliated M130604, WM983B, and M050829 melanoma cells transfected with siCo, siWDR19, siFUZ, or siIFT81 and treated with GSK503 (Q). Scale bars, 25 μm. (R) Luciferase reporter assays on M130604 transfected with siCo, siWDR19, or siFUZ and *TCF/LEF* reporter plasmid, treated with GSK503, and stimulated with WNT3A. (S) *AXIN2* mRNA expression in M130604. Conditions as in (R), except without *TCF/LEF* reporter plasmid. (T) Luciferase reporter assays on M130604 transfected as in (R) and treated with GSK503, JW55, or PRI-724. All samples stimulated with WNT3A. Data are represented as mean ± SEM (A–H and K–T) of 3 independent experiments (A–H, K–M, and O–T) or as median ± interquartile range (box) and ± 100% range (whiskers) (I). p values calculated with ANOVA and Fisher's LSD test (B–I, K–M, and O–T), Spearman's r_S (J), or unpaired Student's *t*-test (N).

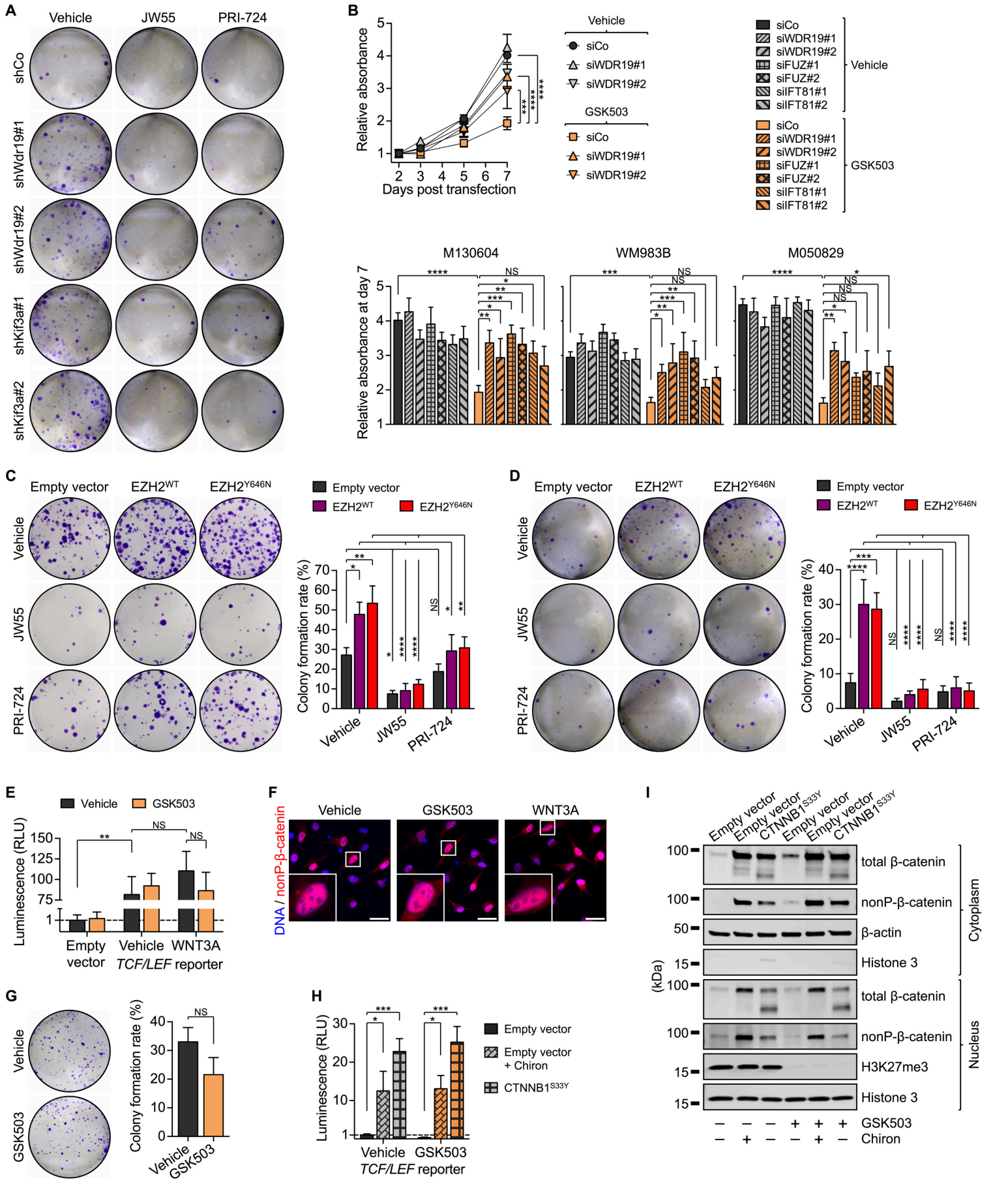

Figure S7, related to Figure 7. Primary cilium disassembly and WNT/β-catenin signaling promote melanoma growth.

(A) Colony formation assay of RIH-1 infected with lenti-shCo, shWdr19, or shKif3a and treated with JW55 or PRI-724. Quantifications are in Figure 7C. (B) Growth curves of M130604 and density after 7 days of M130604, WM983B, and M050829

transfected with siCo, siWDR19, siFUZ, or siIFT81 and treated with GSK503. (C and D) Clonogenicity of A375 (C) and RIH-1 (D) transfected with empty vector, $EZH2^{WT}$, or $EZH2^{Y646N}$-expression plasmids and treated with JW55 or PRI-724. (E) Luciferase reporter assays on 501Mel (endogenous $CTNNB1^{S37F}$) cells transfected with *TCF/LEF* reporter plasmid, treated with GSK503, and stimulated with WNT3A. (F) Immunofluorescence staining for nonP-β-catenin on 501Mel treated with GSK503 or stimulated with WNT3A. Scale bars, 25 μm. (G) Clonogenicity of 501Mel treated with GSK503. (H) Luciferase reporter assays on M130604 co-transfected with empty vector or $CTNNB1^{S33Y}$-expression and *TCF/LEF* reporter plasmids and treated with Chiron or GSK503. (I) Western blots for total and nonP-β-catenin on cytoplasmic and nuclear fractions of M130604 transfected with empty vector or $CTNNB1^{S33Y}$-expression plasmid and treated with Chiron or GSK503. Data are represented as mean ± SEM of 3 (B, E, and H) or 4 (C, D, and G) independent experiments. p values calculated with ANOVA and Fisher's LSD test (B–D, E, and H) or unpaired Student's *t*-test (G).

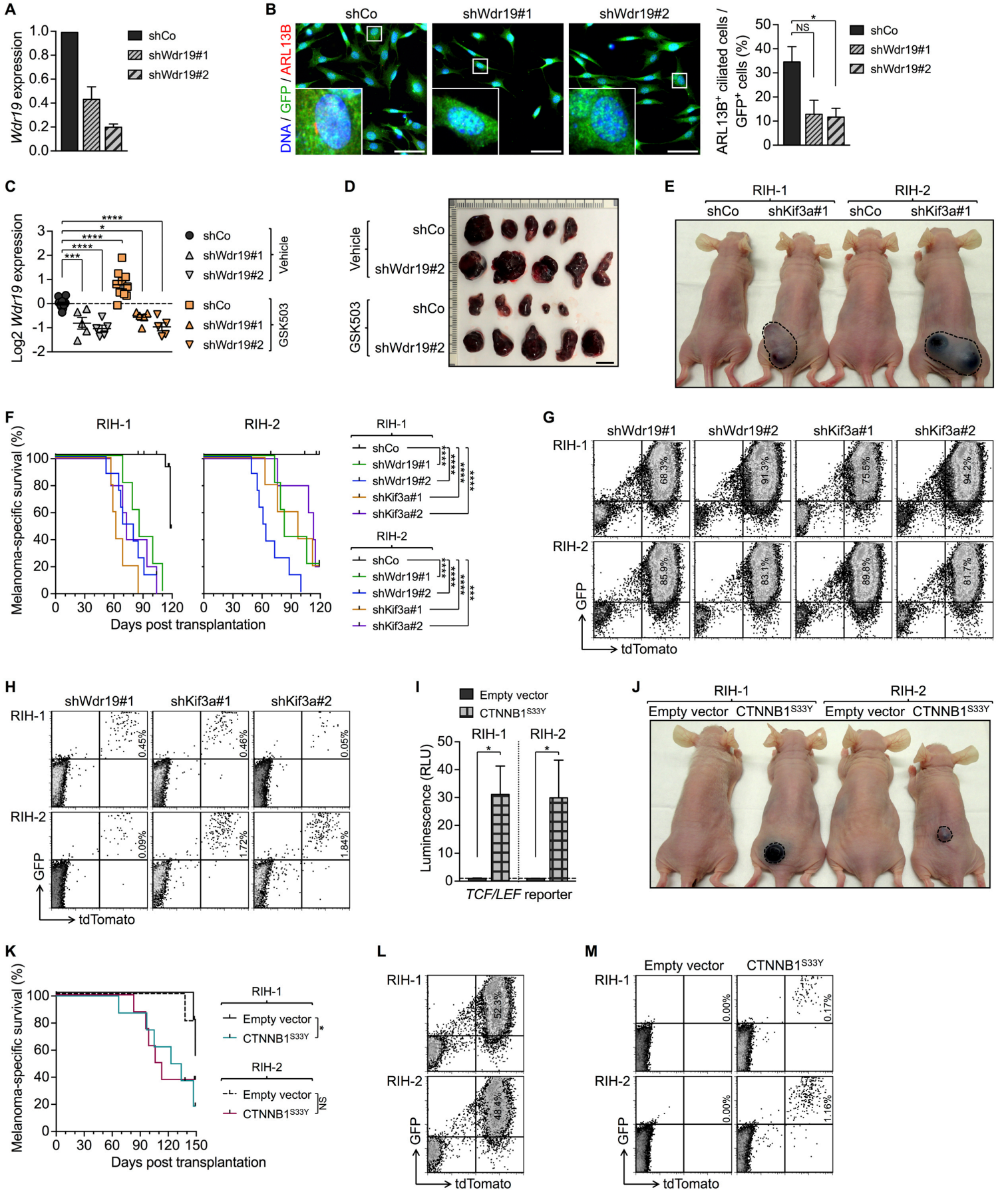
A
Wdr19 expression
shCo
shWdr19#1
shWdr19#2
B
shCo
shWdr19#1
shWdr19#2
DNA / GFP / ARL13B
ARL13B+ ciliated cells / GFP+ cells (%)
NS
*
C
Log2 Wdr19 expression
Vehicle
GSK503
D
Vehicle
GSK503
E
RIH-1
RIH-2
shKif3a#1
F
RIH-1
RIH-2
Melanoma-specific survival (%)
Days post transplantation
shKif3a#2
G
shWdr19#1
shWdr19#2
shKif3a#1
shKif3a#2
68.3%
91.3%
75.5%
94.2%
85.9%
83.1%
89.8%
81.7%
GFP
tdTomato
H
0.45%
0.46%
0.05%
0.09%
1.72%
1.84%
I
Empty vector
CTNNB1S33Y
Luminescence (RLU)
TCF/LEF reporter
J
K
Empty vector
CTNNB1S33Y
L
52.3%
48.4%
M
0.00%
0.17%
0.00%
1.16%

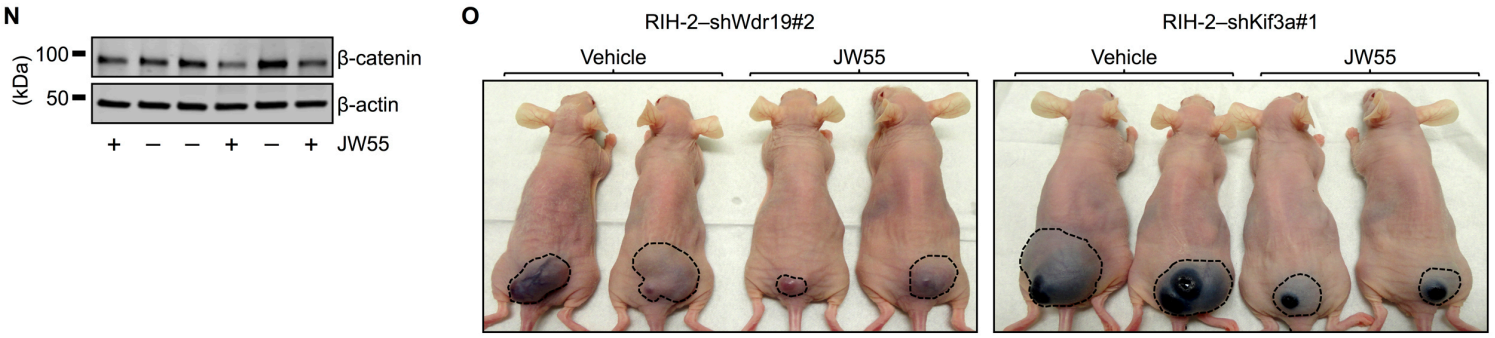

Figure S8, related to Figure 8. Primary cilium deconstruction is sufficient to initiate metastatic melanoma.

(A) *Wdr19* mRNA expression in RIM-3 cells infected with lenti-GFP-shCo or shWdr19. (B) Immunofluorescence staining for GFP and ARL13B to quantify ciliated GFP^+ RIM-3 infected with lenti-shCo or shWdr19. Scale bars, 50 μm. (C) *Wdr19* mRNA expression in tumors derived from RIM-3 infected with lenti-shCo or shWdr19, transplanted into Nude mice, and treated with vehicle or GSK503. Mouse numbers as in Figure 8B. (D) Picture of tumors from mouse cohorts in Figure 8B. (E and F) Picture (E) and Kaplan-Meier curves (F) comparing melanoma-specific survival of mouse cohorts in Figures 8G and 8H. (G and H) FACS analyses to quantify GFP^+ td-$tomato^+$ cells in tumors (G) and lungs (H) from mice in Figures 8G and 8H. Quantifications are in Figure 8I. (I) Luciferase reporter assays on RIH cells infected with lenti-empty vector or $CTNNB1^{S33Y}$ and transfected with *TCF/LEF* reporter plasmid. (J and K) Picture (J) and Kaplan-Meier curves (K) comparing melanoma-specific survival of mouse cohorts in Figure 8J. (L and M) FACS analyses to quantify GFP^+ td-$tomato^+$ cells in $CTNNB1^{S33Y}$ tumors (L) and lungs (M) from mice in Figure 8J. Quantifications are in Figure 8K. (N) Western blot to quantify β-catenin intensities of second-generation tumors derived from a RIH-1–$EZH2^{Y646N}$ tumor (Figure 1E) and treated with vehicle or JW55. Quantification is in Figure 8L. (O) Pictures of mice in Figures 8N and 8O. Data are represented as mean ± SEM (A–C and I) of 3 independent experiments (A, B, and I). p values calculated with ANOVA and Fisher's LSD test (B and C), log-rank (Mantel-Cox) test (F and K), or unpaired Student's *t*-test (I).

Table S2, related to STAR★METHODS. Primers.

GENE	FORWARD SEQUENCE	REVERSE SEQUENCE
Cloning primers		
BamHI-*CTNNB1*	ATATGGATCCATGGCTACTCAAGCTGAC	
CTNNB1-EcoRI		GCCGTCTAGATTACAGGTCAGTATCAAACCA
Mouse genotyping primers		
Cre	CTATCCAGCAACATTTGGGCCAGC	CCAGGTTACGGATATAGTTCATGAC
Ezh2^{WT}	AAGGCTGTGTACAGGAAACAATC	AGTACTCCAGAGGTACTGAAGTTTG
Ezh2^{lox}	AAGGCTGTGTACAGGAAACAATC	TCACCTTAATATGCGAAGTGGAC
Ezh2^{Y646N}	TTTCTGTGCCATTGCTAGGT	ACTTTCCCTCTTCTGTCAGC
Cdkn2a^{WT}	ATGATGATGGGCAACGTTC	CAAATATCGCACGATGTC
Cdkn2a^{KO}	CTATCAGGACATAGCGTTGG	AGTGAGAGTTTGGGGACAGAG
LacZ	GGTCGGCTTACGGCGGTGATTT	AGCGGCGTCAGCAGTTGTTTTT
Nras^{Q61K}	GATCCCACCATAGAGGATT	CTGGCGTATTTCTCTTACC
Mouse qPCR primers for cDNA		
Axin2	AGAGGGACAGGAACCACTCG	GGACACTTGCCAGTTTCTTTGG
Ccdc113	GCTGAGAAACGAGCTACTTGG	AGATATGGGCTTTGGCCCTG
Celsr2	CCCTGCCTTGACCACTAAGTC	GCCGAATCTCCGTAAGGCTG
Ezh2	GTGACCACAGGATAGGCATCT	CAAGGGATTTCCATTTCTCG
Fuz	GAAACTTCTACACGCTGGTGG	TGGCCCTAGCACGAGATAAC
Ift81	GTTGACGAGATGAAAGGCCG	TTTCTGACGCAACTGCCGTA
Kif3a	AGCTCCGTCTTCAGATGCTC	GCCACACATTTTAGCTGCCA
Lztfl1	ACAGCTCGATCAAGAAAACCAAC	TGCAACTGTATTTTCCAAGTCATCC
Tulp3	ACCATGGTGTCAACCCAGTC	TCCTGGGACCTTTGAAACCG
Usf1	CAGGGCTCAGAGGCACTACT	GCTCCCTCCCTGCAATACTT
Wdr19	ACCACCCCATGTCCATTCTG	CGTCTTTCAACATGTGTCGGC
Wdr63	TGGACCTTAAGTCACCCTTCC	TGCTGGACGTATTCCAGGTG
Human qPCR primers for cDNA		
AXIN2	CAGGTCGCAGGATGTCTGG	GGGCAGACTCCAAGGGGTA
CCDC113	TGGACAAGGAGATCTTGCTGAG	CTCTTATTCACTGCCTCGGCT
EZH2	GCTTCCTACATCGTAAGTGCAA	AGCAAACTCCTTTGCTCCCT
FUZ	GTGGAGCCCTTGGGGGATA	CTCATCTTCTGTCTTCTCTGGTGG
IFT81	ATCTTGCACAACAGAAACAGGAAC	TGCTTTTCAGCTGGTTTTGTACTC
LZTFL1	AGCCAAGCACGATCTACTCAG	TTCGATAAGCTGCTGTTTGCTG
NDEL1	TGGCAATGGCACAAAGTTCTC	CCGTTTACTGCCCCATGAAC
USF1	TACTACCCAGGGCTCAGAGG	TCCCTGCAGTACTTCTTGTGG
WDR19	TGATGAGGCCTGAATACCGC	AATGGACATGGAGTCGTGGC
WDR63	TTAAGTCGCCCTTCCACCAA	CGCTGTTCTACGTATTCCAGATG
Mouse qPCR primers for genomic DNA		
Ccdc113	GGGGCAGAGACTTATGCGAG	CAAATCTTTGCATGGACCCTGTT
Celsr2	CGCAGGTAGAGAACGCTCAG	CTCCCACCACTCTCGAAGC
Ezh2 Intron 18	CAAGTGACAGCAAACTTCAGTACC	ACTGCAAAGAGAAACATTGGCAG
Fuz	GCAACACCTTAGCACCATCAC	TGCCAAGCGTTCAAGTTGTTC
Ift81	GTCGCCCCAAGTTTGGTAAATAA	CCGTCTACCGTTCTCACCTTG
Interg1	GCTCCGGGTCCTATTCTTGT	TCTTGGTTTCCAGGAGATGC
Lztfl1	AAGTTATTCTCTTCTGCCAGCGT	TCCGGCTATCAAGCTCATGC
Tulp3	ATTTGCTGAAGGTCCCCAGG	CATCTGACCACCGACTCTGG
Wdr19	GCTCACATAGCTCAAGACCCTT	AGTTGAATGCTACGAGGGCT
Wdr63	CTGGGCTTCTCTGGGATTACG	TATCCGCTCCCCAACATTGTC
Human qPCR primers for genomic DNA		
ARL13B	ACCGTGGATTGGCAACACAT	GTAACTAGGCAACCGGAGCG
BBS2	CTAGACCGAACGTGAGTCTAAGG	TATTCCTTGAGTGTCGGCTCTG
BBS4	TGTTAGGGGCTTCTCGGGAT	TCTGCTCCACAGAAGGCTTAC
CCDC113	GGTTGTGGCGAAGGTTTTCA	GCAGCTGCTGTTTCTCAGC
CELSR2	TCAGGGGGCAGTGGGAG	CTGCGTCTGGATGGCTCG
DYNC2H1	CGACGCCGCCGTAGTG	ACCCGTAGCCCGACCG
DYNC2LI1	CTTGGCATATAGTTGACACCCAG	CTCCTAGAACGAGATGATAAGGGG
FUZ	ACCTACAGGGAATGTGGTTGC	AAAACAGCTGTGCCCGGAT
IFT81	TTTTGTAAACTGCGAAGTGCAGG	TTTGGGACTGTTACTCCGACC
IFT88	CATCCTTTGGGCATCTGCTTTAC	AGGGGAAGGATATGGAACCAAG
IFT140	AAAACGGCGCTCCCATTG	GCGTCACAACACTACTGGC
INTU	GCTGCTCTAAGGAATTGCGTTC	AGGAGGGCTTCTCAGTTGGA
INVS	AAATGTAGTCCTGCACTAGCCTC	GAGCCCAATGGGAAAGGAAGTT

LZTFL1	GCGCCCTATGAGACCATTGA	GTCCAGAACTTCCTGTGGCA
STIL	CACCAATACGTAACGGCGAC	TGACTGGTCAGAAACCTCGC
TULP3	GAGGACCAAGCCTTAGCTCG	GATGCGGGAGGGTTGCTAAG
VANGL2	TTCTCCGACAGGAGGGGTC	GGAATGCCTCGATTCTTGGACT
WDR19	TCTTATGCCTCCTCCCTTCTACC	TCCTATACAGTCCACGCAAAGAG
WDR63	TTCCTAGGGTCCACACCCC	AGGTCTAACAGGCTCGGTCC